Interplay between charge, magnetic and superconducting properties in copper-based and iron-based superconductors

A DISSERTATION
SUBMITTED TO THE FACULTY OF THE GRADUATE SCHOOL
OF THE UNIVERSITY OF MINNESOTA
BY

Xiaoyu Wang

IN PARTIAL FULFILLMENT OF THE REQUIREMENTS
FOR THE DEGREE OF
Doctor of Philosophy

Prof. Rafael M. Fernandes

August, 2017

Acknowledgements

In 2010, I graduated with a Bachelor's degree in Electrical Engineering, decided to follow my interest in theoretical physics, and came to the physics graduate program in University of Minnesota. Upon completion of this thesis, my years in the graduate school will come to a happy ending, and I am ready to start a new chapter as a physics postdoctoral researcher in University of Chicago. Looking back, the seven years were filled with obstacles and bitterness. However, these make the accomplishments all the more valuable. I am thankful to all the people who have helped me achieving my goals in research, as well as giving me the courage and perseverance to carry on amid difficulties.

First and foremost, I am deeply indebted to my adviser Prof. Rafael Fernandes, for all the efforts he put into preparing me for a career in academia. He is very approachable as an adviser, offering all the help I ever wanted when I got stuck in the middle of a project. He is very active in referring me to various workshop opportunities which are of enormous help to building my career. More importantly, his great passion for physics, critical thinking, and rigorous attitude towards research all greatly benefitted me as a person.

I am thankful to Prof. Alex Kamenev, who I worked with during my first three years in graduate school, and still maintain excellent relationship. Although it is a bit unfortunate that our collaborations hadn't resulted in published works, I learned a good deal from him on the methods of studying nonequilibrium phenomena.

I am also greatly thankful to Dr. Jian Kang, Dr. Yuxuan Wang, Dr. Yoni Schattner, Dr. Michael Schütt, Dr. Peter Orth and Dr. Morten Christensen for valuable discussions and collaborations in research.

I want to thank my friends for being part of my life during the seven years in Minnesota, including Qianhui Shi, Tobias Gulden, Yangmu Li, Ruiqi Xing, Tianbai

Cui, Jiaming Zheng, Yang Tang, Qi Shao, Han Fu, Michael Albright, Yanqing Sun and many others. I also want to acknowledge the Twin Cities Go Club and the U of M Go Club, which kept me (happily) busy on the weekends.

Last but not least, I want to say thank you to my parents, who supported me through 16 years of school in China, and endured my seven years away from home in the United States with only increasing love and patience.

I also acknowledge financial supports from teaching and research assistantships offered by the School of Physics and Astronomy in University of Minnesota, the Hoff Lu fellowship granted by Mike and Lester Lu, and the Doctoral Dissertation Fellowship offered by the graduate school in University of Minnesota. In addition, I also acknowledge funding granted by the Department of Energy.

Dedication

This thesis is dedicated to my beloved parents, Jianjun Wang and Huimin Li.

Abstract

Superconductivity (SC) is an electronic phase of matter in which certain condensed matter systems conduct electricity without resistance and completely expel magnetic fields from their interiors. Since the initial discovery in mercury over a century ago, great advances have been made to deepen our understanding of the SC phenomenon and its microscopic mechanism. In two families of layered materials, namely, the cuprates and the iron pnictides/chalcogenides, the superconducting transition temperatures can be higher than the boiling point of liquid Nitrogen. Furthermore, the microscopic origin is not due to electron-phonon coupling, as is the case for low-temperature superconductors. In addition to SC, the phase diagram of these systems exhibit several other electronic phases of matter, such as antiferromagnetism, nematicity and charge density wave. The normal state also exhibits properties different than those of normal metals.

In this thesis, I use analytical and numerical Quantum Monte Carlo (QMC) methods to shed light on the interplay between these ordered states. In particular, I will study the novel magnetic phases in iron pnictides, and attribute their origin to the itineracy of electrons. I will discuss the magnetic origin of electronic nematicity in these materials, and describe the spectroscopic manifestations. I will elaborate on the origin and properties of SC and charge density wave orders near a metallic antiferromagnetic quantum critical point, as well as its relevance to both cuprate and iron pnictide/chalcogenide superconductors.

Contents

List of Figures

Chapter 1

Introduction

1.1 Superconductivity

In condensed matter systems, one of the most fascinating phenomena is the emergence of various electronic phases of matter due to the interactions between individual electrons. Such phases of matter exhibit collective properties, with collective excitations different than that of a single electron. Among the many electronic phases is superconductivity, where the system conducts electricity without resistance, and expels magnetic field completely from its interior. Such electric and magnetic properties make superconductors useful for many applications, such as dissipationless power transmission, magnetic sensing, and quantum computation.

Superconductivity was first discovered in 1911 in mercury below a critical temperature of 4.2K. The past century saw great advances in our understanding of the phenomenon, as well as the discovery and synthesis of new superconducting materials. Fig. 1.1 is a summary of the families of superconducting materials as well as their transition temperatures. There are metallic elements such as mercury and lead, metallic alloys such as niobium nitride and magnetism diboride, heavy fermion compounds such as UPt_3, fullerene compounds such as Cs_3C_{60}, and organic compounds such as carbon nanotubes. In addition, there are the copper-oxide (cuprate) and the iron-pnictide/chalcogenide superconductors discovered in 1986 and 2008 respectively. They are also called high T_c superconductors and unconventional superconductors, because the transition temperature surpasses the boiling point of liquid nitrogen (77K), and the

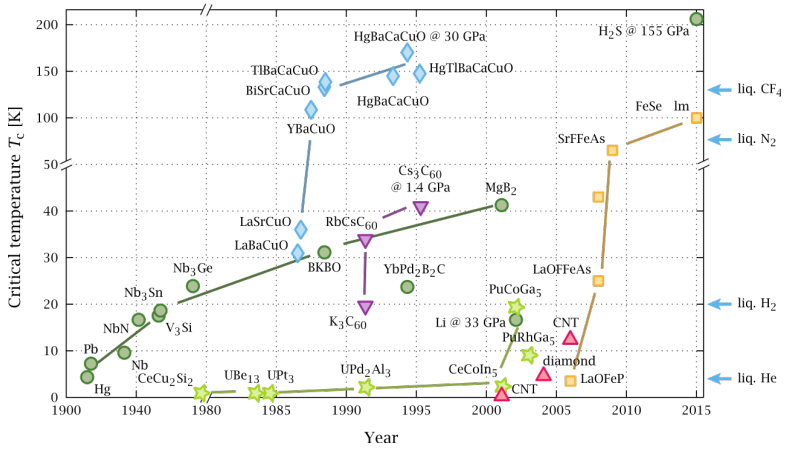

Figure 1.1: Superconductors discovered over the years. The families of superconductors are metallic elements and alloys (green circles), heavy fermion compounds (green stars), organics (red triangles), fullerene (purple triangles), cuprates (blue diamonds) and iron pnictides/chalcogenides (orange squares). From Ref. [1].

microscopic origin is different than the superconducting metals and alloys.

Microscopically, superconductivity is a result of the electronic system forming phase coherent Cooper pairs. A Cooper pair is a bound state of two electrons, and has a lower energy than that of two free electrons, making it robust against small pair-breaking perturbations such as temperature and magnetic field. The existence of phase coherent Cooper pairs is verified by the measurement of the magnetic flux quanta $\Phi_0 = h/2e$ (Ref. [2, 3, 4]).

A Cooper pair is described by a quantum mechanical wavefunction $\Psi_{\alpha\beta}(\mathbf{R}, \mathbf{r})$, where α and β label the electronic spin state, and $\mathbf{R}$, $\mathbf{r}$ label the center of mass position and the relative position of the two electrons respectively. The Cooper pair can be in either a spin-1 state (called a triplet) or a spin-0 state (called a singlet). It can also be in a definite angular momentum state, such as the s-wave, p-wave and d-wave, corresponding to angular momentum number $l = 0, 1, 2$ respectively.

The mechanism for Cooper pairing was addressed in a seminal paper by Bardeen, Cooper and Schrieffer [5], now known as the BCS theory of superconductivity. The BCS theory shows that in the presence of a Fermi surface,[1] any two electrons can

[1] In metals, due to Pauli's principle, electrons fill up the lowest-energy states in the conduction band. The Fermi surface describes the states in the momentum space that electrons fill up to.

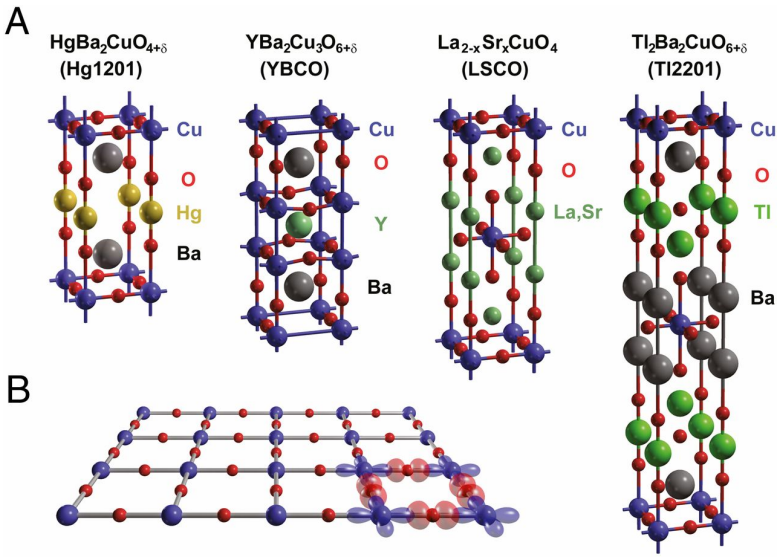

Figure 1.2: A. Crystal structures of $HgBa_2CuO_{4+\delta}$, $YBa_2Cu_3O_{6+\delta}$, $La_{2-x}Sr_xCuO_4$, and $Tl_2Ba_2CuO_{6+\delta}$. B. CuO_2 layer. Figure from Ref. [8].

bind into a Cooper pair by arbitrarily small attraction. Near the Fermi surface, the Coulomb repulsion between electrons is screened. Instead, electrons attract each other by exchanging lattice vibrations, namely phonons. The electron-phonon mechanism is verified by the isotope effect on T_c (Ref. [6, 7]). The Cooper pair predicted by the BCS theory is a spin-singlet s-wave bound state.

While the superconducting metals and alloys shown by green circles in Fig. 1.1 are explained by the BCS mechanism, there are important exceptions. Most notably, the cuprate and iron pnictide/chalcogenide family of high T_c superconductors cannot be explained by the electron-phonon mechanism. Rather, experiments over the past thirty years suggest that superconductivity is of purely electronic origin. How superconductivity can arise from Coulomb repulsion remains one of the fundamental questions to be solved.

In this thesis, I will describe my research on the theoretical understanding of several aspects of the electronic phase diagram of high T_c cuprates and iron pnictides/chalcogenides.

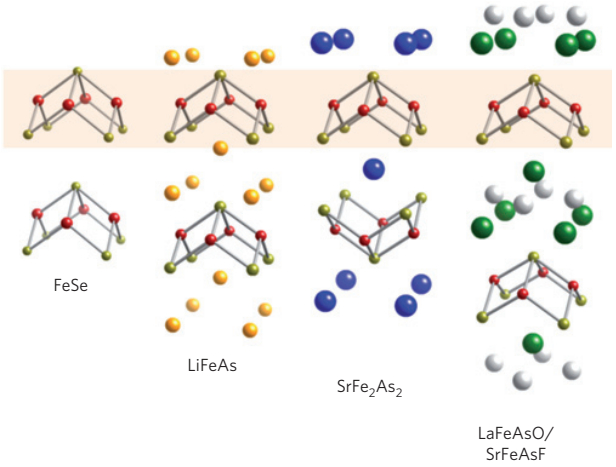

Figure 1.3: Crystal structures of FeSe, LiFeAs, $BaFe_2As_2$, and LaOFeAs. Fe atoms are colored red, and pnictogen/chalcogen atoms green. Taken from Ref. [9].

1.2 Structural properties

All cuprate high T_c superconductors have a layered structure as depicted in Fig. 1.2. Some of the most studied materials include $HgBa_2CuO_{4+\delta}$ and $YBa_2Cu_3O_{6+\delta}$. All cuprates have a stoichiometric CuO_2 layer, where the copper atoms form a two dimensional square lattice, with oxygen atoms residing on the centers of the bonds. The CuO_2 layer is believed to be responsible for the various low energy electronic properties. Additionally, there are spacer layers made of oxides (e.g., HgO) and cations (e.g., Y^{3+}). Different families of cuprates have different numbers and contents of spacer layers. These differences are responsible for the variations in the electronic phase diagram.

Like the cuprates, the iron pnictides/chalcogenides also have layered crystal structures, with a common layer made of iron pnictogen (e.g., FeAs) or iron chalcogen (e.g., FeSe). The Fe atoms form a square lattice. However, the pnictogens/chalcogens protrude out of the two dimensional plane, forming a "puckering" pattern. The most studied families of compounds are the 11 family (e.g. FeSe/Te), the 111 family (NaFeAs), the 1111 family (LaOFeAs), and the 122 family ($BaFe_2As_2$). Fig. 1.3 shows their crystal structures.

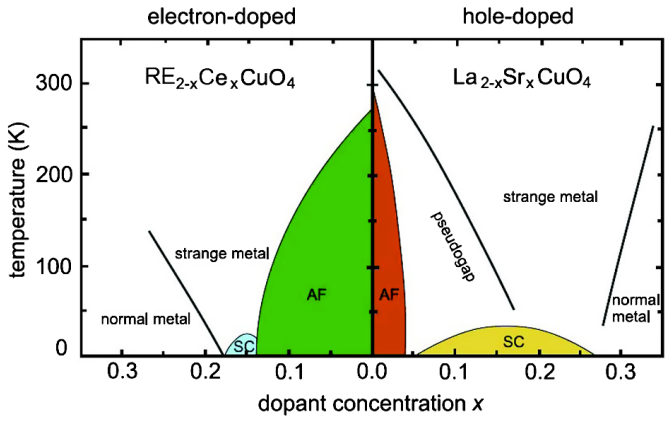

Figure 1.4: Electronic phase diagram of both hole (right panel) and electron (left panel) doped cuprate superconductors. Taken from Ref. [10]. The parent compound is an antiferromagnetic Mott insulator. Superconductivity is achieved by electron/hole doping. In the hole-doped materials, there is a "pseudogap" phenomenon in the intermediate temperature and doping ranges, characterized by suppressed electronic spectral weight at the Fermi surface. Near optimal doping, the disordered phase behaves like "strange" metal characterized by linear resistivity $\rho \propto T$. The overdoped side is characterized by standard Fermi liquid behavior. In recent years, various symmetry breakings have been observed inside the pseudogap region, including time reversal symmetry breaking, rotational symmetry breaking, and translational symmetry breaking.

1.3 Electronic phase diagram

Fig. 1.4 shows a typical electronic phase diagram of cuprates as a function of temperature and doping. The stoichiometric compounds are Mott insulators,[2] which develop antiferromagnetic order below a critical temperature. The antiferromagnetic order is the Néel order, where the electronic spins on neighboring Cu atoms are antiparallel to each other.

Superconductivity is achieved by doping charge carriers (electrons or holes) into the CuO_2 plane. This is done either by substituting the spacer layer cations by elements in other columns of the periodic table, such as $La_{2-x}Sr_xCuO_4$, or by oxygen vacancies, such as $YBa_2Cu_3O_{6+\delta}$. The antiferromagnetic order is suppressed as doping increases.

In addition to antiferromagnetism and superconductivity, the materials also exhibit

[2] Mott insulators are metallic systems driven to an insulating phase due to strong electronic interactions.

a "pseudogap" region at intermediate temperature and doping ranges, characterized by a loss of electronic spectral weight at the Fermi level.[3] The pseudogap shows up in various measures, including angle resolved photo-emission spectroscopy (ARPES), scanning tunneling spectroscopy (STS), unform spin susceptibility, nuclear magnetic resonance (NMR) and so on. It is unclear if the pseudogap temperature (T^*) marks a true phase transition or a crossover. Nonetheless, there have been reports on various symmetry breaking phases occurring in the pseudogap region. Most notably, in recent years, static charge density wave orders have been discovered in various cuprate materials, although short-ranged in many cases[11, 12].

Another very interesting feature observed in both electron and hole-doped cuprates is that near optimal doping (i.e., where superconducting T_c is highest), the normal state exhibits strange metallic behaviors. Normal metals are described by the Landau Fermi liquid theory, with electrical resistivity $\rho \propto T^2$ due to quasiparticle scattering from Coulomb interaction. However, the strange metallic phase is characterized by a linear resistivity: $\rho \propto T$. There are many proposals for the linear resistivity behavior, including proximity to a quantum critical point[13, 14, 15], percolative transport[16] etc. I will discuss quantum critical behaviors later in detail.

Fig. 1.5 shows the phase diagram of the iron pnictide material $Ba(Fe_{1-x}Co_x)_2As_2$ and the iron chalcogenide material $FeSe_{1-x}S_x$. Both parent compounds ($x = 0$) are metallic rather than insulating. In $Ba(Fe_{1-x}Co_x)_2As_2$, the parent compound develops a stripe-type magnetic order at low temperatures, where the spins in the Fe plane are antiferromagnetically aligned along one Fe-Fe bond direction, and ferromagnetically aligned along the other. The stripe magnetic order is preempted by a structural phase transition, where the square lattice symmetry is broken down to orthorhombic. Such a structural phase transition is also called a nematic phase transition. Superconductivity is induced by doping, when both structural and magnetic phase transitions are suppressed. In some iron pnictide materials, the normal state above optimal doping also exhibits strange metal behavior[19].

In $FeSe_{1-x}S_x$, Se is substituted by S, of the same group in the periodic table. Therefore, instead of doping charge carriers into the system, it is believed that the main effect is to change the "chemical pressure". The parent compound has a structural phase

[3] Whether pseudogap phenomenon occurs in electron-doped materials is controversial.

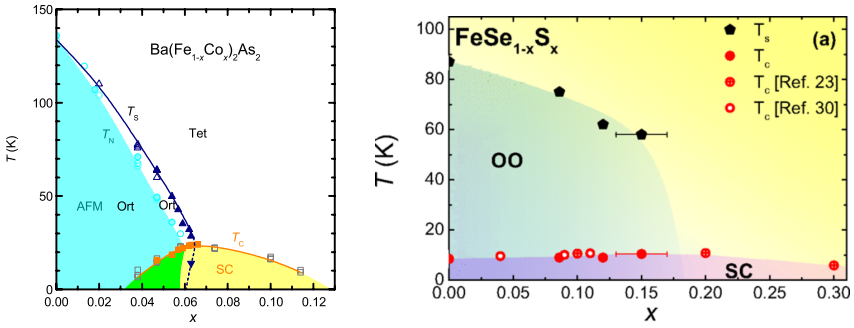

Figure 1.5: Electronic phase diagram of $Ba(Fe_{1-x}Co_x)_2As_2$ (left panel) and $FeSe_{1-x}S_x$ (right panel), taken from Ref. [17] and Ref. [18] respectively. In $Ba(Fe_{1-x}Co_x)_2As_2$, the parent compound is metallic, and develops a stripe-type antiferromagnetic magnetic order (AFM) at low temperatures. The stripe magnetic order is preempted by a structural phase transition, where the square lattice symmetry is broken down to orthorhombic (Ort). Superconductivity (SC) is induced by doping, upon suppression of both structural and magnetic phase transitions. In $FeSe_{1-x}S_x$, superconductivity exists even in the parent compound, and persists when Se is substituted by S of the same group in the periodic table. A structural phase transition (OO) occurs at a higher temperature. Unlike $Ba(Fe_{1-x}Co_x)_2As_2$, there is no long range magnetic order.

transition (labeled by OO) occurring at about 90K. Unlike $Ba(Fe_{1-x}Co_x)_2As_2$, there is no long range magnetic order.[4] In addition, the parent compound also exhibits a finite superconducting transition temperature. Upon doping, the structural phase transition is suppressed, and goes away near 15% of S substitution.

1.4 Electronic properties and theoretical modeling

The low energy electronic properties of both cuprates and iron pnictides/chalcogenides are governed by the $3d$ electronic orbitals. There are five d electronic orbitals: d_{z^2} ($l_z = 0$), $d_{xz/yz}$ ($l_z = \pm 1$), and d_{xy/x^2-y^2} ($l_z = \pm 2$). The copper ion is in the Cu^{2+} valence state, with $3d^9$ electronic configuration. The iron ion is also in the 2+ valence state, however with $3d^6$ electronic configuration.

In a free space, the five $3d$ orbitals have the same energy. The energy levels are split

[4] Despite no long range magnetic order, there is experimental evidence for enhanced magnetic fluctuations upon lowering temperature[20].

in a crystalline environment. In particular, in the cuprate materials, Cu^{2+} sits at the center of a square of oxygen atoms.[5] Crystal field splits the orbital degeneracy, with $d_{x^2-y^2}$ orbital having the highest energy. As a result, at low temperatures, four of the five d orbitals are filled, while $d_{x^2-y^2}$ orbital has only one electron, and is half filled. On the other hand, in iron pnictide/chalcogenide materials, due to the "puckering" of the pnictogen/chalcogen atoms, the crystal environment for an iron atom is between a square and a tetrahedron. While a square environment makes the iron d_{z^2/x^2-y^2} orbitals (also called the e_g orbitals) more energetic, a tetrahedron environment raises the energy of the $d_{xz/yz/xy}$ (t_{2g}) orbitals. The net result is that the crystal field splitting is much smaller compared to that in the cuprates. Therefore, a low-energy description should incorporate all five electronic orbitals[21].

Theoretically, one of the most studied microscopic models to describe these systems is the Hubbard model. Hubbard models consist of two terms: a kinetic energy term describing the electron hopping between sites, and a potential energy term describing the screened Coulomb interactions, assumed to be onsite. The hopping amplitudes are usually determined by tight-binding fits to density functional theory calculations.

A minimal model for the cuprates is the one-band Hubbard model, described as:

$$H = \sum_{ij,\sigma} (t_{ij} - \mu\delta_{ij}) c^\dagger_{i\sigma} c_{j\sigma} + U \sum_i n_{i\uparrow} n_{i\downarrow} \tag{1.1}$$

where $c^\dagger_{i\sigma}$ creates an electron on site i with spin σ, t is the hopping amplitude between sites i and j, and U is the onsite Coulomb interaction. For the iron pnictides/chalcogenides, one needs to study a multi-orbital Hubbard model [21], the details of which will be presented later in Ch. 2.

The Hubbard models are microscopic models, and are usually very complicated to solve beyond mean field approximation.[6] Another theoretical approach to understanding the electronic phase diagram is to construct low-energy effective field-theoretical models. These models can usually be solved using well established methods, and can offer great insights into the microscopic origin of various electronic phases.

[5] Some cuprate compounds have apical oxygens as well, and the crystal field is of either elongated octahedral or square pyramidal type. $d_{x^2-y^2}$ orbital still has the highest energy.

[6] For a review of various analytical and numerical methods in solving Hubbard models, as well as the various electronic phases emergent when electron density and Coulomb interaction strength are tuned, see Ref. [10].

1.5 Quantum criticality

In the cuprate phase diagram shown in Fig. 1.4, the transition temperature of the antiferromagnetic order extrapolates to zero when doping is increased, suggesting a "putative" antiferromagnetic quantum critical point (QCP).

A QCP marks a zero temperature continuous phase transition tuned by an external parameter, such as doping, pressure, and disorder. In the cuprate and iron pnictide/chalcogenide phase diagrams, various experiments have suggested the existence of one or multiple "putative" QCPs, such as the antiferromagnetic QCP, the nematic QCP, and the metal-insulator QCP. Interestingly, the optimal doping and the exotic normal state properties are both achieved near one or more QCPs. This has motivated the study of various low energy effective models describing electrons coupled to quantum critical order parameter fluctuations[22, 23, 13, 14].

Similar to a continuous thermal phase transition, a QCP is characterized by a divergent correlation length $\xi \to \infty$ for the order parameter fluctuations. However, the order parameter fluctuations near a QCP are different than near a thermal critical point, in that its temporal fluctuations cannot be neglected. In particular, near a QCP, the correlation time $\xi_\tau \propto \xi^z$ also diverges, where z is called the dynamical critical exponent.

The quantum critical behavior of order parameter fluctuations extends to finite temperatures, as shown in Fig. 1.6. This can be seen by comparing the timescales associated with quantum decoherence[7] τ_q and thermal equilibration τ_{eq}. The thermal equilibration time is governed by temperature: $\tau_{\text{eq}} \sim \hbar/k_B T$. The quantum decoherence time diverges at QCP: $\tau_q \equiv \hbar/\Delta \sim \xi_\tau$, where Δ is the corresponding energy scale. If $\tau_q > \tau_{\text{eq}}$ or $\Delta < k_B T$, the thermal equilibration is faster than the quantum decoherence. As a result, the order parameter fluctuations have slow dynamics, and temporal fluctuations are important. On the other hand, if $\tau_q < \tau_{\text{eq}}$ or $\Delta > k_B T$, the quantum decoherence happens faster than thermal equilibration. As a result, the order parameter fluctuations can be treated thermally. As shown by Fig. 1.6, the crossover between quantum critical fluctuations and thermal fluctuations is marked by a "fan" above the QCP.

In the studies using QCP as an organizing principle[22, 23, 13, 14], it is argued that the coupling between quantum critical fluctuations and low energy electrons is key to

[7] Quantum decoherence time is the timescale at which order parameter fluctuations are uncorrelated. See Ch.1 of Ref. [24]

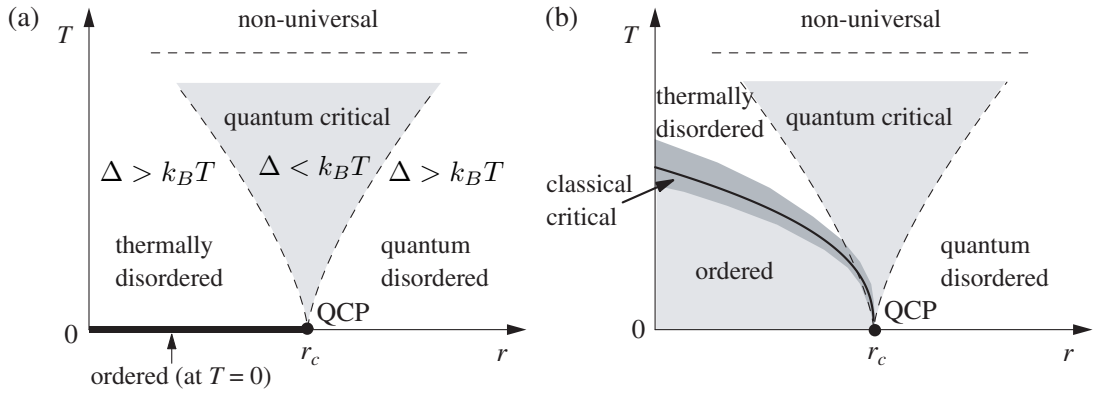

Figure 1.6: Schematic phase diagram near a QCP, adapted from Ref. [25]. r is some tunable parameter. At zero temperature, the ordered and disordered state are separated by a QCP, marked by r_c. At finite temperatures, there could be two scenarios: (a) no thermal phase transition and (b) a thermal phase transition into the ordered state. The two energy scales, k_BT and Δ, are associated with the time to thermal equilibration and quantum decoherence respectively. The order parameter fluctuations are quantum critical when $\Delta < k_BT$, marked by a fan above the QCP. The dashed lines mark the crossover from quantum critical to thermal fluctuations.

the various electronic phases and exotic normal state properties. Various studies have suggested that many of the high T_c phase diagram are indeed captured by proximity to a metallic QCP. In later chapters, I will discuss our contributions to this topic, namely, superconductivity in proximity to a metallic antiferromagnetic quantum critical point.

1.6 Overview

In this thesis, I will discuss several questions related to the electronic phase diagram of both cuprate and iron pnictide high-T_c superconductors.

In Ch. 2, I will discuss the nature and origin of the magnetic order in iron pnictide materials. I will first discuss the recent experimental observations of magnetic orders which preserve the square lattice symmetry. Based on a Ginzburg-Landau analysis, I show what these magnetic orders are, and how they can be stabilized in favor of the stripe magnetic order shown in Fig. 1.5. I will then discuss their microscopic origin in a effective three band model, and show how they emerge as Fermi surface instabilities.

Due to the lack of definitive experimental evidence for the tetragonal magnetic orders, I look at their manifestations in both the electronic (Fermi surface reconstruction) and magnetic properties (collective spin wave excitations), and discuss the features which can be used to uniquely determine the magnetic orders.

In Ch. 3, I will discuss the magnetic origin of the nematic order in iron pnictide materials, i.e., nematicity driven by strong magnetic fluctuations. At a mean field level, the nematic and magnetic phase transitions occur simultaneously. I will discuss how the nematic phase transition can be split from the magnetic phase transition when fluctuation effects are considered. I will then discuss how electronic nematicity can be measured experimentally. In particular, I will study the electronic interference patterns near a non-magnetic impurity in the nematic phase, which can be measured using spatially-resolved probes such as scanning tunneling spectroscopy.

In Ch. 4, I will switch gears and discuss the physics of superconductivity (SC) and charge density wave (CDW) near an antiferromagnetic quantum critical point. In particular, I will present our results on the so-called spin-fermion model, which is an effective model describing quantum critical spin fluctuations coupled to electrons near the Fermi surface. By a combined theoretical and numerical Quantum Monte Carlo study, I show that the microscopic system parameters governing SC and CDW are related to the special points on the Fermi surface connected by the antiferromagnetic ordering wavevector, called hot spots.

Chapter 2

Magnetism in iron-based superconductors

2.1 Introduction

In most iron pnictide/chalcogenide superconductors, superconductivity and magnetism are found near each other in the phase diagram. While some materials, such as FeSe, do not exhibit long range magnetic order, significant magnetic fluctuations are observed[20]. Understanding the nature and origin of magnetism is essential for understanding why these materials become superconducting at low temperatures. While earlier studies showed that most iron pnictide materials display stripe magnetic order accompanied by lattice tetragonal to orthorhombic transition (see Ch. 1), recent experiments[26, 27, 28, 29] on the 122 family suggest that magnetic orders without tetragonal symmetry breaking are also possible. In particular, such magnetic orders have been found in the phase diagram of $Ba_{1-x}Na_xFe_2As_2$, $Ca_{1-x}Na_xFe_2As_2$, $Sr_{1-x}Na_xFe_2As_2$, $Ba_{1-x}K_xFe_2As_2$, and $Ba(Fe_{1-x}Mn_x)_2As_2$[30]. While the first four compounds also exhibit superconductivity with doping, the last one does not. Fig. 2.1 shows a combined phase diagram of the Na-doped compounds[26].

Unlike cuprate materials, where the Néel antiferromagnetic order has long been established, both the nature and origin of magnetism in the iron pnictide/chalcogenide materials are active topics of current research.

What is the nature of the magnetic order observed in the iron pnictide materials?

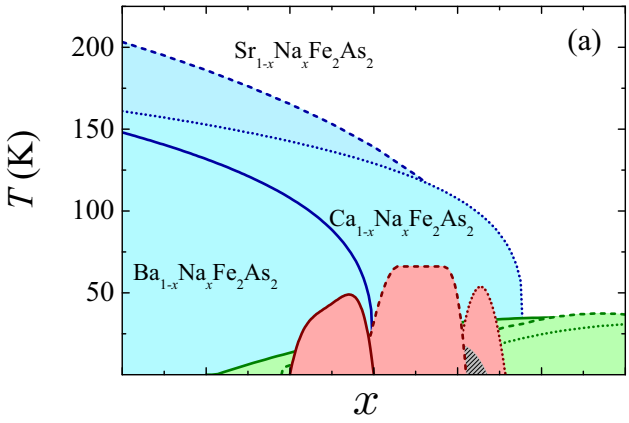

Figure 2.1: Phase diagrams of $Ba_{1-x}Na_xFe_2As_2$, $Ca_{1-x}Na_xFe_2As_2$, $Sr_{1-x}Na_xFe_2As_2$. Taken from Ref. [26]. Green region is superconducting phase, blue corresponds to stripe magnetic phase, and pink region is the tetragonal magnetic phase.

Inelastic neutron scattering measurements present an excellent characterization of the magnetic structure in these materials. Fig. 2.2 shows energy-integrated inelastic neutron scattering in $Ba(Fe_{1-x}Co_x)_2As_2$ in the Brillouin zone of the one-Fe unit cell.[1] Different families of iron pncitide/chalcogenides exhibit similar structures. The scattering intensities are peaked at wavevectors $\mathbf{Q}_1 = (\pi, 0)$ and $\mathbf{Q}_2 = (0, \pi)$, commensurate with the underlying lattice. We can therefore introduce two magnetic order parameters $\mathbf{M}_1$ and $\mathbf{M}_2$ associated with the two wavevectors, and write the real space magnetization as:

$$\mathbf{S}(\mathbf{r}) = \mathbf{M}_1 \cos(\mathbf{Q}_1 \cdot \mathbf{r}) + \mathbf{M}_2 \cos(\mathbf{Q}_2 \cdot \mathbf{r}) \tag{2.1}$$

Since $\mathbf{Q}_i$ are commensurate with the underlying lattice, due to inversion symmetry, $\mathbf{M}_i$ are real three-component vector fields.

In most of the iron pnictide materials such as $Ba(Fe_{1-x}Co_x)_2As_2$, the magnetic order is the stripe order, with either $\mathbf{M}_1$ or $\mathbf{M}_2$ being non-zero, therefore breaking lattice rotation symmetry from tetragonal (C_4) down to orthorhombic (C_2). There are two types of stripe magnetic orders, as shown in Fig. 2.3, where one has parallel spins along the x-direction, and the other along the y-direction. The magnetic scattering intensities at both $\mathbf{M}_1$ and $\mathbf{M}_2$, as shown in Fig. 2.2, are due to formation of domains.

[1] The actual unit cell contains two Fe atoms, due to the puckering of the pnictogen/chalcogen atoms. Both one-Fe and two-Fe unit cells have been used in the literature.

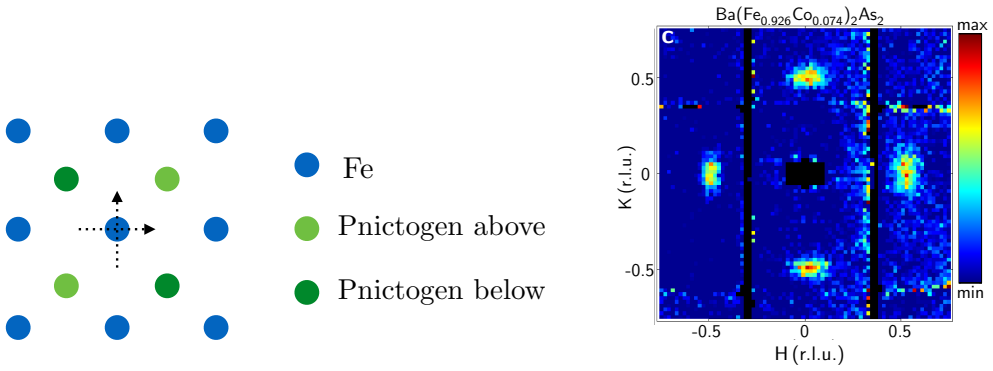

Figure 2.2: Left: schematic plot of the Fe-pnictogen plane. Fe atoms (blue) form a square lattice, and the pnictogen atoms are at the center of the square, alternating above and below the Fe plane. Right: Energy integrated inelastic neutron scattering intensity in the reciprocal space measured on $Ba(Fe_{1-x}Co_x)_2As_2$, with $x = 0.074$. From Ref. [31]. The scattering pattern is consistent for a wide range of iron pnictide superconductors. H and K are wavevectors along the Fe-Fe square lattice. The label $H/K = 0.5$ correspond to the Brillouin zone edge, i.e., $(\pi/a, 0)$ and $(0, \pi/b)$, where a,b are lattice constants along the Fe-Fe bond directions.

The domain formation is confirmed by the lattice Bragg peak splitting observed using X-ray scattering [30].

In the tetragonal magnetic phase shown in Fig. 2.1, the magnetic scattering intensities are at the same wavevectors $\mathbf{Q}_1$ and $\mathbf{Q}_2$. However, there is no tetragonal symmetry breaking from X-ray scattering measurements [30]. Such magnetic orders require $\mathbf{M}_1$ and $\mathbf{M}_2$ to be non-zero simultaneously, and have equal amplitudes $|\mathbf{M}_1| = |\mathbf{M}_2|$. The relative orientation between the two magnetic order parameters can be either 0 or 90 degrees, as will be discussed later.[2] As a result, there are two types of tetragonal magnetic orders consistent with Fig. 2.2, shown in Fig. 2.3. In the case of $\mathbf{M}_1 \perp \mathbf{M}_2$ (third figure from the left in Fig. 2.3), each of the two sublattices (labeled A,B) form a Néel antiferromagnetic order, and the local magnetic moments on the two sublattices are orthogonal to each other. This is called a "spin-vortex crystal" (SVC) order, whose name comes from the alternating vorticity defined as $\mathbf{S}_A \times \mathbf{S}_B$. In the case of $\mathbf{M}_1 \parallel \mathbf{M}_2$ (last figure of Fig. 2.3), the A sublattice has zero local magnetization $\mathbf{S}(\mathbf{r}_A) = 0$, due

[2] These tetragonal magnetic orders are also called C_4 magnetic orders or double-$\mathbf{Q}$ magnetic orders. The stripe magnetic orders are also referred to as C_2 magnetic orders or single-$\mathbf{Q}$ magnetic orders.

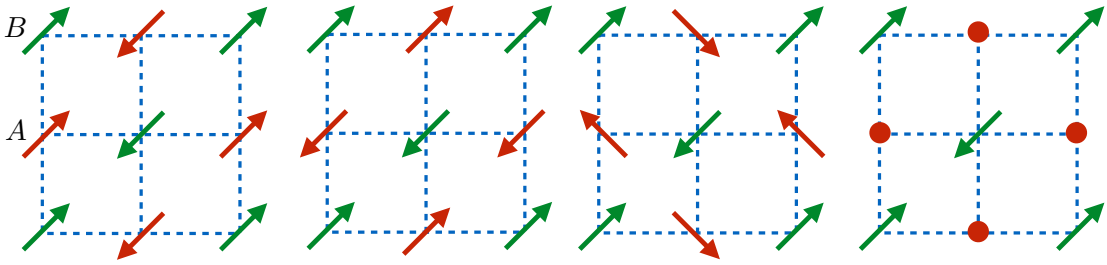

Figure 2.3: Four types of magnetic orders consistent with the inelastic neutron scattering experiment shown in Fig. 2.2. From left to right: stripe magnetic orders with ferromagnetic alignments along y and x directions, spin-vortex crystal (SVC) and charge-spin density wave (CSDW) orders that preserve lattice tetragonal symmetry. A and B label the two sublattices that exhibit Néel antiferromagnetic order.

to the cancellation between $\mathbf{M}_1$ and $\mathbf{M}_2$. The B sublattice forms a Néel antiferromagnetic order, where the local magnetization are twice as big. As will be shown later, this magnetic order also induces a charge density wave order with wavevector (π, π). It is therefore termed "charge-spin density wave" (CSDW). The tetragonal magnetic orders have been proposed and studied in Ref. [32, 33, 34, 28, 35, 36, 37, 38].

One of the main difficulties in experiments is to disentangle features coming from domains of C_2 order and true C_4 magnetic orders. The present experimental results rely on the indirect measurement of lattice Bragg peak splitting. One objective of this chapter is to find direct ways to distinguish between C_2 and C_4 magnetic orders, as well as between the two C_4 magnetic phases.

Having explained the possible types of magnetic orders in iron pnictide materials, here I briefly describe the microscopic origin responsible for them. In Sec. 2.3 I will present a detailed analysis of how each magnetic order can become the ground state.

Generally speaking, magnetism emerges as collective quantum mechanical behavior of electrons, driven by electronic interactions, i.e., screened Coulomb interaction. Depending on whether the electronic system is metallic or insulating, there are two ways how magnetic order can emerge.

In metallic systems, electrons are delocalized, and described by Bloch wavefunctions. The itinerant electrons form a conduction band, and occupy states with the lowest kinetic energies. Electrons fill the band up to the Fermi energy, which is characterized

by a Fermi surface in the momentum space. In the presence of electron-electron interactions, magnetism can emerge as a Fermi surface instability. This is the well-known "Stoner criterion". Magnetic orders due to a Fermi surface instability are itinerant in nature, and are also called spin density wave (SDW) orders. Mathematically, the Stoner criterion can be seen by writing down the spin susceptibility $\chi_{\rm mag}$ using the "random phase approximation" (RPA) of the Hubbard model discussed in Eq. 1.1:

$$\chi_{\rm mag}(\mathbf{q}, T) = \frac{\chi_0(\mathbf{q}, T)}{1 - U\chi_0(\mathbf{q}, T)} \tag{2.2}$$

Here U is the onsite Hubbard repulsion (screened Coulomb repulsion), T is the temperature, $\mathbf{q}$ the wavevector, and χ_0 the non-interacting spin susceptibility due to the Fermi surface. In the simplest case of an isotropic Fermi liquid, $\chi_0(\mathbf{q}, T \to 0) \approx N_f[1 - \frac{1}{3}(q/k_f)^2]$, where k_f is Fermi wavevector, and N_f the electronic density of states at the Fermi level. The spin susceptibility becomes divergent at $\mathbf{q} = 0$ at a critical interaction strength $1 = U_c N_f$, signaling the onset of ferromagnetic order. SDW orders with a finite ordering wavevector $\mathbf{Q}$ are possible, if the Fermi surface has special "nesting" properties, i.e., $\varepsilon_{\mathbf{k}} = -\varepsilon_{\mathbf{k}+\mathbf{Q}}$, where $\varepsilon_{\mathbf{k}}$ is the energy dispersion of the itinerant electrons. In this case, $\chi_0(\mathbf{q}, T) \approx N_f[\ln(\Lambda_c/T) - (\mathbf{q} - \mathbf{Q})^2]$, where Λ_c is some upper energy cutoff. The onset temperature of SDW order is determined by $1 = N_f U \ln(\Lambda_c/T_{\rm SDW})$. Due to nesting, there is a finite transition temperature for arbitrarily weak interactions.

In the other scenario, magnetism can emerge from a Mott insulating phase. A Mott insulator is driven due to strong electronic interactions. For a half-filled band, since there is an odd number of electrons per unit cell, the electrons should be delocalized as there is no Pauli's principle preventing it. However, strong electronic interactions prevent one electron to hop from site to site, leaving a vacancy on the original site and a double-occupancy on the other. In a Mott insulator, mobile charge degrees of freedom are frozen, however, localized electronic spins can interact with each other from "virtual hopping" [39], and the electronic model is mapped onto a spin-Heisenberg model:

$$H = J \sum_{\langle ij \rangle} \mathbf{S}_i \cdot \mathbf{S}_j \tag{2.3}$$

where $\mathbf{S} \equiv \frac{1}{2} c^\dagger \vec{\sigma} c$ is the spin operator, and $J > 0$ is the antiferromagnetic spin-spin interaction. Starting from the t-U Hubbard model, $J \propto t^2/U$[39].

The different origins for magnetism are due to a difference in the electronic interaction strength. For a weakly interacting system, electrons delocalize to form a metal, whereas for a strongly interacting system, electrons localize to become a Mott insulator. In the itinerant picture, the SDW order is driven by a gain in the Coulomb energy, while in the localized picture, magnetism is driven by a gain in the kinetic energy, i.e., tendency toward delocalization.

Which of these two pictures is more suitable for describing magnetism in iron pnictide superconductors? Combined experimental and theoretical results show that electronic interactions in these materials are in the intermediate range. On the one hand, the disordered state from which magnetism emerges is metallic. Quantum oscillations on the parent compounds of iron pnictide materials show well-defined Fermi surfaces at low temperatures[40]. On the other hand, optical conductivity measurements Ref. [41] suggest that the electronic kinetic energy in LaFeAsOP is suppressed by a factor of 2. Ref. [42] also show significant electronic mass renormalization from density function theory calculation.

In the rest of the chapter, I will address both the nature and the origin of magnetism by carefully comparing predictions of localized versus itinerant model with experimental results, and in particular, which picture is more suitable for the study of tetragonal magnetic orders. Additionally, I will propose additional experimental signatures which can be used to uniquely identify the magnetic order in iron pnictide superconductors. This chapter closely follows our published works in Ref. [35, 36, 37].

2.2 Ginzburg-Landau analysis

The discussion in this section is based on my paper Ref. [35, 36].

To see how the single-$\mathbf{Q}$ and double-$\mathbf{Q}$ magnetic orders emerge, we write down the Ginzburg-Landau free energy for the order parameters $(\mathbf{M}_1, \mathbf{M}_2)$ defined previously, constrained by $O(3)$ spin rotation and inversion symmetry and C_4 lattice rotation symmetry:

$$\mathcal{F} = \sum_{i=1,2} \left(\frac{r}{2}\mathbf{M}_i^2 + \frac{\beta}{4}\mathbf{M}_i^4 \right) + \frac{\alpha}{2}\mathbf{M}_1^2\mathbf{M}_2^2 + w(\mathbf{M}_1 \cdot \mathbf{M}_2)^2 \tag{2.4}$$

Here we introduced the notation: $\mathbf{M}_i^4 \equiv (\mathbf{M}_i^2)^2$, and $\mathbf{M}_i^2 \equiv \mathbf{M}_i \cdot \mathbf{M}_i$. $\mathbf{M}_{i=1,2}$ is a three-component vector order parameter. $r \propto T - T_N$ measures the distance to a mean-field magnetic phase transition. The coupling between $\mathbf{M}_1$ and $\mathbf{M}_2$ starts at quartic order, as the bilinear term $(\mathbf{M}_1 \cdot \mathbf{M}_2)$ has a finite momentum. The free energy can be rewritten as:

$$\mathcal{F} = \frac{r}{2}(\mathbf{M}_1^2 + \mathbf{M}_2^2) + \frac{u}{4}(\mathbf{M}_1^2 + \mathbf{M}_2^2)^2 - \frac{g}{4}(\mathbf{M}_1^2 - \mathbf{M}_2^2)^2 + w(\mathbf{M}_1 \cdot \mathbf{M}_2)^2 \tag{2.5}$$

where $u \equiv (\alpha + \beta)/2$, and $g \equiv (\alpha - \beta)/2$. This form is used in Ref. [35, 36] to analyze the possible magnetic states.

The first two terms depend only on the combination $\mathbf{M}_1^2 + \mathbf{M}_2^2$, effectively enlarging the symmetry of the system to $O(6)$, and resulting in a huge degeneracy of the magnetic ground state [33, 43]. The last two terms are responsible for lifting this degeneracy, selecting both the relative amplitudes (either $\mathbf{M}_1^2/\mathbf{M}_2^2 = 0$ or $\mathbf{M}_1^2/\mathbf{M}_2^2 = 1$) and the relative orientations of the two order parameters (either $\mathbf{M}_1 \parallel \mathbf{M}_2$ or $\mathbf{M}_1 \perp \mathbf{M}_2$). Fig. 2.4 displays the phase diagram and the resulting ground states as function of g and w at the mean-field level. For $g > \max\{0, -w\}$, we find a stripe state, characterized by $\mathbf{M}_1 \neq 0$ and $\mathbf{M}_2 = 0$ (or vice-versa), which breaks the tetragonal symmetry of the system. This is the state most commonly observed in the iron pnictides and has a residual Z_2 (Ising) symmetry, related to choosing either $\mathbf{M}_1 \neq 0$ or $\mathbf{M}_2 \neq 0$, which can be broken even before the magnetic transition takes place [44]. This residual order, called the spin-nematic order, will be the main topic of interest in Ch. 3.

For $g < \max\{0, -w\}$, minimization of the free energy leads to a tetragonal magnetic state characterized by simultaneously non-vanishing $\mathbf{M}_1^2 = \mathbf{M}_2^2$. Two different configurations are possible: for $w > 0$, we obtain the SVC state $\mathbf{M}_1 \perp \mathbf{M}_2$, see Fig. 2.4 and also Refs. [32, 33]. For $w < 0$, the ground state is given by $\mathbf{M}_1 \parallel \mathbf{M}_2$, corresponding to a CSDW state. This state induces a charge density-wave (CDW) with modulation $\mathbf{Q}_1 + \mathbf{Q}_2 = \mathbf{Q}_N$, where the odd (non-magnetic) sites have different local charge than the even (magnetic) sites. This can be seen from Eq. 2.5 by including the Ginzburg-Landau term $\zeta\, \rho_{\mathbf{Q}_N}\, (\mathbf{M}_1 \cdot \mathbf{M}_2)$ [45], which leads to a non-zero CDW order parameter $\rho_{\mathbf{Q}_N} = \chi_{\mathrm{CDW}} \zeta\, (\mathbf{M}_1 \cdot \mathbf{M}_2)$, whose amplitude depends on both the coupling constant ζ and the bare CDW susceptibility χ_{CDW}.

While the vast majority of iron pnictides display a stripe ground state, $g > \max\{0, -w\}$,

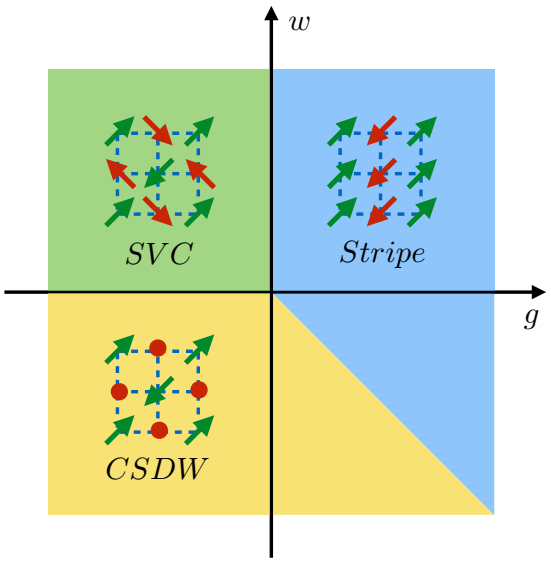

Figure 2.4: Mean field phase diagram of the Ginzburg-Landau free energy, displaying the stripe state for $g > \max\{0, -w\}$, as well as the spin-vortex crystal and charge-spin density wave states for $g < \max\{0, -w\}$. Adapted from our work Ref. [35]. See also Ref. [32, 33].

the observations of a tetragonal magnetic state [26, 27, 28, 29] indicate that a change in the microscopic system parameters can change the Ginzburg-Landau coefficients and bring the system to the regime of the double-**Q** magnetic states.

2.3 Microscopic origin for magnetism

As was briefly discussed in the introduction, depending on the electronic interaction strength, the microscopic origin for magnetism is different. In the localized picture, magnetism emerges due to spin-spin exchange interactions. In the itinerant picture, magnetism is a Fermi surface instability. Here I will elaborate both scenarios, and show how the three types of magnetic orders can/cannot emerge from each scenario. In particular, as I will show later, neither of the two C_4 magnetic orders (CSDW and SVC) can be obtained from a localized J_1-J_2 Heisenberg model, whereas in an itinerant picture, they appear naturally due to the low-energy electronic properties.

2.3.1 Multi-orbital Hubbard model for iron pnictide materials

As has been discussed in Ch. 1, due to the crystal environment and the $3d^6$ electronic configuration of Fe^{2+}, a low-energy description of the iron pnictide materials should include all five d orbitals. A microscopic model is the multi-orbital Hubbard model, discussed in Ref. [21]. The kinetic Hamiltonian is described as:

$$\mathcal{H}_0 = \sum_{ij,\mu\nu} \sum_{\sigma} t_{\mu i,\nu j} d^{\dagger}_{\mu,i\sigma} d_{\nu,j\sigma} \tag{2.6}$$

where $d^{\dagger}_{\mu,i\sigma}$ creates an electron at site i and orbital $\mu = 1...5$ with spin state σ. $t_{\mu i,\nu j}$ are hopping amplitudes. The diagonal terms describe the band dispersions of electrons from separate orbitals, while the off-diagonal terms describe the hybridization. Due to the multi-orbital nature, there are at least four onsite interaction terms:

$$\begin{aligned} \mathcal{H}_{\text{int}} = & U \sum_{i,\mu} n_{\mu,i\uparrow} n_{\mu,i\downarrow} + J \sum_{i,\mu<\nu} \sum_{\sigma,\sigma'} d^{\dagger}_{\mu,i\sigma} d^{\dagger}_{\nu,i\sigma'} d_{\mu,i\sigma'} d_{\nu,i\sigma} \\ & + U' \sum_{i,\mu<\nu} n_{\mu,i} n_{\nu,i} + J' \sum_{i,\mu\neq\nu} d^{\dagger}_{\mu,i\uparrow} d^{\dagger}_{\mu,i\downarrow} d_{\nu,i\downarrow} d_{\nu,i\uparrow} \end{aligned} \tag{2.7}$$

Here U is the usual Hubbard repulsion between electrons on the same orbitals, U' is the onsite repulsion between electrons on different orbitals, J is the Hund's exchange that tends to align spins at different orbitals, and J' is another exchange term, often called the pair-hopping term.

Eq. 2.6 and 2.7 defines the five-orbital Hubbard model. This is a very complicated model to solve beyond self-consistent mean field theory, in particular, if the kinetic term and the interaction term are comparable. In the following sections, I describe the two limits where we can have tractable analytical solutions in regards to magnetism, namely, the strong coupling limit and the weak coupling limit.

2.3.2 Localized J_1-J_2 Heisenberg model

If the electronic interactions are strong, we can project out the charge degrees of freedom, to arrive at some form of spin-Heisenberg model. However, due to the multi-orbital nature, the projection is quite complicated[46, 47]. Instead, a Heisenberg model with both nearest-neighbor (J_1) and next-nearest-neighbor (J_2) antiferromagnetic interactions has been proposed as a phenomenological model. The Heisenberg Hamiltonian is

defined as:

$$H = J_1 \sum_{\langle ij \rangle} \mathbf{S}_i \cdot \mathbf{S}_j + J_2 \sum_{\langle\langle ij \rangle\rangle} \mathbf{S}_i \cdot \mathbf{S}_j \tag{2.8}$$

where $\langle \cdots \rangle$ and $\langle\langle \cdots \rangle\rangle$ label nearest neighbor and next-nearest-neighbor respectively. Depending on the ratio of J_1/J_2, different magnetic orders are stabilized.

Classically, when $J_1/J_2 > 2$, the ground state is the Néel antiferromagnetic order, with nearest-neighbor spins antiparallel to each other. When $J_1/J_2 < 2$, the next-nearest-neighbor interaction is dominant, and the lattice splits into two sublattices of Néel order along the diagonal directions, see Fig. 2.3. At a classical level, the relative angle θ between spin orientations on the two sublattices is not fixed by $J_1 \neq 0$. This is because any given spin on one sublattice is surrounded by four neighboring spins on a different sublattice, and due to the Néel configuration, the average interaction is zero. Quantum and thermal fluctuations can break this classical degeneracy, and favor $\theta = 0$ or π, corresponding to either of the two stripe configurations described in Fig. 2.3. This is the so-called "order-from-disorder" effect studied in Ref. [48]. Microscopically, the effect of quantum and thermal fluctuations can be incorporated into a biquadratic interaction between nearest-neighbors:

$$H = J_1 \sum_{\langle ij \rangle} \mathbf{S}_i \cdot \mathbf{S}_j + J_2 \sum_{\langle\langle ij \rangle\rangle} \mathbf{S}_i \cdot \mathbf{S}_j - K \sum_{\langle ij \rangle} (\mathbf{S}_i \cdot \mathbf{S}_j)^2 \tag{2.9}$$

where $K > 0$ favors the stripe state at classical level. For $K < 0$, the ground state has $\theta = \pi/2$, corresponding to the SVC order shown in Fig. 2.3. However, I emphasize that $K < 0$ *cannot* be achieved by the order from disorder phenomenon of the J_1-J_2 Heisenberg model.

It is obvious to see that the CSDW phase cannot be achieved in the J_1-J_2-K Heisenberg model, which always has a finite (fixed) magnetization at every Fe site. The absence of either of the C_4 magnetic orders (SVC and CSDW) is a main result from the study of this simple localized spin-Heisenberg Hamiltonian.

2.3.3 Itinerant picture and the three band model

This section is written based on my work Ref. [35, 36].

In the weak coupling scenario, the electronic interactions in Eq. 2.7 are small compared to the bandwidth, and electrons are delocalized to form a conduction band. In

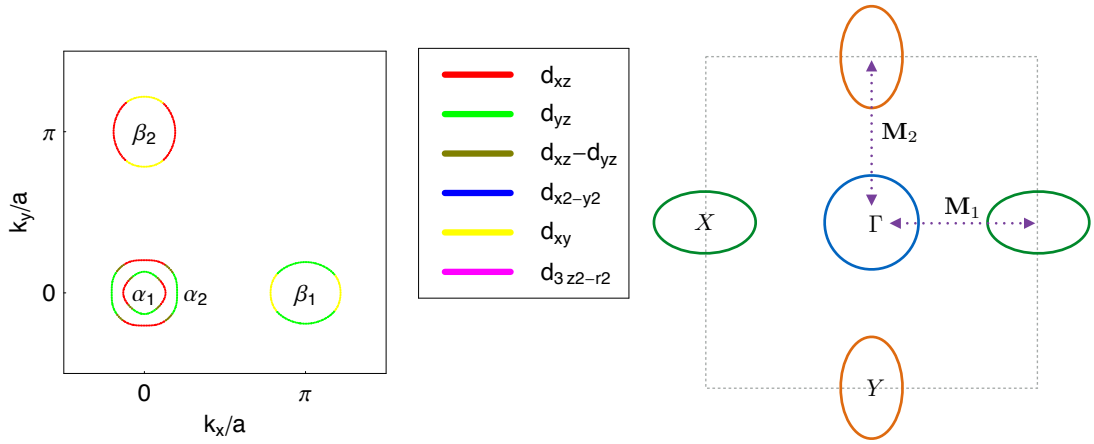

Figure 2.5: Left: Fermi surface obtained from tight-binding fit to LDA calculations of iron pnictide band structure. Taken from Ref. [49]. Right: Simplified three band model describing itinerant magnetism.

the itinerant picture, magnetism comes from Fermi surface instability. Below I will first discuss how the Ginzburg-Landau free energy can be obtained from the itinerant picture, following the Hertz-Millis approach[22, 23]. Then I will discuss the microscopic origins of how various magnetic orders can be stabilized.

The outer shell of the Fe^{2+} ion has $3d^6$ configuration. LDA calculation shows that all five Fe $3d$ orbitals are located near the Fermi level[50]. Fig. 2.5 shows a tight binding fit of the Fermi surface to the LDA calculation [49]. There are two hole-like Fermi pockets centered at the Γ point (zone center), and two electron-like Fermi pockets centered at X and Y (zone boundary).

The outer hole pocket and the electron pockets are of similar sizes, and are quasi-nested ($\varepsilon_{h,\mathbf{k}} \approx -\varepsilon_{e_i,\mathbf{k}+\mathbf{Q}_i}$) with wavevector $\mathbf{Q}_i$. As a result, the charge/spin fluctuations with $\mathbf{Q}_i$ are strongly enhanced by the nesting of the Fermi surface. To study magnetism in the itinerant picture, it is convenient to neglect the orbital character of the Fermi surface, and work in the band basis. The small internal hole pocket can also be neglected because it is less nested with other Fermi surfaces. As a result, we can construct a low-energy effective three-band model as depicted in Fig. 2.5. The band dispersions of the

hole and electron pockets can be approximated as[33]:

$$\begin{aligned}\varepsilon_{h,\mathbf{k}} &= \epsilon_0 - \frac{k^2}{2m} - \mu \\ \varepsilon_{e_1,\mathbf{k}+\mathbf{Q}_1} &= -\epsilon_0 + \frac{k_x^2}{2m_x} + \frac{k_y^2}{2m_y} - \mu \\ \varepsilon_{e_2,\mathbf{k}+\mathbf{Q}_2} &= -\epsilon_0 + \frac{k_x^2}{2m_y} + \frac{k_y^2}{2m_x} - \mu\end{aligned} \tag{2.10}$$

where μ is the chemical potential, ϵ_0 an energy shift, and $m_x \neq m_y$ defines the ellipticity of the electron pockets. Close to particle-hole symmetry (perfect nesting), we can rewrite the band dispersions in a more convenient form:

$$\begin{aligned}\varepsilon_{h,\mathbf{k}} &= -\varepsilon_{\mathbf{k}} \\ \varepsilon_{e_1,\mathbf{k}+\mathbf{Q}_1} &= \varepsilon_{\mathbf{k}} - (\delta_\mu + \delta_m \cos 2\theta) \\ \varepsilon_{e_2,\mathbf{k}+\mathbf{Q}_2} &= \varepsilon_{\mathbf{k}} - (\delta_\mu - \delta_m \cos 2\theta)\end{aligned} \tag{2.11}$$

where θ is the angle around the Fermi surface. The parameter δ_μ is related to the occupation number (doping) and δ_m to the ellipticity of the electron pockets:

$$\begin{aligned}\delta_\mu &= 2\mu + \epsilon_F \left[1 - \frac{m}{2}\left(\frac{m_x + m_y}{m_x m_y}\right)\right] \\ \delta_m &= \frac{\epsilon_F m}{2}\left(\frac{m_x - m_y}{m_x m_y}\right)\end{aligned} \tag{2.12}$$

The non-interacting Hamiltonian is given by $H_0 = \sum_{\mathbf{k},a} \varepsilon_{\mathbf{k},a} c^\dagger_{a,\mathbf{k}\alpha} c_{a,\mathbf{k}\alpha}$, with band index a and spin index α.

Following Ref. [51, 52], there are eight types of purely electronic interactions connecting the three Fermi pockets which preserves the spin rotation symmetry. They are the density-density (U_1, U_4, U_5, U_6), spin-exchange (U_2, U_7) and pair-hopping (U_3, U_8) interactions respectively. The interaction Hamiltonian is:

$$\begin{aligned}H_{\text{int}} = {} & U_1 \sum c^\dagger_{h\alpha} c^\dagger_{e_i\beta} c_{e_i\beta} c_{h\alpha} + U_2 \sum c^\dagger_{h\alpha} c^\dagger_{e_i\beta} c_{h\beta} c_{e_i\alpha} \\ & + \frac{U_3}{2} \sum (c^\dagger_{h\alpha} c^\dagger_{h\beta} c_{e_i\beta} c_{e_i\alpha} + \text{h.c.}) \\ & + \frac{U_4}{2} \sum c^\dagger_{e_i\alpha} c^\dagger_{e_i\beta} c_{e_i\beta} c_{e_i\alpha} + \frac{U_5}{2} \sum c^\dagger_{h\alpha} c^\dagger_{h\beta} c_{h\beta} c_{h\alpha} \\ & + U_6 \sum c^\dagger_{e_1\alpha} c^\dagger_{e_2\beta} c_{e_2\beta} c_{e_1\alpha} + U_7 \sum c^\dagger_{e_1\alpha} c^\dagger_{e_2\beta} c_{e_1\beta} c_{e_2\alpha} \\ & + \frac{U_8}{2} \sum (c^\dagger_{e_1\alpha} c^\dagger_{e_1\beta} c_{e_2\beta} c_{e_2\alpha} + \text{h.c.})\end{aligned} \tag{2.13}$$

For simplicity of notation, the momentum indices are all suppressed with the implicit constraint of momentum conservation. Note that such eight types of interactions can be derived from a microscopic Hamiltonian, e.g., the multi-orbital Hubbard model described in Eq. 2.6.

To study the instability towards magnetic order, we project all the interactions in the spin-density wave (SDW) channel – which is the leading one according to RG and fRG calculations [52, 53]. The only interactions that contribute directly to the SDW instability are U_1 and U_3. The partition function, restricted to this channel only, can then be written in the functional field form:

$$\mathcal{Z} = \int \mathcal{D}c^\dagger \mathcal{D}c \ \exp(-S) \tag{2.14}$$

with the action:

$$S = \int_0^\beta \mathrm{d}\tau \ \sum_{i\mathbf{k}\sigma} c^\dagger_{i\mathbf{k}\sigma} \partial_\tau c_{i\mathbf{k}\sigma} + H_0 + H_{\mathrm{SDW}} \tag{2.15}$$

and the SDW-decoupled interaction:

$$H_{\mathrm{SDW}} = -I \sum_{i\mathbf{k}\mathbf{k}'\mathbf{q}} \left(c^\dagger_{h\mathbf{k}\alpha} \boldsymbol{\sigma}_{\alpha\beta} c_{e_i\mathbf{k}+\mathbf{q}\beta} \right) \cdot \left(c^\dagger_{e_i\mathbf{k}'\gamma} \boldsymbol{\sigma}_{\gamma\delta} c_{h\mathbf{k}'-\mathbf{q}\delta} \right) \tag{2.16}$$

where $I = U_1 + U_3$. We now introduce the Hubbard-Stratonovich field $\mathbf{M}_i$, whose mean value is proportional to the staggered magnetization with ordering vector $\mathbf{Q}_i$, i.e. $\langle \mathbf{M}_i \rangle = I \sum_{\mathbf{k}} \left\langle c^\dagger_{h\mathbf{k}\alpha} \boldsymbol{\sigma}_{\alpha\beta} c_{e_i\mathbf{k}+\mathbf{q}\beta} \right\rangle$, via $\exp\left(-H_{\mathrm{SDW}}\right) \propto \int \mathcal{D}\mathbf{M}_i \exp\left(-S_{\mathrm{SDW}}\left[\mathbf{M}_i\right]\right)$ with:

$$S_{\mathrm{SDW}}\left[\mathbf{M}_i\right] = \sum_{i\mathbf{q}} \frac{\mathbf{M}_{i\mathbf{q}} \cdot \mathbf{M}_{i-\mathbf{q}}}{I} - \sum_{i\mathbf{q}\mathbf{k}} \left(\mathbf{M}_{i\mathbf{q}} \cdot c^\dagger_{e_i\mathbf{k}\gamma} \boldsymbol{\sigma}_{\gamma\delta} c_{h\mathbf{k}-\mathbf{q}\delta} + \mathrm{h.c.} \right) \tag{2.17}$$

Following Ref. [44], we then integrate out the electronic degrees of freedom, obtaining an effective action for the magnetic degrees of freedom:

$$\begin{aligned} \mathcal{Z} &= \int \mathcal{D}c^\dagger \mathcal{D}c \, \mathcal{D}\mathbf{M}_i \ \exp\left(-S\left[c^\dagger, \mathbf{M}_i \right] \right) \\ &= \int \mathcal{D}\mathbf{M}_i \ \exp\left(-S_{\mathrm{eff}}\left[\mathbf{M}_i\right]\right) \end{aligned} \tag{2.18}$$

For a finite-temperature magnetic transition, $S_{\mathrm{eff}}\left[\mathbf{M}_i\right] = F\left[\mathbf{M}_i\right]/T$, where $F\left[\mathbf{M}_i\right]$ is the free energy. Near the magnetic transition, we can expand the action in powers of the magnetic order parameters, deriving the Ginzburg-Landau expansion:

$$S_{\mathrm{eff}}\left[\mathbf{M}_i\right] = \frac{r}{2}(\mathbf{M}_1^2 + \mathbf{M}_2^2) + \frac{u}{4}(\mathbf{M}_1^2 + \mathbf{M}_2^2)^2 - \frac{g}{4}(\mathbf{M}_1^2 - \mathbf{M}_2^2)^2 + w(\mathbf{M}_1 \cdot \mathbf{M}_2)^2 \tag{2.19}$$

This is identical to the phenomenological Ginzburg-Landau free energy presented in Eq. 2.5, but now the coefficients are given microscopically. In the vicinity of the magnetic transition, $r \approx N_f(T - T_N)$, where N_f is the density of states at the Fermi surface. The coefficients u, g, and w are given by [44]:

$$u = A + B;\ g = B - A;\ w = 0 \tag{2.20}$$

with:

$$\begin{aligned} A &= \int_k G_{h,\mathbf{k}}^2 G_{e_1,\mathbf{k}+\mathbf{Q}_1}^2 \\ &= \int_k \left(\frac{1}{i\omega_n + \varepsilon_{\mathbf{k}}}\right)^2 \left(\frac{1}{i\omega_n - \varepsilon_{\mathbf{k}} + \delta_\mu + \delta_m \cos 2\theta}\right)^2 \\ B &= \int_k G_{h,\mathbf{k}}^2 G_{e_1,\mathbf{k}+\mathbf{Q_1}} G_{e_2,\mathbf{k}+\mathbf{Q}_2} \\ &= \int_k \left(\frac{1}{i\omega_n + \varepsilon_{\mathbf{k}}}\right)^2 \frac{1}{i\omega_n - \varepsilon_{\mathbf{k}} + \delta_\mu + \delta_m \cos 2\theta} \frac{1}{i\omega_n - \varepsilon_{\mathbf{k}} + \delta_\mu - \delta_m \cos 2\theta} \end{aligned} \tag{2.21}$$

Here, $G_{a,\mathbf{k}}$ is the non-interacting fermionic Green's function for pocket a, $G_{a,\mathbf{k}}^{-1} = i\omega_n - \varepsilon_{a,\mathbf{k}}$, and $\int_k \to T\sum_n \int \frac{d\mathbf{k}}{(2\pi)^d}$, with Matsubara frequency $\omega_n = (2n+1)\,\pi T$. After integrating out the momentum, we obtain:

$$\begin{aligned} A &= N_f T\pi \sum_{n=0}^{\infty} \mathrm{Im} \int_\theta \frac{1}{\left(i\omega_n + \frac{\delta_\mu}{2} + \frac{\delta_m}{2}\,\cos 2\theta\right)^3} \\ B &= N_f T\pi \sum_{n=0}^{\infty} \mathrm{Im} \int_\theta \frac{i\omega_n + \frac{\delta_\mu}{2}}{\left(\left(i\omega_n + \frac{\delta_\mu}{2}\right)^2 - \left(\frac{\delta_m}{2}\,\cos 2\theta\right)^2\right)^2} \end{aligned} \tag{2.22}$$

with $\int_\theta = \int_0^{2\pi} \frac{d\theta}{2\pi}$.

In the limit of perfect nesting (i.e. $\delta_\mu = \delta_m = 0$) one obtains $g = w = 0$, implying that the system has an enlarged $O(6)$ symmetry and a huge ground-state degeneracy. Expanding near perfect nesting yields $w = 0$ and:

$$u = \int_k G_{h,k}^2 \left(G_{e_1,k} + G_{e_1,k}\right)^2 \approx \frac{7\zeta(3) N_F}{2\pi^2 T^2} \tag{2.23}$$

$$g = \int_k G_{h,k}^2 \left(G_{e_2,k} - G_{e_2,k}\right)^2 \approx \frac{31\zeta(5) N_F}{32\pi^4 T^2} \left(\frac{\delta_m}{T}\right)^2 > 0 \tag{2.24}$$

This places the system in the regime of a stripe magnetic state (see Fig. 2.4). Similar free energy calculations considering other types of band dispersions also find that the stripe state is favored for a wide range of parameters, consistent with the observations that most iron pnictides display this magnetic ordered state [32, 34, 54, 55].

How can C_4 magnetic phases be favored in this itinerant model? Below I discuss two effects that can drive a phase transition from the C_2 magnetic phase to the C_4 magnetic phases, namely, moving away from perfect nesting, based on my paper Ref. [36], and the effect of Néel antiferromagnetic fluctuations based on my paper Ref. [35].

2.3.4 Away from perfect nesting

This section is written based on my paper Ref. [36].

In the previous section, we showed that within the microscopic three-band model, small deviations from perfect-nesting lead to a stripe magnetic order. In this section, we show that strong deviations from particle-hole symmetry (perfect nesting) favor a tetragonal magnetic state over the stripe state. Interestingly, the SVC state is selected by a residual electronic interaction that does not participate explicitly in the formation of the magnetic state (Ref. [33]). These theoretical results are complementary to those reported in Ref. [28, 29, 26], which found that deep inside the stripe ordered state a second instability towards a tetragonal magnetic state emerges.

The previous analysis of the Ginzburg-Landau coefficients (2.22) in Ref. [44] focused on the regime near perfect nesting, where $\delta_\mu, \delta_m \ll T$. In this case, $g \propto \delta_m^2 > 0$ and the ground state is the stripe magnetic one. Here, we extend the analysis beyond small deviations from perfect nesting by numerically computing Eqs. 2.22 for arbitrary δ_μ/T, δ_m/T.[3]

The effect of doping is mimicked by changing the parameter δ_μ (proportional to the carrier concentration) for a fixed value of the ellipticity δ_m. Note that Eq. 2.22 implies that the behavior of u and g depend only on $|\delta_\mu|$. Fig 2.6 shows the results for $\delta_m/T = 0.8\pi$ and $\delta_m/T = 2\pi$. For small values of $|\delta_\mu|$, both u and g are positive, and the stripe magnetic state is favored. However, as $|\delta_\mu|$ becomes larger, regardless of the value

[3] Here $T \approx T_N$. The constraint $\delta_m \geq \delta_\mu$ is imposed to ensure that hot spots are present, as seen experimentally. Hot spots are locations on the electron/hole Fermi surfaces that are connected by the SDW wavevector $\mathbf{Q}_{i=1,2}$.

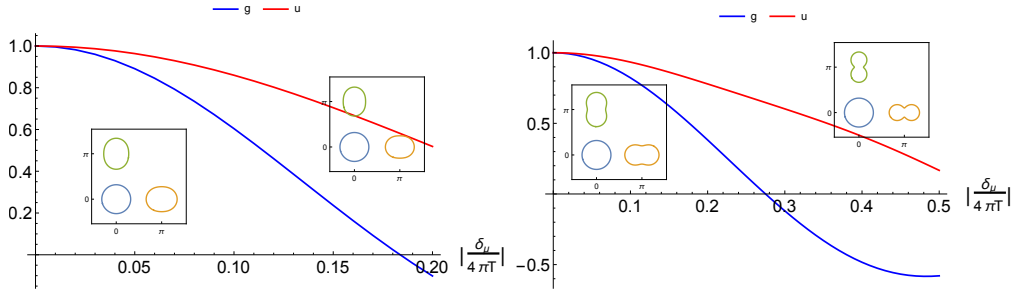

Figure 2.6: Quartic Ginzburg-Landau coefficients u (red) and g (blue) of the free energy (2.19) as function of $|\delta_\mu|/(4\pi T)$ for $\delta_m/(4\pi T) = 0.2$ (top) and $\delta_m/(4\pi T) = 0.5$ (bottom). The insets show the shape of the Fermi pockets for $\frac{\delta_\mu}{4\pi T} = -0.05$ and -0.2 in the top panel, $\frac{\delta_\mu}{4\pi T} = -0.1$ and -0.4 in the bottom panel. Note that u and g are normalized by their values at $\delta_\mu = 0$. For $g > 0$, the magnetic ground state is the stripe state, which lowers the tetragonal symmetry to orthorhombic. For $g < 0$, tetragonal symmetry is preserved, and either of the double-**Q** magnetic state (SVC and CDW) arises. Notice that the free energy remains bounded as long as $u > 0$. From Ref. [36].

of δ_m, g becomes negative, indicating that the magnetic ground state becomes a double-**Q** tetragonal phase. The evolution of the Fermi surfaces as $|\delta_\mu|$ increases, for the case of hole-doping, is shown in the insets. Since u remains positive when g first changes sign, the free energy remains bounded, i.e. the mean-field transition is second-order. These results are in qualitative agreement with the phase diagrams of $(Ba_{1-x}K_x)Fe_2As_2$, and $(Ba_{1-x}Na_x)Fe_2As_2$, which display the tetragonal magnetic phase only for sufficiently large doping concentration.

Because $w = 0$ in our model, when g becomes negative the system does not distinguish between the two possible tetragonal magnetic states, namely, the SVC order ($w > 0$, $\mathbf{M}_1 \perp \mathbf{M}_2$) and the CSDW order ($w < 0$, $\mathbf{M}_1 \parallel \mathbf{M}_2$). Although the terms arising purely from the band structure do not contribute to the w coefficient, the residual interactions in Eq. 2.13 that do not participate in the SDW instability (namely U_2, U_4, U_5, U_6, U_7, and U_8) give rise to such a term, as pointed out in Ref. [33]. Computing

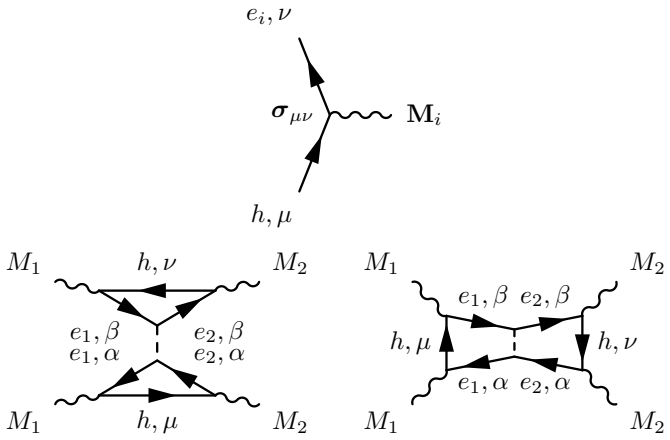

Figure 2.7: Top panel: The vertex that couples the magnetic order parameter to the low-energy fermionic states, which has a $\mathbf{M}_i \cdot \boldsymbol{\sigma}$ structure. Solid lines refer to the non-interacting electronic Green's functions. Bottom panel: the Feynman diagrams containing the leading-order corrections to the free energy arising from the residual U_7 interaction, denoted by the dashed line. From Ref. [36].

the contributions of the residual interactions to the action, we obtain:

$$\begin{aligned}\tilde{S}\left[\mathbf{M}_i\right] = & \frac{1}{4}\left(-\tilde{u}_2+\tilde{u}_4+\tilde{u}_5+\tilde{u}_6-\tilde{u}_7+\tilde{u}_8\right)\left(\mathbf{M}_1^2+\mathbf{M}_2^2\right)^2 \\ & -\frac{1}{4}\left(-\tilde{g}_4+\tilde{g}_6-\tilde{g}_7+\tilde{g}_8\right)\left(\mathbf{M}_1^2-\mathbf{M}_2^2\right)^2 \\ & +\tilde{w}_7\left(\mathbf{M}_1\cdot\mathbf{M}_2\right)^2 \end{aligned} \tag{2.25}$$

The Ginzburg-Landau coefficients can be obtained in a straightforward way using diagrammatics. In Fig. 2.7 we show the two diagrams arising from the U_7 interaction, which contribute to $\tilde{u}_7$, $\tilde{g}_7$, and $\tilde{w}_7$. Additional computational details are discussed in

the appendix to Ref. [36]. The coefficients of the quartic symmetric term are given by:

$$\begin{aligned}
\tilde{u}_2 &= 8U_2 \left(\int_k G_{h,\mathbf{k}} G^2_{e_1,\mathbf{k}+\mathbf{Q}_1} \right) \left(\int_k G^2_{h,\mathbf{k}} G_{e_1,\mathbf{k}+\mathbf{Q}_1} \right) \\
\tilde{u}_4 &= 2U_4 \left(\int_k G_{h,\mathbf{k}} G^2_{e_1,\mathbf{k}+\mathbf{Q}_1} \right)^2 \\
\tilde{u}_5 &= 4U_5 \left(\int_k G^2_{h,\mathbf{k}} G_{e_1,\mathbf{k}+\mathbf{Q}_1} \right)^2 \\
\tilde{u}_6 &= 2U_6 \left[2 \left(\int_k G_{h,\mathbf{k}} G^2_{e_1,\mathbf{k}+\mathbf{Q}_1} \right)^2 - \left(\int_k G_{h,\mathbf{k}} G_{e_1,\mathbf{k}+\mathbf{Q}_1} G_{e_2,\mathbf{k}+\mathbf{Q}_2} \right)^2 \right] \\
\tilde{u}_7 &= 2U_7 \left(\int_k G_{h,\mathbf{k}} G^2_{e_1,\mathbf{k}+\mathbf{Q}_1} \right)^2 \\
\tilde{u}_8 &= 2U_8 \left(\int_k G_{h,\mathbf{k}} G_{e_1,\mathbf{k}+\mathbf{Q}_1} G_{e_2,\mathbf{k}+\mathbf{Q}_2} \right)^2
\end{aligned} \tag{2.26}$$

whereas the coefficients of the quartic anti-symmetric term read:

$$\begin{aligned}
\tilde{g}_4 &= 2U_4 \left(\int_k G_{h,\mathbf{k}} G^2_{e_1,\mathbf{k}+\mathbf{Q}_1} \right)^2 \\
\tilde{g}_6 &= 2U_6 \left[2 \left(\int_k G_{h,\mathbf{k}} G^2_{e_1,\mathbf{k}+\mathbf{Q}_1} \right)^2 - \left(\int_k G_{h,\mathbf{k}} G_{e_1,\mathbf{k}+\mathbf{Q}_1} G_{e_2,\mathbf{k}+\mathbf{Q}_2} \right)^2 \right] \\
\tilde{g}_7 &= 2U_7 \left(\int_k G_{h,\mathbf{k}} G^2_{e_1,\mathbf{k}+\mathbf{Q}_1} \right)^2 \\
\tilde{g}_8 &= 2U_8 \left(\int_k G_{h,\mathbf{k}} G_{e_1,\mathbf{k}+\mathbf{Q}_1} G_{e_2,\mathbf{k}+\mathbf{Q}_2} \right)^2
\end{aligned} \tag{2.27}$$

and the coefficient of the quartic scalar-product term yields:

$$\tilde{w}_7 = 4U_7 \left(\int_k G_{h,\mathbf{k}} G_{e_1,\mathbf{k}+\mathbf{Q}_1} G_{e_2,\mathbf{k}+\mathbf{Q}_2} \right)^2 \tag{2.28}$$

At perfect nesting, an overall factor proportional to the Green's functions product $\left(\int_k G^2_{h,\mathbf{k}} G_{e_1,\mathbf{k}+\mathbf{Q}_1} \right)^2$ appears in all terms. In this limit, our results become identical to those found in Ref. [33], which computed the corrections to the magnetic ground state energy in the ordered state using a sequence of Bogoliubov transformations. In the paramagnetic state, however, which is our case of interest, this Green's functions product vanishes – as also pointed out in Ref. [33]. The corrections due to the residual interactions naturally become non-zero – and in fact positive – once one considers small

deviations from perfect nesting. For $\tilde{w}_7$, we find:

$$\tilde{w}_7 \approx 4U_7 \left(\frac{7\zeta(3) N_f \delta_\mu}{8\pi^2 T^2} \right)^2 \tag{2.29}$$

Because the band dispersions do not contribute to the term $(\mathbf{M}_1 \cdot \mathbf{M}_2)^2$, the fact that $\tilde{w}_7 > 0$ is very important, as it implies that the residual interaction U_7 selects the SVC state over the CSDW state (assuming that $U_7 > 0$, as one would expect). Therefore, when $g_{\text{eff}} = g + \tilde{g}$ changes sign, the system tends to form the SVC state shown in Fig. 2.3 and Fig. 2.4. Dimensional analysis of the relevant Feynman diagrams reveals that $\tilde{g}/g \propto U_i N_f$, where U_i is the appropriate combination of residual interactions. Therefore, in our weak-coupling approach, because $U_i N_f \ll 1$, it follows that $\tilde{g} \ll g$ – unless g itself is close to zero. As a result, although the contribution from $\tilde{g}$ may change slightly the value of δ_μ for which $g_{\text{eff}} = g + \tilde{g}$ vanishes, it cannot preclude the sign-changing found in Fig. 2.6 from taking place. The case of $w_{\text{eff}} = w + \tilde{w}$ is fundamentally different, since $w = 0$, making $\tilde{w}$ the leading non-vanishing term.

To conclude, although small deviations from perfect nesting ($\delta_\mu/T \ll 1$ and $\delta_m/T \ll 1$) favor a stripe magnetic order, the tetragonal magnetic orders (SVC and CSDW) can be favored for large doping levels. The residue electronic interaction U_7, which is a spin-exchange interaction between the two electron pockets centered at X and Y, favors the SVC order over the CSDW order.

2.3.5 Néel antiferromagnetic fluctuations

This section is written based on our paper Ref. [35].

One of the first observations of C_4 magnetism was in $Ba(Fe_{1-x}Mn_x)_2As_2$ [30, 31]. Fig. 2.8 shows the phase diagram as a function of Mn concentration, taken from Ref. [30]. At about 10% Mn doping, the material goes from a stripe magnetic order with measurable orthorhombic distortion to a magnetic order where the tetragonal symmetry is restored. Additionally, unlike the $Ba(Fe_{1-x}Co_x)_2As_2$ compounds, there is no sign of superconductivity in the Mn-doped compound. A key observation from inelastic neutron scattering experiments is that upon Mn doping, in addition to the intensities at $\mathbf{Q}_1$ and $\mathbf{Q}_2$, there is also significant Néel fluctuations at $\mathbf{Q}_{\text{Néel}} \equiv (\pi, \pi)$. This is presented in Fig. 2.8. The Néel fluctuations are most likely due to Mn dopants acting like local magnetic moments, evidenced by the fact that the compound $BaMn_2As_2$ is an insulating

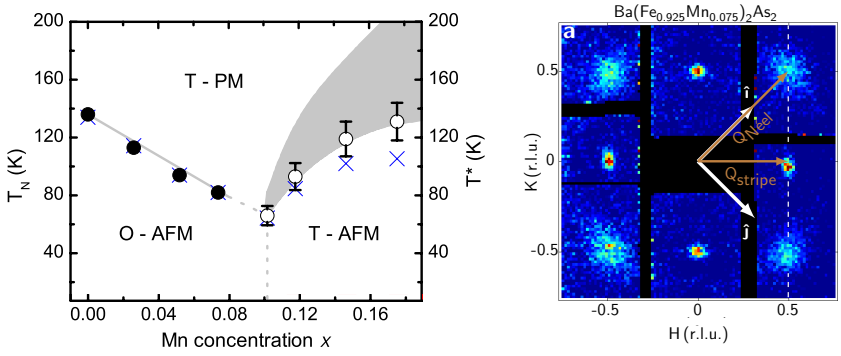

Figure 2.8: Left panel: Phase diagram of $Ba(Fe_{1-x}Mn_x)_2As_2$ as a function of Mn concentration x, from Ref. [30]. At $x < 0.12$, the magnetic order is stripe type, evidenced by the splitting of Bragg peaks observed in X-ray scattering. At $x > 0.12$, the peak splitting abruptly goes to zero, while magnetism of a similar wavevector persists. Right panel: energy-integrated inelastic neutron scattering intensity, from Ref. [31]. In addition to the wavevectors $\mathbf{Q}_{i=1,2}$, there is a diffusive peak at $\mathbf{Q}_{\text{Néel}}$, suggesting Néel antiferromagnetic fluctuations due to local moments on Mn dopants.

Néel antiferromagnet[56, 57].

To make contact with the $Ba(Fe_{1-x}Mn_x)_2As_2$ compounds, we include the coupling between the conduction electrons and the Néel fluctuations induced by the local moments. We denote by $\mathbf{N}$ the collective field associated with these Néel fluctuations, and by $\chi_N(\mathbf{q})$ the corresponding momentum-dependent susceptibility. They couple to the itinerant electrons within the three band model (Eq. 2.11) according to [58]:

$$H_N = \sum_{\mathbf{k}} \mathbf{N} \cdot \left(c^{\dagger}_{e_1,\mathbf{k}+\mathbf{Q}_1\alpha} \boldsymbol{\sigma}_{\alpha\beta} c_{e_2,\mathbf{k}+\mathbf{Q}_2\beta} \right) \tag{2.30}$$

where, for simplicity, the coupling constant was incorporated to $\mathbf{N}$. To determine how the magnetic instability is affected by short-range Néel fluctuations, we derive the coefficients of the free energy (Eq. 2.5) from the Hamiltonian $H_0 + H_{SDW} + H_N$. The leading corrections are quadratic in $\mathbf{N}$, and:

$$\begin{aligned} \delta F = & \frac{\alpha}{2} N^2 \left(\mathbf{M}_1^2 + \mathbf{M}_2^2 \right) - 4\lambda_{12} \left[(\mathbf{M}_1 \times \mathbf{M}_2) \cdot \mathbf{N} \right]^2 \\ & + \left(\frac{4\lambda_{11} + 8\lambda_{12}}{4} \right) N^2 \left(\mathbf{M}_1^2 + \mathbf{M}_2^2 \right)^2 \\ & - \left(-\frac{4\lambda_{11} + 8\lambda_{12}}{4} \right) N^2 \left(\mathbf{M}_1^2 - \mathbf{M}_2^2 \right)^2 \end{aligned} \tag{2.31}$$

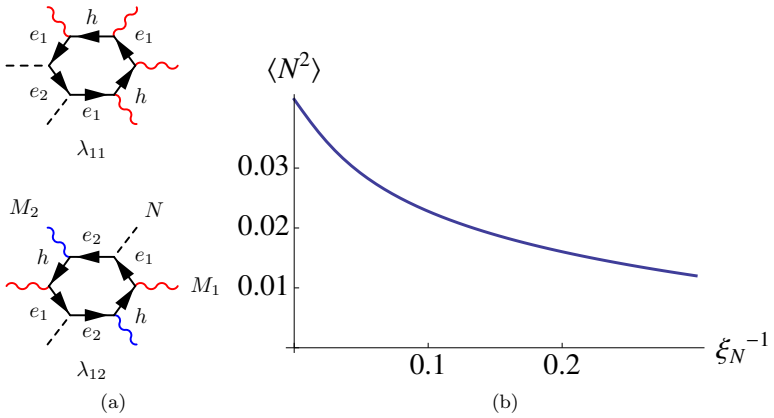

Figure 2.9: (a) Feynman diagrams λ_{ij} associated with the coupling between the Néel collective field $\mathbf{N}$ (dashed lines) and the magnetic order parameters $\mathbf{M}_1$ and $\mathbf{M}_2$ (wavy lines). The solid (black) lines are the Green's functions of the corresponding bands. (b) Behavior of the Gaussian Néel fluctuations $\langle N^2 \rangle$ as function of the inverse Néel correlation length ξ_N^{-1}. The Néel critical point is at $\xi_N^{-1} = 0$. From Ref. [35].

with the coefficients:

$$\alpha = 4 \int_k G_{h,k} G_{e_1,k}^2 G_{e_2,k}$$
$$\lambda_{ij} = \int_k G_{h,k}^2 G_{e_1,k} G_{e_2,k} G_{e_i,k} G_{e_j,k}$$

The coefficients λ_{ij} are represented diagrammatically in Fig. 2.9(a).

Near perfect nesting, $\alpha > 0$, reflecting the competition between the Néel and stripe states. To study the corrections to the quartic terms of the Ginzburg-Landau free energy Eq. 2.5, we consider Gaussian isotropic Néel fluctuations (i.e., $\langle N_i N_j \rangle = \frac{\langle N^2 \rangle}{3} \delta_{ij}$). We obtain $\tilde{u} = u + u_N \langle N^2 \rangle$, $\tilde{g} = g + g_N \langle N^2 \rangle$, and $\tilde{w} = w + w_N \langle N^2 \rangle$. Evaluating them near perfect nesting then gives $\frac{\tilde{u}}{u} \approx 1 - 0.13 \frac{\langle N^2 \rangle}{T_N^2}$ as well as:

$$\frac{\tilde{g}}{u} \approx 0.024 \left(\frac{\delta_m^2}{T_N^2} - \frac{4 \langle N^2 \rangle}{3 T_N^2} \right) \; ; \; \frac{\tilde{w}}{u} \approx -0.016 \frac{\langle N^2 \rangle}{T_N^2} \tag{2.32}$$

where T_N is the bare magnetic transition temperature. Thus, when Néel fluctuations are strong enough compared to the energy scale of the ellipticity of the electron pockets, $\langle N^2 \rangle > \delta_m^2/2$, the leading instability of the system is towards the CSDW state ($0 < \tilde{g} < -\tilde{w}$), which preserves the tetragonal symmetry of the system and induces a

simultaneous checkerboard charge order. Notice that, in the Gaussian approximation, $\langle N^2 \rangle \propto \int_{\mathbf{q}} \chi_N(\mathbf{q})$ does not diverge at the Néel critical point (see Fig. 2.9(b)), so the CSDW order is not guaranteed to appear.

In summary, we have shown that the CSDW order can be realized in the Mn-doped $BaFe_2As_2$ as a result of the interplay between itinerant magnetism promoted by the nesting features of the Fermi surface and Néel-type fluctuations promoted by local moments.

2.4 Experimental manifestations of C_4 magnetism

In previous sections, we showed that tetragonal magnetic orders do not naturally emerge from the localized J_1-J_2 Heisenberg model. On the other hand, the itinerant model gives a good account of the present experimental results. Therefore, establishing the existence of C_4 magnetic orders is crucial for establishing the proper theoretical framework to study magnetism and superconductivity.

Past experimental works relied on the presence/absence of lattice tetragonal to orthorhombic distortion to identify the magnetic phase. This is an indirect probe dependent on magnetoelastic coupling, i.e., the coupling between electronic and lattice degrees of freedom. Different magnetic orders give different Fermi surface reconstructions, as well as different low-energy spin wave excitations. Below I elaborate on how these two properties can be used as direct probes of various magnetic phases. This section is written based on our results obtained in Ref. [35, 36].

2.4.1 Fermi surface reconstruction

This section is written based on my paper Ref. [35].

An immediate difference between the C_2 magnetic order and the C_4 magnetic orders is the number of Fe atoms per magnetic unit cell. As shown in Fig. 2.3, the magnetic unit cell for the stripe orders contains two Fe atoms, whereas it is 4 for the CSDW and SVC orders. This leads to different Brillouin zone foldings, and different features of the reconstructed Fermi surfaces.

To study how the Fermi surface reconstruction can be different between C_2 and C_4 magnetic orders, we start with the five-orbital tight-binding model of Ref. [49], with the

Hamiltonian

$$H_0 = \sum_{mn}\sum_{\boldsymbol{k}\sigma} c^{\dagger}_{m,\mathbf{k}\sigma}\left(t_{mn} + \epsilon_m\delta_{mn} - \mu\delta_{mn}\right) c_{n,\mathbf{k}\sigma} \tag{2.33}$$

where σ is the spin index, and $m, n = 1...5$ label the five d-orbitals of the Fe atom. t_{mn}, ϵ_m are orbital hopping parameters and orbital onsite energies chosen to give the correct band structure according to the DFT calculations. The chemical potential is $\mu = 0$ for the undoped compound, corresponding to an occupation number of $n = 6$.

The presence of non-zero magnetic order parameters $\mathbf{M}_1$ and $\mathbf{M}_2$ gives rise to the term:

$$\begin{aligned} H_{\text{mag}} = &\sum_{i}\sum_{m}\sum_{\mathbf{k}\alpha\beta} c^{\dagger}_{m,\mathbf{k}\alpha}\left(\mathbf{M}_i\cdot\boldsymbol{\sigma}_{\alpha\beta}\right) c_{m,\mathbf{k}+\mathbf{Q}_i,\beta} + \\ &\kappa\sum_{m}\sum_{\mathbf{k}\alpha} c^{\dagger}_{m,\mathbf{k}\alpha}\left(\mathbf{M}_1\cdot\mathbf{M}_2\right) c_{m,\mathbf{k}+\mathbf{Q}_1+\mathbf{Q}_2,\alpha} + h.c. \end{aligned} \tag{2.34}$$

where we considered only intra-orbital magnetic order parameters [59], assumed for simplicity to be of equal amplitude. κ is a coupling constant that determines the amplitude of the higher-order harmonic generated when both $\mathbf{M}_1$ and $\mathbf{M}_2$ are non-zero. In our calculations, we found that the reconstructed Fermi surface does not depend strongly on the choice of κ.

The reconstructed Fermi surface for the stripe and CSDW orders can be obtained by diagonalizing the full Hamiltonian $H = H_0 + H_{\text{mag}}$ adjusting the chemical potential μ under the constraint of fixed occupation number $n = 6$. To diagonalize the Hamiltonian, we introduce the spinors:

$$\psi^{\dagger}_{m,\mathbf{k}\sigma} = \begin{pmatrix} c^{\dagger}_{m,\mathbf{k}\sigma} & c^{\dagger}_{m,\mathbf{k}+\mathbf{Q}_1\sigma} & c^{\dagger}_{m,\mathbf{k}+\mathbf{Q}_2\sigma} & c^{\dagger}_{m,\mathbf{k}+\mathbf{Q}_1+\mathbf{Q}_2\sigma} \end{pmatrix}$$

The order parameters couple different elements in Nambu space: $\mathbf{M}_i$ couples $c^{\dagger}_{m,\mathbf{k}\sigma}$ to $c_{m,\mathbf{k}+\mathbf{Q}_i\sigma'}$ and $c^{\dagger}_{m,\mathbf{k}+\mathbf{Q}_i\sigma}$ to $c_{m,\mathbf{k}+\mathbf{Q}_1+\mathbf{Q}_2\sigma'}$, while $\mathbf{M}_1\cdot\mathbf{M}_2$ couples $c^{\dagger}_{m,\mathbf{k}+\mathbf{Q}_1\sigma}$ to $c_{m,\mathbf{k}+\mathbf{Q}_2\sigma'}$ and $c^{\dagger}_{m,\mathbf{k}\sigma}$ to $c_{m,\mathbf{k}+\mathbf{Q}_1+\mathbf{Q}_2\sigma'}$. For the $(\pi, 0)$ stripe order, $\mathbf{M}_2 = 0$ and $\mathbf{M}_1 = M\hat{\mathbf{x}}$, and the magnetic unit cell is given by $-\pi/2 \le k_x \le \pi/2$ and $-\pi \le k_y \le \pi$. For the CSDW magnetic order, $\mathbf{M}_1 = \mathbf{M}_2 = \frac{M}{\sqrt{2}}\hat{x}$, where the factor of $\sqrt{2}$ is to keep the total order parameter $\sqrt{M_1^2 + M_2^2}$ the same as in the striped case. The magnetic unit cell is given in this case by $-\pi/2 \le k_x, k_y \le \pi/2$. The SVC order gives rise to similar Fermi surface reconstructions compared to the CSDW order, and is not discussed here.

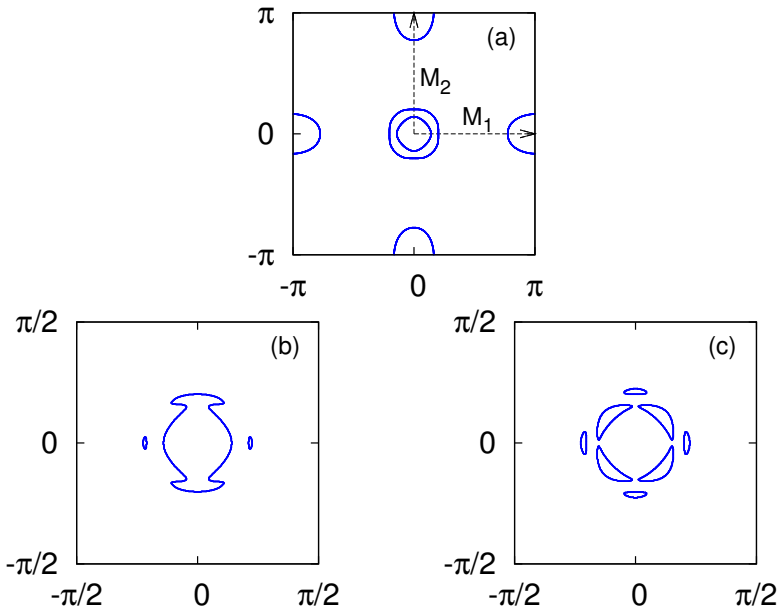

Figure 2.10: Reconstructed Fermi surfaces near the center of the Brillouin zone in the presence of $\mathbf{Q}_1 = (\pi, 0)$ stripe magnetic order (b) and CSDW magnetic order (c). The Fermi surface in the paramagnetic state is shown in (a), with the tight-binding parameters of Ref. [49]. From Ref. [35].

In Fig. 2.10, we present the reconstructed Fermi surface around the center of the magnetic Brillouin zone for both magnetic ground states. In the paramagnetic phase, the Fermi surface consists of two concentric hole pockets at the center of the Brillouin zone and two elliptical pockets centered at the momenta $\mathbf{Q}_1 = (\pi, 0)$ and $\mathbf{Q}_2 = (0, \pi)$. In the striped state, we find that for reasonable values of the magnetic order parameter ($M \approx 60$ meV), one of the hole pockets remains unhybridized while the other hole pocket hybridizes with the folded electron pocket, giving rise to "Dirac cones" – the small reconstructed pockets along the stripe modulation direction. This is in general agreement with previous theoretical and experimental results [60, 61, 59]. On the other hand, for the CSDW state, each of the two hole pockets hybridize with one of the two electron pockets. As a result, there remains only small reconstructed pockets [62]. Unlike the small pockets that appear in the stripe state case, four of these pockets appear along the $\mathbf{Q}_1 + \mathbf{Q}_2 = (\pi, \pi)$ direction. We found that a non-zero CDW order parameter $\rho_{\mathbf{Q}_N}$ does not lead to qualitative differences in the reconstructed Fermi surface.

2.4.2 Spin wave

This section is written based on my paper Ref. [35].

A main difference between the SVC and the stripe phase is the absence of collinear spins (see Fig. 2.3). As has been shown in Ref. [63], the number of Goldstone modes (acousticspin waves) for collinear and non-collinear magnetic phases are different, due to different number of broken rotational symmetry generators in the spin space. In this section, we study in details the spin-wave spectrum of the SVC magnetic phase, and compare it to the stripe phase.

As we are interested in the low-energy behavior, there are two alternative approaches to compute the spin-wave spectrum: the first is by evaluating self-consistently the poles of the spin-spin correlation function deep inside the magnetically ordered state within the itinerant approach described in the previous section [64]. The second alternative is to build a phenomenological localized-spin model that gives the same ground states as the itinerant model, and then use Holstein-Primakoff (HP) bosons to compute the spin-wave dispersion.[65, 66]. [4] Given the simplicity of the latter, we here consider a Heisenberg model on a two-dimensional square lattice, with nearest-neighbor and next-nearest neighbor interactions:

$$H = J_1 \sum_{\langle i,j \rangle} \mathbf{S}_i \cdot \mathbf{S}_j + J_2 \sum_{\langle\langle i,j \rangle\rangle} \mathbf{S}_i \cdot \mathbf{S}_j - \frac{K}{S^2} \sum_{\langle i,j \rangle} (\mathbf{S}_i \cdot \mathbf{S}_j)^2 \tag{2.35}$$

where $\langle ... \rangle$ and $\langle\langle ... \rangle\rangle$ denote nearest-neighbors and next-nearest neighbors, and $J_1 > 0$, $J_2 > J_1/2$ are the respective antiferromagnetic exchange interactions. The biquadratic term K selects between the stripe phase ($K > 0$) and the SVC phase ($K < 0$) in the classical regime. We emphasize that this is a phenomenological model constructed to describe the ground states obtained in Section II. Indeed, as discussed previously, if it was the classical J_1-J_2 model, K would be restricted to small positive values only [48]. Instead, here K should be understood as a phenomenological parameter, analogous to the parameter g calculated in Eq. (2.19). In fact, a Ginzburg-Landau expansion of this toy Heisenberg model would result in a free energy equivalent to that of Eq. (2.19), evidencing the fact that both models share the same low-energy properties [68].

[4] To study spin-wave spectrum of the CSDW phase, we need to work with the itinerant model rather than the J_1-J_2 spin Heisenberg model. This is not done here. For a more thorough investigation of magnetic excitations of the CSDW order, refer to Ref. [67].

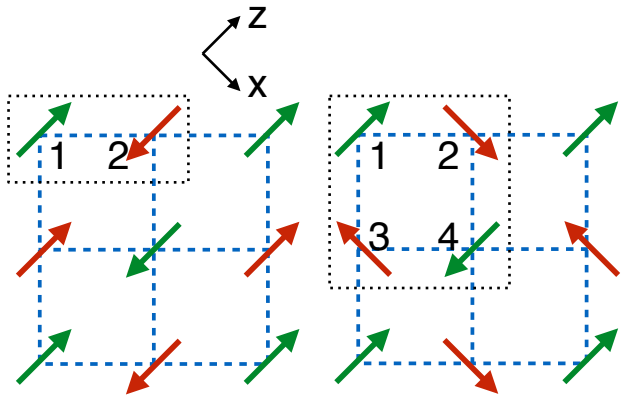

Figure 2.11: Magnetic unit cell for the stripe magnetic order with wavevector $\mathbf{Q}_1$, and SVC order with wavevectors $\mathbf{Q}_1$ and $\mathbf{Q}_2$. In the text for introducing Holstein-Primakov bosons, we used a local spin coordinate system, where the z axis is parallel to the local spin alignment. The global spin coordinate system is chosen to be that for site 1.

Therefore, the use of this localized-spin model should be understood simply as a tool to evaluate the spin-wave spectrum, and not an implication that local moments are necessarily present in the system. Incidentally, we note that other Heisenberg models with ring exchange interactions can also display the SVC order [69].

We emphasize that a strict two-dimensional model does not have long-range Heisenberg magnetic order, according to Mermin-Wagner theorem. As a result, we assume here that the system is formed by weakly-coupled layers. Such a small inter-layer coupling can nevertheless be neglected in what regards the main properties of the spin-wave dispersions. To obtain the spin-wave spectrum of the Hamiltonian (2.35), we follow Refs. [70, 71] and introduce locally Holstein-Primakoff (HP) bosons for each of the r spins in a single magnetic unit cell:

$$\begin{aligned}
\mathbf{S}_z^{(r)} &= S - a^{(r)\dagger} a^{(r)} \\
\mathbf{S}_+^{(r)} &= \sqrt{2S - a^{(r)\dagger} a^{(r)}}\; a^{(r)} \\
\mathbf{S}_-^{(r)} &= a^{(r)\dagger} \sqrt{2S - a^{(r)\dagger} a^{(r)}}
\end{aligned} \tag{2.36}$$

Here a annihilates a HP boson. Note that the spin coordinate system is defined locally, such that the local spin is always parallel to the local $+\hat{\mathbf{z}}$ axis, see Fig. 2.11. For convenience, the two-dimensional lattice plane xy is chosen to be the xz spin-plane.

Since different types of spins within a magnetic unit cell have their own degree of freedom, the number of HP bosons (labeled by r) is equal to the number of spins within a magnetic unit cell. Thus, the stripe state has $r = 1, 2$ whereas the SVC state has $r = 1, 2, 3, 4$. The Fourier transform of the HP bosons is defined as

$$a_{\mathbf{k}}^{(r)} = \sum_{i \in r} a_i^{(r)} e^{-i\mathbf{k}\cdot\mathbf{x}_i^{(r)}} \tag{2.37}$$

where i labels different magnetic unit cells, and $\mathbf{x}_i^{(r)}$ is the position of the r-th spin in the i-th magnetic unit cell. For convenience, we define:

$$\Psi_{\mathbf{k}}^{\dagger} \equiv \left(a_{\mathbf{k}}^{(1)\dagger}, a_{-\mathbf{k}}^{(1)}, a_{\mathbf{k}}^{(2)\dagger}, a_{-\mathbf{k}}^{(2)}, ... \right) \tag{2.38}$$

Because we are interested in the classical limit, we perform a large S expansion and keep only terms that are quadratic in the bosonic operators. In this case, the Heisenberg Hamiltonian can be re-expressed as:

$$H = H_0 + \frac{1}{2} \sum_{\mathbf{k}} \Psi_{\mathbf{k}}^{\dagger} \hat{\mathcal{H}}_{\mathbf{k}} \Psi_{\mathbf{k}} \tag{2.39}$$

where H_0 is the classical ground state energy for a given spin configuration. The spin-wave modes can be obtained by a generalized Bogoliubov transformation, $\Psi_{\mathbf{k}} = \hat{\mathcal{U}}_{\mathbf{k}} \Phi_{\mathbf{k}}$. To ensure that the transformed operators satisfy the correct bosonic commutation relations, it is convenient to introduce the Bogoliubov metric:

$$\hat{\eta} = \mathrm{diag}(1, -1, 1, -1, ...) \tag{2.40}$$

Then, the generalized Bogoliubov transformation satisfies:

$$\begin{aligned} \hat{\mathcal{U}}_{\mathbf{k}}^{\dagger} \hat{\eta} \hat{\mathcal{U}}_{\mathbf{k}} &= \hat{\eta} \\ \hat{\mathcal{U}}_{\mathbf{k}}^{-1} \left(\hat{\eta} \hat{\mathcal{H}}_{\mathbf{k}} \right) \hat{\mathcal{U}}_{\mathbf{k}} &= \left(\hat{\eta} \hat{\mathcal{H}}_{\mathbf{k}} \right)^{\mathrm{diag}} \end{aligned} \tag{2.41}$$

The spin-wave modes are therefore the eigenvalues of $\hat{\eta} \hat{\mathcal{H}}_{\mathbf{k}}$.

Spin wave excitations in the stripe magnetic phase

As discussed above, the stripe phase is the ground state of the model (Eq. 2.35) for $K > 0$. The spin-wave dispersion of the stripe phase was obtained previously in Refs. [72,

73, 74] and here we rederive the results to compare them later with the SVC case. For concreteness, we first consider the stripe phase with ordering vector $\mathbf{Q}_1 = (\pi, 0)$. As shown in Fig. 2.11, there are two spins per magnetic unit cell, whose HP operators we denote by $a_{\mathbf{k}}^{(1)}$ and $a_{\mathbf{k}}^{(2)}$. Note that, with respect to the spin coordinate system defined on site 1, the spin on site 2 is rotated by 180°, yielding:

$$\mathbf{S}^{(2)} = \left(-S_x^{(2)}, S_y^{(2)}, -S_z^{(2)}\right)_{(1)} \tag{2.42}$$

Using the Holstein-Primakoff transformation defined in Eq. 2.38, we find that the large-S Hamiltonian is given by:

$$\hat{\mathcal{H}}_{\mathbf{k}} = \begin{pmatrix} \epsilon_{\mathbf{k}} & 0 & 0 & \Delta_{\mathbf{k}} \\ 0 & \epsilon_{\mathbf{k}} & \Delta_{\mathbf{k}} & 0 \\ 0 & \Delta_{\mathbf{k}} & \epsilon_{\mathbf{k}} & 0 \\ \Delta_{\mathbf{k}} & 0 & 0 & \epsilon_{\mathbf{k}} \end{pmatrix} \tag{2.43}$$

with:

$$\begin{aligned} \epsilon_{\mathbf{k}} &= 2S\left[(J_1 - 2K)\cos k_y + 2J_2 + 4K\right] \\ \Delta_{\mathbf{k}} &= -2S\left(J_1 + 2K + 2J_2 \cos k_y\right)\cos k_x \end{aligned} \tag{2.44}$$

The Hamiltonian is diagonalized via the Bogoliubov transformation

$$\hat{\mathcal{U}}_{\mathbf{k}} = \begin{pmatrix} u_{\mathbf{k}} & 0 & 0 & v_{\mathbf{k}} \\ 0 & u_{\mathbf{k}} & v_{\mathbf{k}} & 0 \\ 0 & v_{\mathbf{k}} & u_{\mathbf{k}} & 0 \\ v_{\mathbf{k}} & 0 & 0 & u_{\mathbf{k}} \end{pmatrix} \tag{2.45}$$

with:

$$u_{\mathbf{k}}^2 = \frac{1}{2}\left(1 + \frac{\epsilon_{\mathbf{k}}}{\omega_{\mathbf{k}}}\right);\ v_{\mathbf{k}}^2 = \frac{1}{2}\left(-1 + \frac{\epsilon_{\mathbf{k}}}{\omega_{\mathbf{k}}}\right);\ u_{\mathbf{k}} v_{\mathbf{k}} = -\frac{1}{2}\frac{\Delta_{\mathbf{k}}}{\omega_{\mathbf{k}}} \tag{2.46}$$

yielding the doubly-degenerate eigenmode (i.e. spin-wave mode) of the bosonic system:

$$\omega_{\mathbf{k}} = \sqrt{\epsilon_{\mathbf{k}}^2 - \Delta_{\mathbf{k}}^2} \tag{2.47}$$

The fact that there are two degenerate spin-wave modes for the stripe state is a consequence of the fact that $\omega_{\mathbf{k}+\mathbf{Q}_1} = \omega_{\mathbf{k}}$ and also of the collinear configuration of the

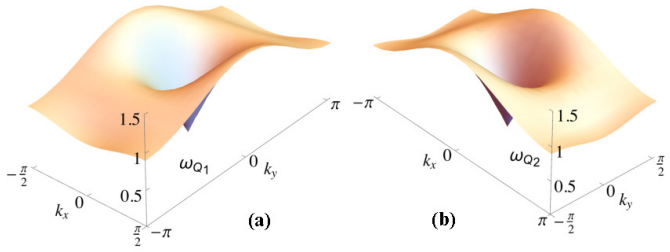

Figure 2.12: Spin-wave dispersions for the stripe phase with ordering vector $\mathbf{Q}_1 = (\pi, 0)$ (a) and $\mathbf{Q}_2 = (0, \pi)$ (b). Both are doubly degenerate modes. The energies are in units of $4J_2S$ and the parameters used are $J_1 = 0.8J_2$ and $K = 0.1J_2$. From Ref. [36].

spins. The spin-wave dispersion of the stripe phase with ordering vector $\mathbf{Q}_2 = (0, \pi)$ can be calculated in the same way, yielding $\omega_{\mathbf{Q}_2}(k_x, k_y) = \omega_{\mathbf{Q}_1}(k_y, -k_x)$, as expected. In Fig. 2.12, we show the dispersion of the spin waves (Eq. 2.47) for the two types of stripe orders in their respective *magnetic* Brillouin zones. The results obtained here are in agreement with those obtained previously elsewhere [74].

Spin wave excitations in the SVC phase

The SVC phase becomes the ground state of Eq. 2.35 for $K < 0$. As shown in Fig. 2.11, there are four spins per magnetic unit cell, giving rise to the HP operators $a_{\mathbf{k}}^{(1)}$, $a_{\mathbf{k}}^{(2)}$, $a_{\mathbf{k}}^{(3)}$, and $a_{\mathbf{k}}^{(4)}$. Because the spins on sites 2, 3, 4 correspond respectively to rotations of 90°, 180°, and 270° relative to the spin on site 1, we define the local spin coordinate systems:

$$\begin{aligned}
\mathbf{S}^{(2)} &= (S_z^{(2)}, S_y^{(2)}, -S_x^{(2)})_{(1)} \\
\mathbf{S}^{(3)} &= (-S_z^{(3)}, S_y^{(3)}, S_x^{(3)})_{(1)} \\
\mathbf{S}^{(4)} &= (-S_x^{(4)}, S_y^{(4)}, -S_z^{(4)})_{(1)}
\end{aligned} \tag{2.48}$$

Introducing $\Psi_{\mathbf{k}}^{\dagger}$ as defined in Eq. 2.38 and substituting in the Hamiltonian, we obtain in the large-S limit:

$$\hat{\mathcal{H}}_{\mathbf{k}} = \begin{pmatrix} \hat{A}_{\mathbf{k}} & \hat{B}_{\mathbf{k}} & \hat{C}_{\mathbf{k}} & \hat{D}_{\mathbf{k}} \\ \hat{B}_{\mathbf{k}} & \hat{A}_{\mathbf{k}} & \hat{D}_{\mathbf{k}} & \hat{C}_{\mathbf{k}} \\ \hat{C}_{\mathbf{k}} & \hat{D}_{\mathbf{k}} & \hat{A}_{\mathbf{k}} & \hat{B}_{\mathbf{k}} \\ \hat{D}_{\mathbf{k}} & \hat{C}_{\mathbf{k}} & \hat{B}_{\mathbf{k}} & \hat{A}_{\mathbf{k}} \end{pmatrix} \tag{2.49}$$

where we defined four 2×2 matrices, $\hat{A}_{\mathbf{k}}$, $\hat{B}_{\mathbf{k}}$, $\hat{C}_{\mathbf{k}}$, and $\hat{D}_{\mathbf{k}}$ of the form:

$$\hat{O}_{\mathbf{k}} = \begin{pmatrix} O_{1,\mathbf{k}} & O_{2,\mathbf{k}} \\ O_{2,\mathbf{k}} & O_{1,\mathbf{k}} \end{pmatrix} \tag{2.50}$$

with the matrix elements:

$$\begin{aligned} A_{1,\mathbf{k}} &= 4S\left(J_2 - K\right), \; A_{2,\mathbf{k}} = -4SK \\ B_{1,\mathbf{k}} &= S\left(J_1 + 2K\right)\cos k_x, \; B_{2,\mathbf{k}} = -S\left(J_1 - 2K\right)\cos k_x \\ C_{1,\mathbf{k}} &= S\left(J_1 + 2K\right)\cos k_y, \; C_{2,\mathbf{k}} = -S\left(J_1 - 2K\right)\cos k_y \\ D_{1,\mathbf{k}} &= 0, \; D_{2,\mathbf{k}} = -4SJ_2 \cos k_x \cos k_y \end{aligned} \tag{2.51}$$

The generalized Bogoliubov transformation is given by:

$$\hat{\mathcal{U}}_{\mathbf{k}} = \begin{pmatrix} \hat{X}_{\mathbf{k}} & \hat{Y}_{\mathbf{k}} & \hat{Z}_{\mathbf{k}} & \hat{W}_{\mathbf{k}} \\ \hat{X}_{\mathbf{k}} & -\hat{Y}_{\mathbf{k}} & \hat{Z}_{\mathbf{k}} & -\hat{W}_{\mathbf{k}} \\ \hat{X}_{\mathbf{k}} & \hat{Y}_{\mathbf{k}} & -\hat{Z}_{\mathbf{k}} & -\hat{W}_{\mathbf{k}} \\ \hat{X}_{\mathbf{k}} & -\hat{Y}_{\mathbf{k}} & -\hat{Z}_{\mathbf{k}} & \hat{W}_{\mathbf{k}} \end{pmatrix} \tag{2.52}$$

where the four 2×2 matrices, $\hat{X}_{\mathbf{k}}$, $\hat{Y}_{\mathbf{k}}$, $\hat{Z}_{\mathbf{k}}$, and $\hat{W}_{\mathbf{k}}$ are also of the form (2.50). For $\hat{X}_{\mathbf{k}}$, the matrix elements are given by:

$$\begin{aligned} X_{1,\mathbf{k}}^2 &= \frac{1}{8}\left(1 + \frac{\epsilon_{\mathbf{k}}}{\omega_{\mathbf{k}}}\right) \\ X_{2,\mathbf{k}}^2 &= \frac{1}{8}\left(-1 + \frac{\epsilon_{\mathbf{k}}}{\omega_{\mathbf{k}}}\right) \\ X_{1,\mathbf{k}} X_{2,\mathbf{k}} &= -\frac{1}{8}\frac{\Delta_{\mathbf{k}}}{\omega_{\mathbf{k}}} \end{aligned} \tag{2.53}$$

with:

$$\begin{aligned} \epsilon_{\mathbf{k}} &= A_{1,\mathbf{k}} + B_{1,\mathbf{k}} + C_{1,\mathbf{k}} + D_{1,\mathbf{k}} \\ \Delta_{\mathbf{k}} &= A_{2,\mathbf{k}} + B_{2,\mathbf{k}} + C_{2,\mathbf{k}} + D_{2,\mathbf{k}} \end{aligned} \tag{2.54}$$

and the spin-wave dispersions:

$$\omega_{\mathbf{k}} = \sqrt{\epsilon_{\mathbf{k}}^2 - \Delta_{\mathbf{k}}^2} \tag{2.55}$$

For the other matrix elements, we find:

$$\begin{aligned} Y_{i,\mathbf{k}} &= X_{i,\mathbf{k}+\mathbf{Q}_1} \\ Z_{i,\mathbf{k}} &= X_{i,\mathbf{k}+\mathbf{Q}_2} \\ W_{i,\mathbf{k}} &= X_{i,\mathbf{k}+\mathbf{Q}_1+\mathbf{Q}_2} \end{aligned} \tag{2.56}$$

Therefore, there are four non-degenerate spin-wave dispersions of the bosonic system:

$$\omega_{1\mathbf{k}} = \omega_{\mathbf{k}};\ \omega_{2\mathbf{k}} = \omega_{\mathbf{k}+\mathbf{Q}_1};\ \omega_{3\mathbf{k}} = \omega_{\mathbf{k}+\mathbf{Q}_2};\ \omega_{4\mathbf{k}} = \omega_{\mathbf{k}+\mathbf{Q}_1+\mathbf{Q}_2} \tag{2.57}$$

with $\omega_{\mathbf{k}}$ given in Eq. 2.55. These four spin-wave dispersions are shifted with respect to each other by the ordering vectors of the SVC phase, corresponding to in-phase or out-of-phase combinations of the four HP bosons. All of them are shown in Fig. 2.13 in the *magnetic* unit cell of the SVC phase. We note that while ω_1, ω_2, and ω_3 display gapless modes, corresponding to three Goldstone modes, the ω_4 spin-wave dispersion is gapped. The fact that there are three Goldstone modes is a consequence of the non-collinear magnetic configuration of the SVC phase, which breaks completely all the spin-rotational symmetries of the system.

Dynamic structure factors of the stripe and SVC phases

Having established the nature of the spin-wave modes in the stripe and SVC phases, we now proceed to compute the spin-spin correlation function $\mathcal{S}_{\mu\nu}$ in the non-magnetic unit cell, which can be measured by neutron scattering. Follwing [71, 70], we have:

$$\mathcal{S}_{\mu\nu}\left(\mathbf{k},\omega\right) = \int_{-\infty}^{\infty} \frac{\mathrm{d}t}{2\pi}\ \mathrm{e}^{-i\omega t}\langle S^{\mu}_{\mathbf{k}}(0) S^{\nu}_{-\mathbf{k}}(t)\rangle \tag{2.58}$$

where $\mu\nu = x, y, z$ refer to the spin components and $\mathbf{S}_{\mathbf{k}} \equiv \sum_r \mathbf{S}_{r,\mathbf{k}}$ is the sum over all the r spins in the magnetic unit cell. Here, the spin coordinate system is defined globally with respect to the neutron polarization, in contrast to the local coordinate system introduced in the previous subsection. For concreteness, hereafter we assume the incoming neutron to be polarized parallel to the spin on site 1, i.e. parallel to the $\hat{\mathbf{z}}$ axis. Computation of Eq. 2.58 is straightforward with the aid of the HP bosons and the Bogoliubov transformation defined in the previous subsection. Denoting by $\tilde{a}^{(r)}_{\mathbf{k}}$ the

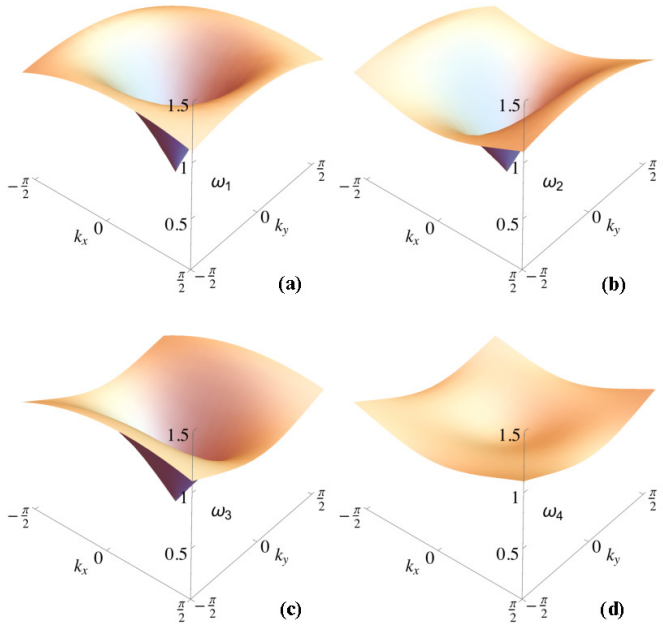

Figure 2.13: The spin-wave dispersions of the SVC order in the magnetic Brillouin zone. The four dispersions are linked by a shift of the momentum coordinate system by the SVC ordering vectors. Here, the energies are in units of $4J_2S$ and the parameters are $J_1 = 0.8J_2$ and $K = -0.1J_2$. From Ref. [36].

Bogoliubov-transformed bosonic operators, the only non-zero terms, at $T = 0$, are those of the form:

$$\int_{-\infty}^{\infty} \frac{\mathrm{d}t}{2\pi}\, \mathrm{e}^{-i\omega t} \left\langle \tilde{a}_{\mathbf{k}}^{(r)}(0)\, \tilde{a}_{\mathbf{k}}^{\dagger(r)}(t) \right\rangle = \delta\left(\omega - \omega_{r,\mathbf{k}}\right) \tag{2.59}$$

We first consider the stripe phase with the two possible ordering vectors $\mathbf{Q}_1 = (\pi, 0)$ and $\mathbf{Q}_2 = (0, \pi)$. We find that only the transverse components $\mathcal{S}_{xx} = \mathcal{S}_{yy}$ are non-zero, i.e. the longitudinal component S_{zz} and the off-diagonal components $\mathcal{S}_{i\neq j}$ do not acquire spin-wave contributions. We obtain:

$$\mathcal{S}_{xx}^{\mathbf{Q}_i}(\mathbf{k}, \omega) = 2S\left(u_{\mathbf{k}} - v_{\mathbf{k}}\right)^2 \delta\left(\omega - \omega_{\mathbf{k}}^{\mathbf{Q}_i}\right) \tag{2.60}$$

where $u_{\mathbf{k}}, v_{\mathbf{k}}$ are given by Eq. (2.46) and $\omega_{(k_x,k_y)}^{\mathbf{Q}_2} = \omega_{(-k_y,k_x)}^{\mathbf{Q}_1}$, with $\omega_{\mathbf{k}}^{\mathbf{Q}_1}$ given by Eq. (2.47). The total spin-spin correlation function, $\mathcal{S} = \sum_i \mathcal{S}_{ii}$ is then simply $\mathcal{S}(\mathbf{k}, \omega) = 2\mathcal{S}_{xx}(\mathbf{k}, \omega)$. In Fig. 2.14, we plot $\mathcal{S}(\mathbf{k}, \omega)$ for both the $\mathbf{Q}_1$ and $\mathbf{Q}_2$ stripe

phases separately, as well as for a system containing equal domains of $\mathbf{Q}_1$ and $\mathbf{Q}_2$:

$$\mathcal{S}_{\text{domain}}(\mathbf{k},\omega) = \frac{1}{2}\mathcal{S}^{\mathbf{Q}_1}(\mathbf{k},\omega) + \frac{1}{2}\mathcal{S}^{\mathbf{Q}_2}(\mathbf{k},\omega) \tag{2.61}$$

The latter is the case relevant for the real systems, since twin domains are always formed in the iron pnictides. In all the plots, the delta function is replaced by a Lorentzian with width $\gamma = 0.05$ in units of $2J_2S$. From the figure, we see that the system with twin domains display anisotropic spin-wave branches emerging from the ordering vectors $\mathbf{Q}_1 = (\pi, 0)$ and $\mathbf{Q}_2 = (0, \pi)$, as expected. In all cases, the structure factor vanishes at center of the Brillouin zone, but diverges at the ordering vectors $\mathbf{Q}_i$. Therefore, expanding the spin-wave dispersion around the ordering vector $\mathbf{Q}_i$ yields (θ denote the polar angle between $\mathbf{k}$ and $\hat{\mathbf{k}}_x$):

$$\omega_{\mathbf{k}+\mathbf{Q}_i} \approx 4S|\mathbf{k}|\sqrt{\left(J_2 + K + \frac{J_1}{2}\right)\left(J_2 + K \pm \frac{J_1}{2}\cos 2\theta\right)} \tag{2.62}$$

which is anisotropic along the k_x and k_y axis, as expected. In the previous expression, the upper (lower) sign refers to $\mathbf{Q}_1$ ($\mathbf{Q}_2$).

For the SVC phase, we find that all diagonal components $\mathcal{S}_{ii}$ acquire spin-wave contributions. This is expected since the magnetic configuration is non-collinear (see Fig. 2.3), implying that all directions are "transverse" with respect to the sublattice $1, 3$ and/or the sublattice $2, 4$. In particular, we find:

$$\begin{aligned}
\mathcal{S}_{xx}(\mathbf{k},\omega) = \mathcal{S}_{zz}(\mathbf{k},\omega) &= 4S\left(Y_{1,\mathbf{k}} + Y_{2,\mathbf{k}}\right)^2 \delta\left(\omega - \omega_{2,\mathbf{k}}\right) \\
&\quad + 4S\left(Z_{1,\mathbf{k}} + Z_{2,\mathbf{k}}\right)^2 \delta\left(\omega - \omega_{3,\mathbf{k}}\right) \\
\mathcal{S}_{yy}(\mathbf{k},\omega) &= 16S\left(X_{1,\mathbf{k}} - X_{2,\mathbf{k}}\right)^2 \delta\left(\omega - \omega_{1,\mathbf{k}}\right)
\end{aligned} \tag{2.63}$$

with the Bogoliubov transformation parameters and spin-wave modes defined in Eqs. 2.53 and 2.57. In Fig. 2.15, we plot these diagonal components as well as the total structure factor $\mathcal{S} = \sum_i \mathcal{S}_{ii}$. In the latter, we observe two spin-wave branches emerging from the ordering vectors $\mathbf{Q}_1 = (\pi, 0)$ and $\mathbf{Q}_2 = (0, \pi)$, in sharp contrast to the case of domains of stripes, where only one spin-wave branch emerges from each ordering vector (see Fig. 2.14). We note that, once again, the structure factor vanishes at the center of the Brillouin zone and diverges at the magnetic ordering vectors $\mathbf{Q}_1 = (\pi, 0)$ and

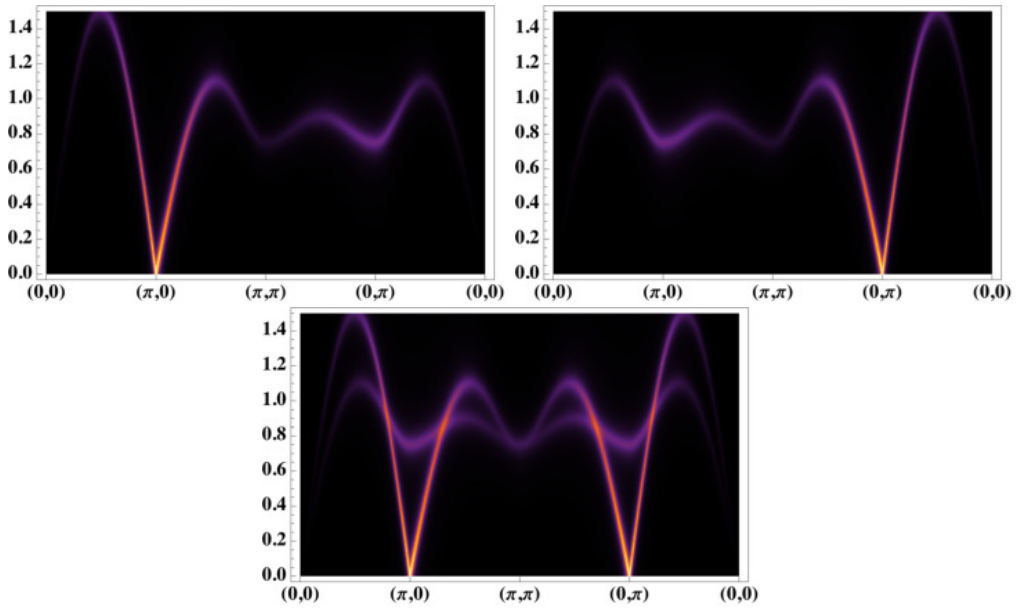

Figure 2.14: The total spin-spin structure factor $\mathcal{S} = \sum_i \mathcal{S}_{ii} = 2S_{xx}$ for the $\mathbf{Q}_1$ (top panel) and $\mathbf{Q}_2$ (mid panel) stripe phases. Bottom panel is the structure factor assuming equal domains of $\mathbf{Q}_1$ and $\mathbf{Q}_2$ stripes. The vertical axis is the energy measured in units of $4J_2S$, whereas the horizontal axis displays momentum cuts in the Fe-square-lattice Brillouin zone. The intensity is highest at the ordering vectors $\mathbf{Q}_1$ and $\mathbf{Q}_2$. The parameters used here are $J_1 = 0.8J_2$ and $K = 0.1J_2$. From Ref. [36].

$\mathbf{Q}_2 = (0, \pi)$. Expanding the dispersions near them, we find (recall that $K < 0$):

$$\begin{aligned}
\omega_{1,\mathbf{k}+\mathbf{Q}_1} &\approx 4S\,|\mathbf{k}|\sqrt{(J_2 - K)\left(J_2 + \frac{J_1}{2}\cos 2\theta\right)} \\
\omega_{2,\mathbf{k}+\mathbf{Q}_1} &\approx 4S\,|\mathbf{k}|\sqrt{(J_2 - K)\left(J_2 + \frac{J_1}{2}\right)} \\
\omega_{3,\mathbf{k}+\mathbf{Q}_1} &\approx 8S\sqrt{(2J_2 - J_1)\,(-K)}
\end{aligned} \tag{2.64}$$

as well as:

$$\begin{aligned}
\omega_{1,\mathbf{k}+\mathbf{Q}_2} &\approx 4S\left|\mathbf{k}\right|\sqrt{\left(J_2-K\right)\left(J_2-\frac{J_1}{2}\cos 2\theta\right)} \\
\omega_{2,\mathbf{k}+\mathbf{Q}_2} &\approx 8S\sqrt{\left(2J_2-J_1\right)\left(-K\right)} \\
\omega_{3,\mathbf{k}+\mathbf{Q}_2} &\approx 4S\left|\mathbf{k}\right|\sqrt{\left(J_2-K\right)\left(J_2+\frac{J_1}{2}\right)}
\end{aligned} \tag{2.65}$$

Therefore, we obtain two gapless spin-wave branches emerging from each ordering vector, as shown in Fig. 2.15, as well as one gapped spin-wave dispersion. As expected, tetragonal symmetry is preserved by these dispersions. Interestingly, along the direction parallel to the $\mathbf{Q}_i$ vector, the two spin-wave velocities are equal, whereas along the direction perpendicular to the $\mathbf{Q}_i$ vector, they are different. In the latter case, their ratio is given by:

$$\frac{\mathrm{c}_{1,\perp}}{\mathrm{c}_{2,\perp}}=\sqrt{\frac{2J_2+J_1}{2J_2-J_1}} \tag{2.66}$$

where the $\perp$ sign indicates that the spin-wave velocity is measured relative to the direction perpendicular to the ordering vector $\mathbf{Q}_i$. Interestingly, this ratio does not depend on the biquadratic coupling K. These qualitative features, in principle, allow one to experimentally distinguish, in an unambiguous way, whether the magnetic ground state is stripe or SVC. Note that, in the SVC phase, no spin-wave modes emerge from $\mathbf{Q}_1+\mathbf{Q}_2=(\pi,\pi)$.

Continuing the investigation of the SVC phase, we find that the spin-waves also contribute to the off-diagonal component:

$$\begin{aligned}
\mathcal{S}_{xz}\left(\mathbf{k},\omega\right) = {} & 4S\left(Y_{1,\mathbf{k}}+Y_{2,\mathbf{k}}\right)^2\delta\left(\omega-\omega_{2,\mathbf{k}}\right) \\
& -4S\left(Z_{1,\mathbf{k}}+Z_{2,\mathbf{k}}\right)^2\delta\left(\omega-\omega_{3,\mathbf{k}}\right)
\end{aligned} \tag{2.67}$$

providing another criterion to distinguish experimentally the SVC and stripe phases via polarized neutron scattering.

In principle, the structure factor tensor of the SVC phase can be brought in a diagonal form if the neutron is polarized along $\tilde{\mathbf{z}}=\left(\mathbf{x}+\mathbf{z}\right)/\sqrt{2}$, instead of parallel to the spin on site 1. In this new coordinate system, each of the three gapless spin-wave

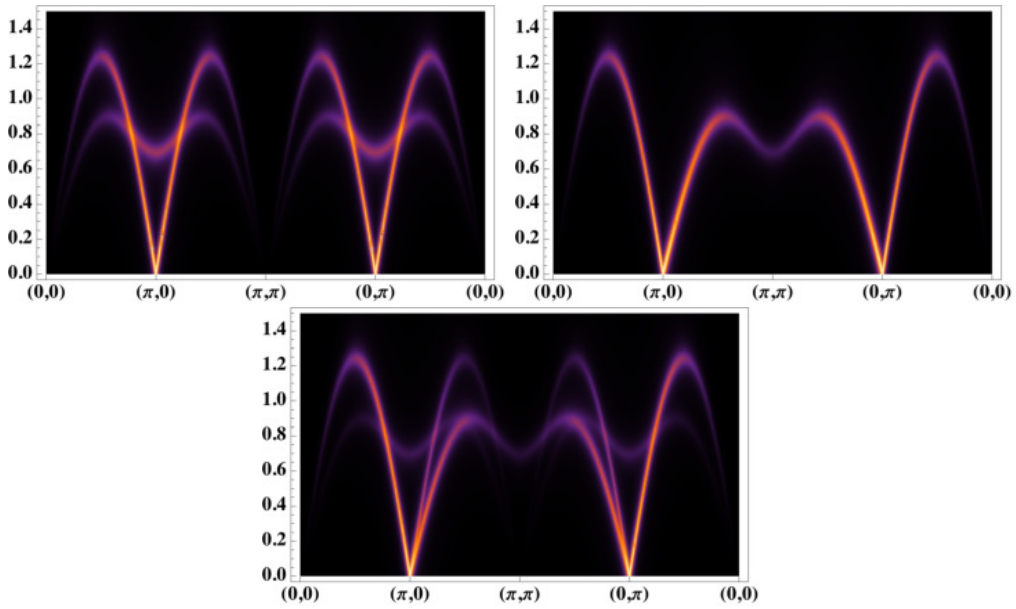

Figure 2.15: The structure factors $\mathcal{S}_{xx} = \mathcal{S}_{zz}$ (top panel), $\mathcal{S}_{yy}$ (mid panel) and $\mathcal{S} = \sum_i \mathcal{S}_{ii}$ (bottom panel) for the SVC phase. The vertical axis is the energy measured in units of $4J_2S$, whereas the horizontal axis displays momentum cuts in the Fe-square-lattice Brillouin zone. The parameters used here are $J_1 = 0.8J_2$ and $K = -0.1J_2$. Two gapless spin-wave branches emerge from the ordering vectors $\mathbf{Q}_1 = (\pi, 0)$ and $\mathbf{Q}_2 = (0, \pi)$, in sharp contrast to the case of domains of stripes shown in Fig. 2.14. From Ref. [36].

dispersions contribute only to one of the diagonal components, and we find:

$$\begin{aligned} \tilde{\mathcal{S}}_{zz}(\mathbf{k}, \omega) &= 8S\left(Y_{1,\mathbf{k}} + Y_{2,\mathbf{k}}\right)^2 \delta\left(\omega - \omega_{2,\mathbf{k}}\right) \\ \tilde{\mathcal{S}}_{xx}(\mathbf{k}, \omega) &= 8S\left(Z_{1,\mathbf{k}} + Z_{2,\mathbf{k}}\right)^2 \delta\left(\omega - \omega_{3,\mathbf{k}}\right) \end{aligned} \tag{2.68}$$

as well as $\tilde{\mathcal{S}}_{yy} = \mathcal{S}_{yy}$.

Summary

In summary, based on the J_1-J_2-K spin-Heisenberg model we calculated the low-energy spin wave excitations of both the stripe and the spin-vortex crystal phase. We showed that due to the noncollinear magnetic structure of the SVC phase, the number of Goldstone modes is 3, compared to 2 in the collinear case. The results are consistent with the results obtained in Ref. [63]. The counting of Goldstone modes can be used to uniquely

differentiate between collinear versus non-collinear magnetic orders. Additionally, by a detailed calculation of the spin-spin correlation function, we showed that in the stripe phase, there is one Goldstone mode located at the magnetic ordering wavevector $\mathbf{Q}_1$, and two for the SVC case.

2.5 Conclusions

In this chapter, we investigated the nature and origin of magnetic orders in iron pnictide materials, and proposed direct measurements of various magnetic orders based on Fermi surface reconstruction and collective spin wave excitations.

The significance of C_4 magnetic orders is two-fold. First, C_4 magnetic orders can be realized from an itinerant picture, but not from a localized J_1-J_2 spin-Heisenberg model. This suggests that magnetism in iron pnictide materials are of itinerant nature, and a result of Fermi surface instability. This is different than that in cuprate superconductors. Second, C_4 magnetism competes more strongly with superconductivity than C_2 magnetism. In a collaborative work [37], we showed theoretically that superconducting transition temperature is reduced in the coexisting phase of superconductivity and C_4 magnetism. This was also observed experimentally in $Ba_{1-x}K_xFe_2As_2$ [29].

We also proposed experimental signatures based on Fermi surface reconstruction and collective spin wave excitations. These properties are direct manifestations of the electronic order, rather than relying on magnetoelastic coupling, therefore, they can be used to uniquely determine the nature of the magnetic orders, being stripe, SVC or CSDW magnetism.

Since in iron pnictide materials, both superconductivity and magnetism emerge due to Fermi surface instability, their interplay needs to be placed on an equivalent footing, contrasted to the spin-fermion model described in Ch. 4 Sec. 4.2, where magnetism is assumed to come from physics beyond the Fermi surface. A purely electronic model which captures both physics is described by the Hamiltonian:

$$H = \sum_{i=c,d;\sigma} (\varepsilon_{\mathbf{k}} - \mu)\psi^\dagger_{i\mathbf{k}\sigma}\psi_{i\mathbf{k}\sigma} - U\sum_{\mathbf{r}} \left(\psi^\dagger_{c\alpha}\vec{\sigma}_{\alpha\beta}\psi^\dagger_{d\beta} + h.c.\right)^2 \tag{2.69}$$

where c and d are electronic annihilation operators for two electronic bands (see Ch. 4 Sec. 4.2 for details). This model can be studied using the sign-problem-free Quantum

Monte Carlo method discussed in appendix A, with preliminary results suggesting that both superconductivity and magnetic order can be found by in the $\{T, U\}$ parameter space.

Chapter 3

Origin of electronic nematicity in iron-based superconductors and manifestations in Scanning Tunneling Spectroscopy

3.1 Introduction

As was discussed in Ch. 1 and Ch. 2, in most iron pnictide superconductors, there is a structural phase transition at T_S where the square lattice symmetry (C_4) is broken down to orthorhombic (C_2), followed by a magnetic phase transition at T_N into a stripe magnetic phase, where the spins are ferromagnetically aligned along one of the Fe-Fe bond directions, and antiferromagnetically aligned along the other. Fig. 3.1 is a schematic phase diagram of the iron pnictide materials[21]. While in some materials such as $(Ba_{1-x}K_x)Fe_2As_2$, the two transition temperatures coincide [9], other materials such as $Ba(Fe_{1-x}Co_x)_2As_2$ exhibit an intermediate nematic phase, where the square lattice symmetry is broken while long range magnetic order is absent[17]. The two transition temperatures follow each other closely even in the doped materials, suggesting the intimate relationips between the nematic and magnetic phases.

Although the nematic order manifests itself in both lattice and electronic degrees of

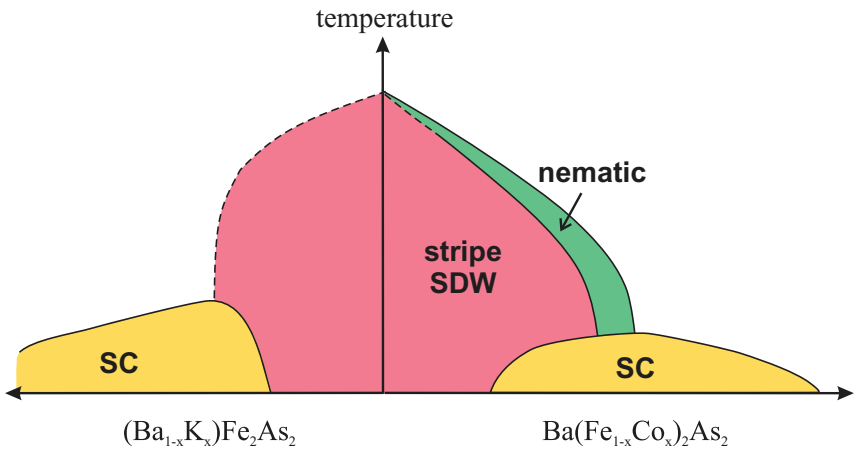

Figure 3.1: Schematic phase diagram of electron-doped (Co-doped) and hole-doped (K-doped) $BaFe_2As_2$, displaying stripe spin-density wave (SDW) order, nematic order, and superconductivity (SC). Taken from Ref. [21].

freedom, various experiments have shown that the nematic order is driven by electronic correlations[75, 76]. For example, in the $Ba(Fe_{1-x}Co_x)_2As_2$ compound, the observed anisotropy is much more pronounced in the electrical resisitivity than in the orthorhombic distortion of the lattice[75, 30]. A more definitive evidence is given by Ref. [76], which showed that T_S marks a divergence of the electronic nematic susceptibility.

There are two main scenarios where electronic nematicity can emerge in the iron pnictide materials, namely, the orbital scenario [77] and the magnetic scenario [74, 44].

In the orbital scenario, the nematic order is due to the electronic system developing an "orbital order" at T_S, where the occupation number of the Fe d_{xz} and d_{yz} orbitals becomes different. The electronic nematic order can be defined by the charge imbalance between the d_{xz} and d_{yz} orbitals: $\phi \propto \langle n_{xz} - n_{yz} \rangle$, where $n_{xz/yz}$ is the occupation number in the corresponding electronic orbital, and $\langle \cdots \rangle$ denotes thermal averaging. In this scenario, electronic nematicity and stripe magnetism do not necessarily come together. This has been used to explain the absence of long range magnetic order in the iron chalcogenide compound FeSe, see Fig. 1.5.

In the magnetic scenario, the nematic order is driven by strong magnetic fluctuations. Following the discussion in Ch. 2, the magnetic order in most iron pnictide materials can be described by two magnetic order parameters $\mathbf{M}_1$ and $\mathbf{M}_2$, with wavevectors

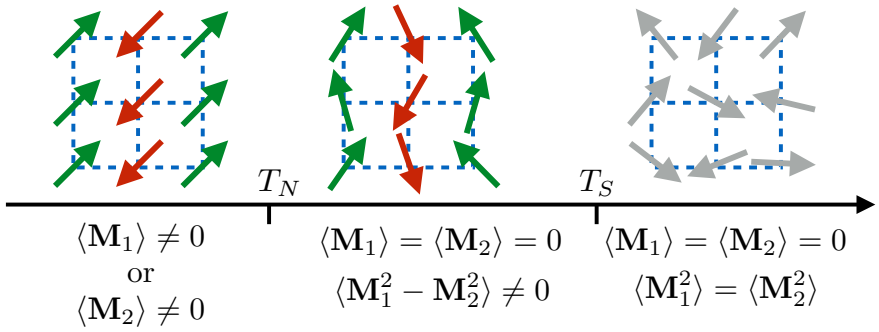

Figure 3.2: Magnetic scenario. The melting of long range stripe magnetic order goes in two steps. First, spin rotational symmetry is restored at T_N. Then, the tetragonal symmetry is restored at T_S.

$\mathbf{Q}_1 = (\pi, 0)$ and $\mathbf{Q}_2 = (0, \pi)$ respectively. In the stripe magnetic phase, either $\mathbf{M}_1$ or $\mathbf{M}_2$ becomes non-zero, which simultaneously breaks the square lattice symmetry (C_4) down to orthorhombic (C_2). If magnetic fluctuations are taken into account, upon raising temperature, the "melting" of the stripe magnetic order can occur in two steps (Here I use the stripe order with $\mathbf{M}_1 \neq 0$ to illustrate the idea): At a temperature T_N, the spin rotational symmetry is restored, and the long range magnetic order is lost. However, the magnetic fluctuations at $\mathbf{Q}_1$ and $\mathbf{Q}_2$ can still be inequivalent, $\langle \mathbf{M}_1^2 \rangle \neq \langle \mathbf{M}_2^2 \rangle$. Therefore, the nematic order parameter $\phi \propto \langle \mathbf{M}_1^2 - \mathbf{M}_2^2 \rangle$ remains non-zero. Only at a higher temperature T_S does the system recover the C_4 symmetry. Fig. 3.2 shows schematically the magnetic scenario. This scenario is very successful at explaining why the nematic phase transition temperature follows the magnetic transition temperature, observed in most iron pnictide materials.

It is important to understand the origin of the electronic nematicity. Not only does it encode the dominant low-energy electronic correlations, but it also constrains the appropriate low-energy effective descriptions of the electronic phase diagram of iron pnictide superconductors. This is a difficult question to answer, because the orbital order and the spin-nematic order breaks the same square lattice symmetry, and therefore will always appear together[78]. On the other hand, the orbital order scenario and the spin-nematic scenario can have quite different experimental manifestations. In particular, the

feedback of nematicity on the electronic and magnetic spectrum can be quite different for these two scenarios [78]. In addition, recent theoretical studies have shown that the two scenarios have opposite effects on the electrical resistivity anisotropy[79].

In this chapter, I will focus on the magnetic scenario. I will first discuss how the electronic nematic order can emerge due to strong magnetic fluctuations. Motivated by recent results on the spectroscopic manifestations of the electronic nematic order [80], I studied the effects of strong stripe antiferromagnetic fluctuations on the local electronic density of states near an impurity. I will show that the spectroscopic results are fully consistent with the predictions from the magnetic scenario.

3.2 Nematicity as a vestigial order to stripe magnetism

This section reproduces previous results published in Ref. [44].

As shown in Ch. 2, the onset of magnetic order in the iron pnictide materials can be described using a Ginzburg-Landau free energy which preserves the spin rotational symmetry and the square lattice symmetry (see also Eq. 2.5):

$$\mathcal{F} = \frac{r_0}{2}(\mathbf{M}_1^2 + \mathbf{M}_2^2) + \frac{u}{4}(\mathbf{M}_1^2 + \mathbf{M}_2^2)^2 - \frac{g}{4}(\mathbf{M}_1^2 - \mathbf{M}_2^2)^2 + w(\mathbf{M}_1 \cdot \mathbf{M}_2)^2 \tag{3.1}$$

The mean-field phase diagram, obtained by minimizing the free energy, has been presented in Fig. 2.4. In particular, the stripe magnetic order becomes the ground state if $g > \min\{0, -w\}$. As was shown in Ch. 2, w can become non-zero when residual electronic interactions or Néel-type antiferromagnetic fluctuations are considered. For simplicity we set $w = 0$. As a result, the criterion for stripe magnetic order becomes $g > 0$.

In the mean-field approximation, both the square lattice symmetry and the spin rotational symmetry are broken at the same temperature, therefore $T_S = T_N$. While this is true for some iron pnictide materials such as $Ba_{1-x}K_xFe_2As_2$, in many other systems they appear as split phase transitions. Theoretically, to see how split nematic and magnetic phase transitions occur, one needs to consider the effects of magnetic fluctuations [44]. We can write down the effective bosonic action for the magnetic order

parameters $\{\mathbf{M}_1, \mathbf{M}_2\}$:

$$S_{\text{eff}} = \frac{1}{2}\int_q \chi_q^{-1}\left(\mathbf{M}_{1q}\cdot\mathbf{M}_{1-q} + \mathbf{M}_{2q}\cdot\mathbf{M}_{2-q}\right) + \frac{1}{4}\int_x \left[u\left(\mathbf{M}_1^2+\mathbf{M}_2^2\right)^2 - g\left(\mathbf{M}_1^2-\mathbf{M}_2^2\right)^2\right] \tag{3.2}$$

Here $q \equiv (\mathbf{q}, i\omega_n)$, and $x \equiv (\mathbf{x}, \tau)$. We used the notation: $\int_q \equiv \sum_n \int_{\mathbf{q}}$, and $\int_x \equiv \int_0^{1/T} \mathrm{d}\tau \int_{\mathbf{x}}$.

The non-interacting magnetic fluctuations are characterized by the propagator (for small momentum and frequency):

$$\chi_q^{-1} \approx r_0 + \mathbf{q}^2 + \gamma|\omega_n| \tag{3.3}$$

where $r_0 \propto T - T_N^{(0)}$, and $T_N^{(0)}$ is the mean-field magnetic transition temperature. γ is the Landau damping parameter, describing the decay of low-energy magnetic fluctuations into electron-hole pairs near the Fermi surface. The Landau damping parameter can be obtained from microscopic electronic models (e.g., Ref. [33, 35]) following the standard Hertz-Millis approach[22, 23, 44]. See also Sec. 4.2.

The partition function is given by $Z = \int \mathcal{D}[\mathbf{M}_1, \mathbf{M}_2]\exp(-S_{\text{eff}})$. To study the effects of magnetic fluctuations, we introduce two Hubbard-Stratonovich fields ψ and ϕ to decouple the quartic interactions:[1]

$$\exp(-S_{\text{eff}}) = \int \mathcal{D}[\psi,\phi]\exp\left\{\frac{\psi^2}{4uT} - \frac{\phi^2}{4gT} - \frac{1}{2}\int_x \left[\psi\left(\mathbf{M}_1^2+\mathbf{M}_2^2\right) + \phi\left(\mathbf{M}_1^2-\mathbf{M}_2^2\right)\right]\right\} \tag{3.4}$$

Variation with respect to $\{\psi, \phi\}$ gives:

$$\psi = u\langle \mathbf{M}_1^2 + \mathbf{M}_2^2\rangle;\ \ \phi = g\langle \mathbf{M}_1^2 - \mathbf{M}_2^2\rangle \tag{3.5}$$

As a result, ψ and ϕ describe the Gaussian magnetic fluctuations and the nematic order parameter respectively. In the absence of long-range magnetic order, $\langle \mathbf{M}_i\rangle = 0$, and the Gaussian magnetic fluctuations can be integrated out to give an effective action for $\{\psi, \phi\}$:

$$\mathcal{S} = -\frac{(r-r_0)^2}{4uT} + \frac{\phi^2}{4gT} + \frac{N}{2}\int_q \ln\left[(r+\mathbf{q}^2+\gamma|\omega_n|)^2 - \phi^2\right] \tag{3.6}$$

[1] Here we work in the normal state before magnetic order condenses. For a treatment of the stripe magnetic phase, see Ref. [44].

where N is the number of spin components, and $r \equiv r_0 + \psi$. We treat $1/N$ as a small parameter, and in the large-N limit, the action can be solved using the saddle point approximation:

$$\begin{aligned} \frac{r - r_0}{2\tilde{u}} &= \int_q \frac{r + \mathbf{q}^2 + \gamma|\omega_n|}{(r + \mathbf{q}^2 + \gamma|\omega_n|)^2 - \phi^2} \\ \frac{\phi}{2\tilde{g}} &= \int_q \frac{\phi}{(r + \mathbf{q}^2 + \gamma|\omega_n|)^2 - \phi^2} \end{aligned} \tag{3.7}$$

where $\tilde{x}$ denotes $x \cdot (TN)$. We can also define the magnetic correlation lengths associated with the magnetic order parameters $\mathbf{M}_{i=1,2}$: $\xi_i^2 \equiv (r \pm \phi)^{-1}$. In the nematic phase, $\phi \neq 0$, and the magnetic fluctuations become inequivalent $\xi_1 \neq \xi_2$. The magnetic phase transition temperature is determined by the criterion $r_c = |\phi|$.

The nature of the nematic and magnetic phase transitions can be determined by solving the coupled saddle point equations Eq. 3.7. To see this, we show one example, where we consider a two-dimensional system at temperatures such that $T\gamma >> \Lambda^2$, where Λ is the upper momentum cutoff. In this limit, only the lowest Matsubara frequency term is relevant, and Eq. 3.7 can be simplified to be [44]:

$$\begin{aligned} \bar{r}_0 &= r + \frac{\tilde{u}}{4\pi} \ln(r^2 - \phi^2) \\ \phi &= \frac{\tilde{g}}{4\pi} \ln \frac{r + \phi}{r - \phi} \\ \bar{r}_0 &\equiv r_0 + \frac{\tilde{u}}{2\pi} \ln \Lambda \end{aligned} \tag{3.8}$$

The second equation gives $r = \phi \coth(2\pi\phi/\tilde{g})$. Substituting into the first equation:

$$\bar{r}_0 = \phi \coth \frac{2\pi\phi}{\tilde{g}} + \frac{\tilde{u}}{2\pi} \ln \left(\phi / \sinh \frac{2\pi\phi}{\tilde{g}} \right) \tag{3.9}$$

By rescaling the fields: $\phi^* \equiv 2\pi\phi/g$, $\bar{\bar{r}}_0 \equiv 2\pi\bar{r}_0/g$, and defining a dimensionless ratio $\alpha \equiv u/g$, we obtain:

$$\bar{\bar{r}}_0 = \phi^* \coth \phi^* + \alpha \ln \left(\frac{\phi^*}{\sinh \phi^*} \right) \tag{3.10}$$

Fig. 3.3 shows the temperature evolution ($\bar{\bar{r}}_0$) of the nematic order parameter for $\alpha = 1.5$ and $\alpha = 2.5$ respectively[44]. For $\alpha > 2$, the nematic phase transition is second order, where upon decreasing temperature ($\bar{\bar{r}}_0$), the first solution is $\phi^* = 0_+$. For $\alpha < 2$, the nematic phase transition becomes first order, marked by a finite jump of the order parameter, i.e., the first solution is at $\phi^* = \phi_0^* \neq 0$.

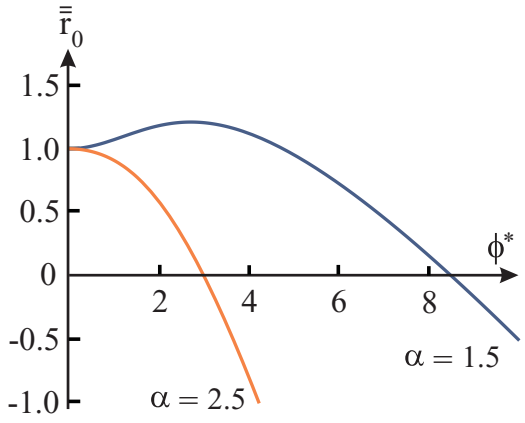

Figure 3.3: Temperature evolution of the nematic order parameter for $u/g = 2.5$ (orange) and $u/g = 1.5$ (blue) respectively. The nematic phase transition is second order for $u/g = 2.5$, and first order for $u/g = 1.5$. The first order transition is marked by a finite jump of the nematic order parameter at the transition temperature. Taken from Ref. [44].

Note that in two space dimensions, there is no magnetic phase transition at a finite temperature. This is due to the Mermin-Wagner theorem, which states that there is no continuous symmetry breaking in two dimensions. This can easily be seen from the saddle point equations, in that $r = \phi$ (meaning a divergent magnetic correlation length $\xi^2 = 1/(r - \phi)$) can never be satisfied.

3.3 Spectroscopic manifestations of electronic nematic order driven by magnetic fluctuations

Having understood how electronic nematic order can emerge in the magnetic scenario, we proceed to look at its experimental manifestations. In particular, we want to understand the differences between the magnetic and the orbital scenario.

As discussed previously, in these two scenarios, the effects of electronic nematic order on the low-energy electronic spectrum are quite different[21]. For the magnetic scenario, the nematic order is accompanied by large stripe-like antiferromagnetic fluctuations, which may even open a "pseudogap" near the Fermi level. In the orbital scenario, the key effect is a Pomeranchuk distortion of the Fermi surface induced by orbital

polarization[77].

Experimentally, scanning tunneling microscopy (STM) provides a direct visualization of the low-energy electronic properties. The key quantity measured in STM is the local tunneling conductance at a given voltage bias eV. It can be shown that the tunneling conductance is proportional to the local electronic density of states $n(\mathbf{r}, \omega = eV)$ (LDOS), given by the imaginary part of the momentum-integrated one-particle Green's function:

$$n(\mathbf{r},\omega) = -\frac{1}{\pi\mathcal{V}} \int_{\mathbf{k}_1,\mathbf{k}_2} \exp[i(\mathbf{k}_1 - \mathbf{k}_2)\cdot\mathbf{r}] \mathrm{Im}G\left(\frac{\mathbf{k}_1+\mathbf{k}_2}{2}, \mathbf{k}_1 - \mathbf{k}_2; \omega + i\delta\right) \tag{3.11}$$

Here δ is the quasiparticle decay rate, and $\mathcal{V}$ is the volume.

For translationally invariant systems, the electronic Green's function depends only on the center of mass momentum: $\mathbf{k}_1 = \mathbf{k}_2$, and the LDOS is spatially homogeneous. In the presence of an impurity, the translational symmetry is broken, and interference patterns appear. In particular, for a weak non-magnetic point-like impurity potential described as $V(\mathbf{r}) = -\alpha\delta(\mathbf{r})$, the LDOS can be calculated using the Born approximation:

$$\begin{aligned} n(\mathbf{r},\omega) &= n_0(\omega) + \delta n(\mathbf{r},\omega) \\ \delta n(\mathbf{r},\omega) &= \alpha \mathrm{Im}\chi(\mathbf{r},\omega) \end{aligned} \tag{3.12}$$

Here $\chi(\mathbf{r},\omega) \propto \int_{\mathbf{k}_1,\mathbf{k}_2} \exp[i(\mathbf{k}_1-\mathbf{k}_2)\cdot\mathbf{r}] G_0(\omega+i\delta,\mathbf{k}_1) G_0(\omega+i\delta,\mathbf{k}_2)$, where G_0 is the electronic Green's function unrenormalized by impurity scattering.[2] As a result, the LDOS near an impurity is sensitive to various electronic correlations, encoded in the electronic Green's functions. The quasiparticle interference patterns $|\delta n(\mathbf{q},\omega)|$ (QPI), defined as the absolute Fourier transform of the LDOS, are intimately related to properties of the Fermi surface.

The spectroscopic patterns (both LDOS and QPI) as measured by STM are great tools to study electronic nematicity. In particular, by comparing the patterns in the nematic phase and in the stripe magnetic phase, we can infer the origin of nematic order in iron pnictide compounds.

In this section, I will discuss a collaborative work on the scanning tunneling spectroscopy measurements of a typical iron pnictide compound NaFeAs. This work has

[2] A more rigorous analysis of the LDOS near a non-magnetic impurity is done later.

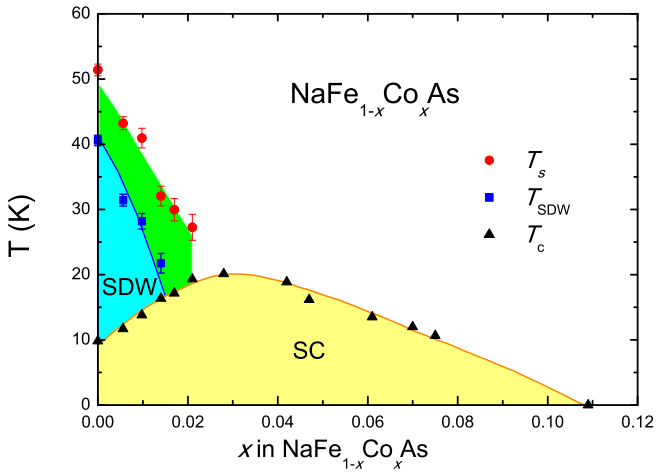

Figure 3.4: Phase diagram of $NaFe_{1-x}Co_xAs$. The colors refer to the nematic phase (green), the stripe magnetic phase (cyan, also labeled as SDW), and the superconducting phase (yellow). From Ref. [82].

been submitted, and is listed in Ref. [81]. The experimental part of the work is led by Prof. Abhay Pasupathy's group from Columbia University, while I led the theoretical part.

3.3.1 Experimental results

NaFeAs is a typical material of the 111 family of iron pnictide superconductors. The parent compound has two known phase transitions: a structural phase transition at $T_S = 52K$ which breaks the lattice tetragonal symmetry (C_4) down to orthorhombic (C_2), and a magnetic phase transition at $T_N = 41K$ into the stripe magnetic phase. Superconductivity is achieved by Cobalt doping, i.e., $NaFe_{1-x}Co_xAs$, with a maximum $T_c = 20K$ at $x \approx 0.028$. Fig. 3.4 shows the phase diagram obtained from resistivity and susceptibility measurements[82].

Ref. [81] performed spectroscopic studies of $NaFe_{1-x}Co_xAs$ for a variety of temperatures and dopings. Here I describe the two main results.

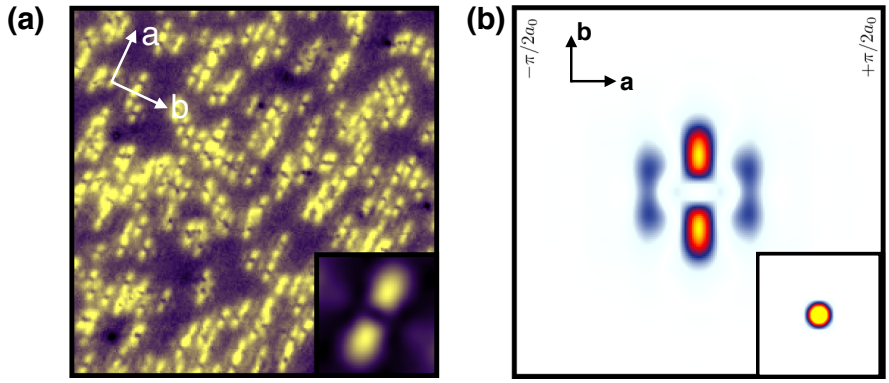

Figure 3.5: LDOS and QPI in the stripe magnetic phase, obtained at 26K. (a) LDOS in a 100nm×100nm real space image at bias voltage 10meV. Inset is the extracted LDOS near a single impurity. (b) QPI plotted for $k_x, k_y \in (-\pi/2, \pi/2)$. Inset is the QPI in the normal state. The Fe-Fe bond directions are labeled by a and b, where a denotes the stripe magnetic ordering direction. The figure is adapted from Ref. [81].

LDOS and QPI in the stripe magnetic phase

Fig. 3.5(a) shows the LDOS in the stripe magnetic phase ($T = 26K$). In the LDOS map, the square lattice symmetry is broken down to orthorhombic. The patterns near a single impurity are extracted and shown in the inset. It displays two bright lobes along the magnetic ordering wavevector direction, with a separation of about 10 lattice constants. Fig. 3.5(b) shows the QPI, defined as the absolute Fourier transformation of the LDOS near a single impurity. Notably, the patterns exhibit a three-stripe structure along the magnetic ordering wavevector. This is to be contrasted with the normal state, which shows an isotropic "blob", as depicted in the inset.

LDOS and QPI in the nematic phase

Fig. 3.6 shows the LDOS and QPI in the nematic phase. The results are obtained in the normal state ($T = 54K$) by applying a uniaxial strain. Both the LDOS and QPI patterns are quite similar to the stripe magnetic phase.

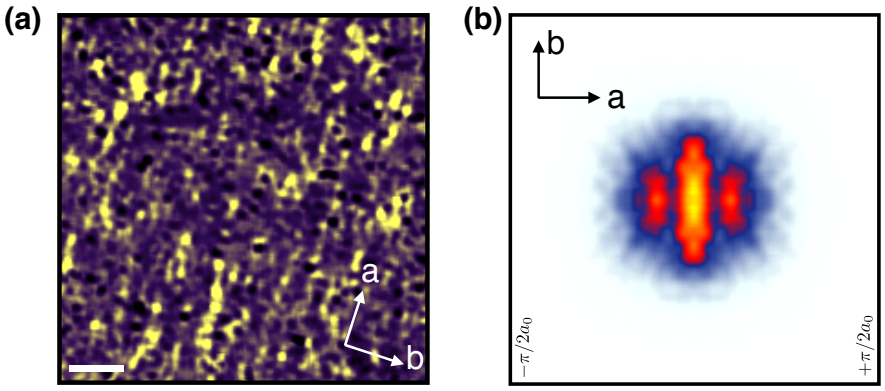

Figure 3.6: LDOS and QPI in the nematic phase, obtained from the normal state (54K) subject to an uniaxial strain. The Fe-Fe bond directions are labeled by a and b, where a denotes the stripe magnetic ordering direction. Different than the 26K data presented in Fig. 3.5, the LDOS near a single impurity is difficult to extract. As a result, the QPI is obtained by Fourier transforming the entire LDOS image. The difference compared to Fig. 3.5 is the presence of a bright peak at Brillouin zone center. This is due to averaging of impurities, and not a feature of the electronic properties. The figure is adapted from Ref. [81].

Temperature evolution of electronic anisotropy

The degree of electronic anisotropy can be quantified by an anisotropy parameter η, defined as the ratio between the absolute difference in the LDOS near a single impurity over the absolute LDOS intensity:

$$\eta \equiv \frac{\sum_{\mathbf{r}} |n(\mathbf{r}, eV) - n(\tilde{\mathbf{r}}, eV)|}{\sum_{\mathbf{r}} |n(\mathbf{r}, eV)|} \tag{3.13}$$

Here $\tilde{\mathbf{r}} \equiv (y, -x)$ is the 90-degree rotation with respect to $\mathbf{r}$. Fig. 3.7 shows the temperature evolution of the anisotropy parameter (red dots). The sharp increase of the electronic anisotropy coincides with the onset of long range stripe magnetic order.

3.3.2 Theoretical analysis

This subsection is written based on the supplementary material to Ref. [81].

In the earlier section, I presented the spectroscopic results of NaFeAs, focusing on the measurement of the electronic anisotropy in the nematic and magnetic phases. Can these results be explained by a magnetic origin of the electronic nematicity?

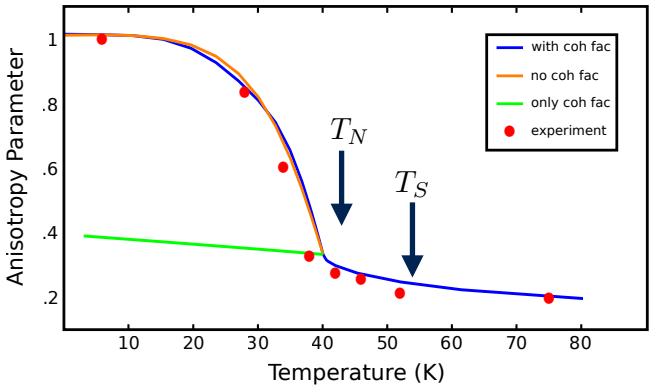

Figure 3.7: Temperature evolution of the anisotropy parameter. The nematic and magnetic phase transitions are labeled by T_S and T_N respectively. Blue, orange and green lines are theoretical calculations. The orange line is obtained by neglecting the effect of coherence factors due to Brillouin zone folding, but the effects of Fermi surface (FS) reconstruction (namely, poles of electronic Green's function) are included. The green line neglects FS reconstruction, but considers coherence factor effects. Blue line includes both. Figure is adapted from Ref. [81].

As discussed in the beginning of this section, the spectroscopic images encode the low-energy electronic properties. In the stripe magnetic phase, an energy gap opens near the Fermi surface. The three-stripe structure observed in the QPI (Fig. 3.5) should be manifestations of the Fermi surface (FS) reconstruction. On the other hand, the nematic phase does not have long range magnetic order, and therefore there is no FS reconstruction. However, in the magnetic scenario, the nematic phase is accompanied by large-amplitude stripe antiferromagnetic fluctuations [21]. The magnetic fluctuations strongly renormalize the electronic Green's function, which can be incorporated as a self-energy effect. This can open a "pseudogap" near the Fermi surface, and act as a "precursor" to the FS reconstruction.

To put the above qualitative arguments in more concrete form, I studied a low-energy effective model based on the magnetic scenario, and calculated the LDOS and QPI in the nematic and magnetic phases theoretically [81]. The calculation follows an earlier publication Ref. [80]. Below I first describe the model, and then make comparisons to the experimental results.

Model

The low-energy electronic band dispersions of NaFeAs were measured using angle-resolved photoemission spectroscopy (ARPES), which revealed two hole-like bands at the center of the one-Fe Brillouin zone (labeled by Γ), and two electron-like bands at the zone boundaries $(\pi,0)/(0,\pi)$ (labeled by X and Y)[83]. To reconstruct the ARPES measurements, I use a four-band model with band dispersions described as follows. The band dispersions of the two hole pockets are given in terms of a function

$$h(\alpha) = -\mu_\gamma + b\left[2\alpha(1-\cos k_x) + \frac{2}{\alpha}(1-\cos k_y)\right]$$

as:

$$\begin{aligned}
\varepsilon_{\gamma_1\mathbf{k}} &= \frac{1}{2}\left[h(\alpha_\gamma) + h(\frac{1}{\alpha_\gamma})\right] + \frac{1}{2}\sqrt{\left[h(\alpha_\gamma) - h(\frac{1}{\alpha_\gamma})\right]^2 + W^2} \\
\varepsilon_{\gamma_2\mathbf{k}} &= \frac{1}{2}\left[h(\alpha_\gamma) + h(\frac{1}{\alpha_\gamma})\right] - \frac{1}{2}\sqrt{\left[h(\alpha_\gamma) - h(\frac{1}{\alpha_\gamma})\right]^2 + W^2}
\end{aligned} \tag{3.14}$$

while the band dispersions of the electron pockets are:

$$\begin{aligned}
\varepsilon_{X\mathbf{k}+\mathbf{Q}_1} &= -\mu_e + b\left[2\alpha_e(1-\cos k_x) + \frac{2}{\alpha_e}(1-\cos k_y)\right] \\
\varepsilon_{Y\mathbf{k}+\mathbf{Q}_2} &= -\mu_e + b\left[2\alpha_e(1-\cos k_y) + \frac{2}{\alpha_e}(1-\cos k_x)\right]
\end{aligned} \tag{3.15}$$

The parameters are: $b = 4$, $\mu_\gamma = -0.17$, $\alpha_\gamma = -2$, $W = 0.12$, $\mu_e = 0.32$, and $\alpha_e = 0.4$. Here, all energy scales are measured in units of $\varepsilon_0 \approx 300meV$, such that the bottom of the electron band is about 100meV below the Fermi level, consistent with ARPES measurements [83]. Fig. 3.8 shows the Fermi surface of the four electron bands.

Effects of stripe magnetic order and magnetic fluctuations on the low-energy electronic properties

For definiteness we choose the magnetic ordering wavevector to be $\mathbf{Q}_1 = (\pi, 0)$.

In the magnetic phase, $\langle \mathbf{M}_1 \rangle \neq 0$. We use Δ_{SDW} to denote the amplitude of the order parameter. A non-zero Δ_{SDW} couples the wavevector $\mathbf{k}$ to $\mathbf{k}+\mathbf{Q}_1$, in particular mixing the X electron band to the two hole bands (For simplicity, we include only the coupling to the band γ_1 with the larger Fermi surface) and opening a gap, thereby changing

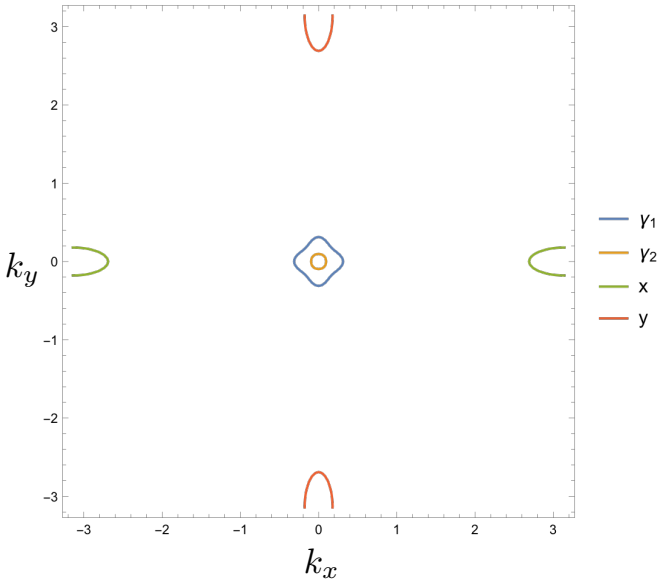

Figure 3.8: Fermi surface of our effective four band model, constructed from the ARPES measurements [83]. Figure taken from Ref. [81].

the dispersion. In the nematic phase, long range magnetic order is destroyed by phase fluctuations, $\langle \mathbf{M}_1 \rangle \to 0$, so that there is no coherent coupling between $\mathbf{k}$ and $\mathbf{k} + \mathbf{Q}_1$. However, the amplitude fluctuations $\langle \mathbf{M}_1^2 \rangle - \langle \mathbf{M}_1 \rangle^2 \equiv \Delta_{\text{LRA}}^2$ remain non-vanishing, so that a "pseudogap" is opened.

We represent the above discussions mathematically via an 8×8 matrix electronic Green's function $\mathcal{G}_\sigma$ including both $\mathbf{k}$ and $\mathbf{k} + \mathbf{Q}_1$ terms as:

$$\mathcal{G}_\sigma = \begin{pmatrix} g_{\gamma_1} & 0 & 0 & 0 & 0 & \sigma f & 0 & 0 \\ 0 & \tilde{g}_{\gamma_1} & 0 & 0 & \sigma \tilde{f} & 0 & 0 & 0 \\ 0 & 0 & g_{\gamma_2} & 0 & 0 & 0 & 0 & 0 \\ 0 & 0 & 0 & \tilde{g}_{\gamma_2} & 0 & 0 & 0 & 0 \\ 0 & \sigma \tilde{f} & 0 & 0 & g_X & 0 & 0 & 0 \\ \sigma f & 0 & 0 & 0 & 0 & \tilde{g}_X & 0 & 0 \\ 0 & 0 & 0 & 0 & 0 & 0 & g_Y & 0 \\ 0 & 0 & 0 & 0 & 0 & 0 & 0 & \tilde{g}_Y \end{pmatrix} \tag{3.16}$$

where the normal (g) and anomalous (f) parts of $\mathcal{G}_\sigma$ are:

$$\begin{aligned} g_{\gamma_1}(\mathbf{k},\omega) &= \left(\omega - \varepsilon_{\gamma_1\mathbf{k}} - \frac{\langle \mathbf{M}_1^2\rangle}{\omega - \tilde{\varepsilon}_{X\mathbf{k}} + i\xi^{-1}}\right)^{-1} \\ \tilde{g}_X(\mathbf{k},\omega) &= \left(\omega - \tilde{\varepsilon}_{X\mathbf{k}} - \frac{\langle \mathbf{M}_1^2\rangle}{\omega - \varepsilon_{\gamma_1\mathbf{k}} + i\xi^{-1}}\right)^{-1} \\ g_Y(\mathbf{k},\omega) &= (\omega - \varepsilon_{Y\mathbf{k}})^{-1} \\ g_{\gamma_2}(\mathbf{k},\omega) &= (\omega - \varepsilon_{\gamma_2\mathbf{k}})^{-1} \\ f(\mathbf{k},\omega) &= \frac{\Delta_{\mathrm{SDW}}}{(\omega - \varepsilon_{\gamma_1\mathbf{k}})(\omega - \tilde{\varepsilon}_{X\mathbf{k}}) - \langle \mathbf{M}_1^2\rangle} \end{aligned} \tag{3.17}$$

σ denotes the electron spin and a tilde denotes the same function evaluated at $\mathbf{k}+\mathbf{Q}_1$. Following Ref. [80], we have also included a phenomenological broadening parameter ξ measured in units of the lattice spacing a and related to the correlation length of the magnetic phase fluctuations.

The extra terms in g_{X,γ_1} are proportional to $\langle \mathbf{M}_1^2\rangle \equiv \Delta_{\mathrm{SDW}}^2 + \Delta_{\mathrm{LRA}}$, and express the effect of coherent and incoherent magnetic fluctuations in opening a gap. This form of the self-energy has also been used by Lee-Rice-Anderson in Ref. [84] to describe the fluctuation effects at a Peierls transition. f expresses the effect of coherent backscattering associated with long ranged order.

We distinguish the normal state ($\Delta_{\mathrm{SDW}} = \Delta_{\mathrm{LRA}} = 0$), the nematic phase ($\Delta_{\mathrm{SDW}} = 0$, $\Delta_{\mathrm{LRA}} \neq 0$) and the stripe magnetic phase ($\Delta_{\mathrm{SDW}} \neq 0$, $\Delta_{\mathrm{LRA}} \neq 0$).

Calculating the LDOS and QPI

We now use standard formulas to compute the change in density of states, $\delta n(\mathbf{r},\omega)$, due to a non-magnetic impurity located at the origin $\mathbf{r} = 0$. In the first Born approximation, we have

$$\delta n(\mathbf{r},\omega) = -\frac{1}{\pi}\mathrm{Im}\mathrm{Tr}\left[\hat{M}G_\sigma(\mathbf{r},\omega+i\delta)\hat{V}G_\sigma(-\mathbf{r},\omega+i\delta)\right] \tag{3.18}$$

where $G_\sigma(\mathbf{r},\omega+i\delta)$ is the Fourier transform of the $\mathcal{G}_\sigma$ defined above, $\hat{M}$ the square of the matrix element linking the STM tip to the band states, and $\hat{V}$ the impurity scattering. We make the simplifying assumptions that the impurity scattering potential and STM matrix elements are momentum and band independent (i.e., connecting all momenta to all momenta and all bands to all bands, with equal amplitudes). $\delta =$

0.03 is a phenomenological broadening parameter corresponding to STM measurement resolution. Carrying out the sum one finds:

$$\delta n(\mathbf{r},\omega) = -\frac{VM}{\pi}\mathrm{Im}\sum_{\sigma}\left[\sum_{ij} G_{ij}(\mathbf{r},\omega+i\delta)\right]\left[\sum_{kl} G_{kl}(-\mathbf{r},\omega+i\delta)\right] \tag{3.19}$$

where the Roman indices denote elements of the G matrix defined above. Carrying out the sum over elements and spin degrees of freedom we find (the 2 is from the spin sum):

$$\begin{aligned}
\delta n(\mathbf{r},\omega) &= -\frac{2VM}{\pi}\left[\delta n_1(\mathbf{r},\omega) + \delta n_2(\mathbf{r},\omega)\right] \\
\delta n_1(\mathbf{r},\omega) &= \mathrm{Im}\sum_{ij}\left(g_i(\mathbf{r},\omega+i\delta) + \tilde{g}_i(\mathbf{r},\omega+i\delta)e^{i\mathbf{Q}_1\cdot\mathbf{r}}\right)\left(g_j(-\mathbf{r},\omega+i\delta) + \tilde{g}_j(-\mathbf{r},\omega+i\delta)e^{-i\mathbf{Q}_1\cdot\mathbf{r}}\right) \\
\delta n_2(\mathbf{r},\omega) &= 2(1+\cos(\mathbf{Q}_1\cdot\mathbf{r}))\left[f(\mathbf{r},\omega+i\delta) + \tilde{f}(\mathbf{r},\omega+i\delta)\right]\left[f(-\mathbf{r},\omega+i\delta) + \tilde{f}(-\mathbf{r},\omega+i\delta)\right]
\end{aligned} \tag{3.20}$$

$\delta n(\mathbf{r},\omega)$ defined in this way may be directly compared to the experimentally determined LDOS associated with a single impurity. To achieve consistency with experimental results, rather than directly computing the QPI in momentum space, we compute it by Fourier transforming the LDOS on a square image of 24×24 lattice constants and taking the absolute value.

QPI in the normal state, nematic and magnetic phase

Fig. 3.9 shows a sequence of calculated QPIs in the normal state, nematic, and magnetic phase.

Let us first look at the QPI in the magnetic phase shown in Fig. 3.9(e), calculated with $\Delta_{\mathrm{LRA}} = 0.052$, $\Delta_{\mathrm{SDW}} = 0.1$, and the broadening parameter $\xi^{-1} = 0$. Compared to the normal state (Fig. 3.9(a)), we observe that the spectral weights along the magnetic ordering wavevector direction are reduced. This is because the segments of the Fermi surfaces along this direction are gapped out due to the magnetic order. The calculated QPI is quite similar compared to the experimental result shown in Fig. 3.9(f) and Fig. 3.5. This offers strong evidence of QPI induced by FS reconstruction.

Next, let us look at the QPI in the nematic phase, shown in Fig. 3.9(b-d) for different fluctuation amplitudes Δ_{LRA} and correlation lengths ξ. We see that the QPIs are similar

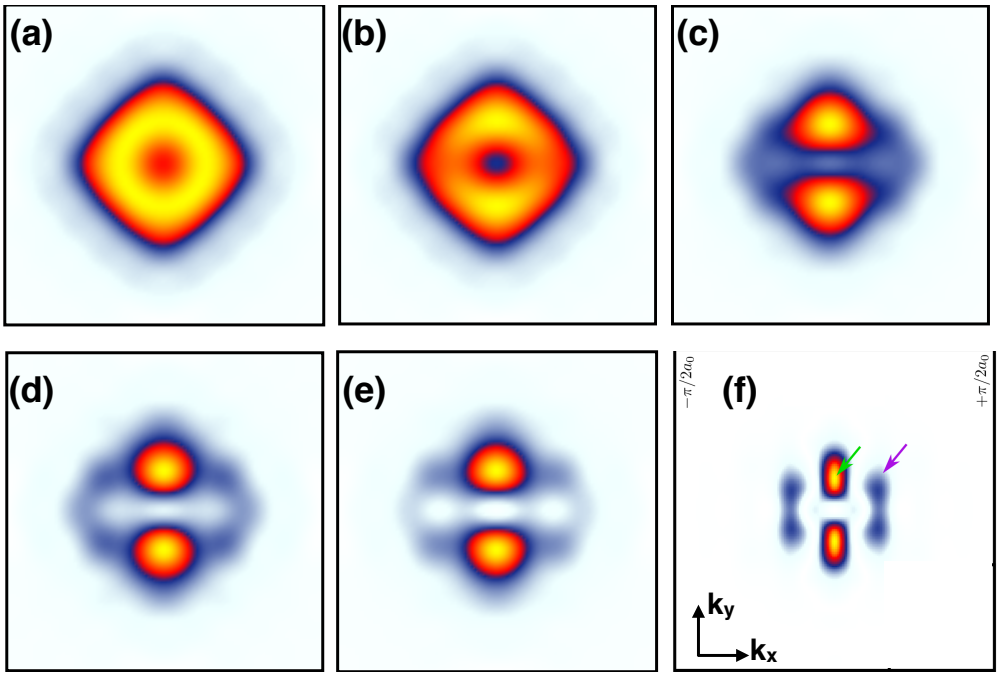

Figure 3.9: QPI calculated in the normal state (a), nematic (b-d) and magnetic phase (e), plotted for $k_x, k_y \in (-\pi/2, \pi/2)$. (f) is the experimental QPI at $T = 26K$, also shown in Fig. 3.5. The parameters used for the nematic phase are: (b) $\Delta_{\mathrm{LRA}} = 0.05$ and $\xi^{-1} = 0.05$, (c) $\Delta_{\mathrm{LRA}} = 0.1$ and $\xi^{-1} = 0.05$, and (d) $\Delta_{\mathrm{LRA}} = 0.1$ and $\xi^{-1} = 0$. The parameters used for the magnetic phase are $\Delta_{\mathrm{LRA}} = 0.052$, $\Delta_{\mathrm{SDW}} = 0.1$, and $\xi^{-1} = 0$. Figure adapted from Ref. [81].

to the magnetic phase when the fluctuation amplitude becomes comparable to the long ranged order.

To understand the similarities of the QPIs in the nematic and magnetic phase, we note that in our model calculations, the difference lies in the anomalous Green's function f defined in Eq. 3.16. The presence of f introduces coherent backscattering, namely, the momentum states outside of the magnetic Brillouin zone can be coherently scattered back via $\mathbf{k} + \mathbf{Q}_1 \rightarrow \mathbf{k}$. The similarities between the QPIs calculated in the nematic and magnetic phase show that the dominant features come from gap opening rather than coherent backscattering.

To further illustrate this, in Fig. 3.7 I present three calculations of the anisotropy parameter in the magnetic phase, by considering only coherent backscattering (green

line), only gap opening (orange line), and taking both into account (blue line). Here to fit the experimental results, I used a mean-field like ansatz for the magnetic correlation length ξ and the order parameter Δ_{SDW}:

$$\xi^{-1} = \xi_0^{-1}\sqrt{\frac{T - T_N}{T_S - T_N}};\ \Delta_{\mathrm{SDW}} = \Delta_0\sqrt{1 - \frac{T}{T_N}} \tag{3.21}$$

with $T_N = 40K$, $T_S = 52K$, $\Delta_0 = 0.14$, and $\Delta_{\mathrm{LRA}} = 0.052$. It is clear that the presence of coherent backscattering only introduces a minimal electronic anisotropy when compared to gap opening.

Summary

In summary, I presented a theoretical calculation of the spectroscopic patterns using a low-energy four-band model fitted to the ARPES measurements. I showed that in the magnetic scenario, the QPI patterns due to a non-magnetic point-like impurity can be understood as due to gap opening near the Fermi surface. The similarities between QPIs in the nematic and magnetic phases can be explained by large-amplitude magnetic fluctuations in the nematic phase opening a "pseudogap" in the electronic spectrum. The dominant electronic anisotropy also comes from the gap opening, rather than coherent backscattering due to the onset of long range magnetic order.

3.4 Conclusions

In this chapter, I first discussed two scenarios where electronic nematic order can emerge in the iron pnictide materials, namely, the orbital scenario, where nematicity is due to spontaneous symmetry breaking between Fe d_{xz} and d_{yz} orbitals, and the magnetic scenario, where it is a "vestigial" order due to partial melting of the long range stripe magnetic order.

Focusing on the magnetic scenario, I discussed in detail how nematic order can emerge due to strong magnetic fluctuations. By studying an effective bosonic action describing the magnetic fluctuations, I discussed the nature of the nematic phase transition and how it is related to the quartic terms describing the interactions between magnetic fluctuations.

I proceeded to discuss the experimental manifestations of electronic nematic order, focusing on the differences between the orbital scenario and the magnetic scenario. In particular, I studied the feedback effects of nematicity on the electronic spectrum near the Fermi level, and discussed the spectroscopic manifestations. I argued that the experimental results can be fully understood within the magnetic scenario. In addition, I showed that the dominant source of electronic anisotropy comes from gap opening, rather than coherent backscattering due to the translational symmetry breaking inside the magnetic phase.

Chapter 4

Antiferromagnetic quantum criticality and numerical solutions of the spin-fermion model

4.1 Introduction

As was discussed in Ch. 1, in the electronic phase diagram of most cuprate and iron pnictide materials, superconductivity is found in proximity to some form of antiferromagnetic order. Most interestingly, superconductivity is induced by suppressing the magnetic order via doping or pressure, and the maximum superconducting transition temperature is close to a "putative" magnetic quantum phase transition. In addition, the normal state electronic properties also deviate from Landau Fermi liquid description. This is particularly true for cuprates with electron doping (Fig. 1.4) and iron pnictides (Fig. 1.5) with either electron or hole doping.[1] Multiple experiments have hinted that the quantum phase transition is second order, and marked by a quantum critical point (QCP)[85, 86, 87, 88]. However, the definitive evidence of a magnetic QCP is lacking. Moreover, some theoretical calculations for iron pnictide materials suggest that the magnetic quantum phase transition can be first order [44]. Nonetheless, it is

[1] For hole-doped cuprates, the antiferromagnetic order is totally suppressed before the onset of superconductivity. However, the maximum T_c appears to be located where the pseudogap temperature extrapolates to zero.

important to see if the presence of a magnetic QCP is responsible for the enhanced T_c and exotic electronic properties.

So far, despite intense theoretical efforts in this frontier[13, 89, 14, 15, 23, 90], the relevance of magnetic QCP remains to be fully addressed. This is partially due to the difficulties to find a magnetic QCP in microscopic models, such as the Hubbard model. On the other hand, low energy effective models can be constructed, taking quantum critical magnetic fluctuations and low energy electrons as inputs rather than outputs. Such models have the advantage of working directly with QCP, albeit it remains a challenging task to show how they can be derived from microscopic models.

One of the simplest and most studied low energy models is the spin-fermion model. Over the past twenty years, many analytical works have been done analyzing its properties, producing fruitful results. In particular, both superconductivity and charge density wave are enhanced near a magnetic QCP. The non-Fermi liquid properties are also captured. Nonetheless, there are fundamental issues associated with the various approximations schemes used to solve the spin-fermion model, making the conclusions unreliable.

In recent years, a sign-problem-free Monte Carlo technique has been proposed [91] for the spin-fermion model, offering for the first time unbiased solutions. In particular, Ref. [92, 93] presented a thorough characterization of both the phase diagram and the low energy electronic/magnetic properties.

In this chapter, I will present our contributions to the understanding of the spin-fermion model. In particular, we combined both analytical and numerical methods to address the microscopic origin and system parameters controlling the low energy physics. A big part of the work presented here has been published in Ref. [94]. A later discussion on the charge density wave physics is based on an unpublished work.

The chapter is organized as follows: In Sec. 4.2, I will present the spin-fermion model, and the Eliashberg approximation used to obtain superconducting and charge density wave properties. In Sec. 4.3, I will briefly describe the Determinantal Quantum Monte Carlo (DQMC) technique and its application to the study of the spin-fermion model. I will then present two main works, one on the validity of the Eliashberg approach and microscopic parameters governing the superconducting transition temperature (Sec. 4.4), the other on the charge density wave physics near magnetic QCP, and its interplay with

superconductivity (Sec. 4.5).

4.2 The spin-fermion model

The spin-fermion model describes quantum critical spin fluctuations coupled to low-energy electrons. One of the earliest proposals to address the properties in cuprate materials is in Ref. [95]. Below I give a quantitative definition of the model. The discussion reproduces some of the results presented in Ref. [13, 14].

The spin-fermion model assumes long range magnetic order coming from high energy states away from the Fermi surface. The spin fluctuations[2] are described by a Orstein-Zenike type propagator:

$$\chi_{ij}^{(0)}(\mathbf{q}, i\Omega_n) = \frac{\delta_{ij}}{r_0 + (\mathbf{q}-\mathbf{Q})^2 + \Omega_n^2/v_s^2} \tag{4.1}$$

where $i, j = x, y, z$ represents the spin components, v_s the spin fluctuation velocity, and $\Omega_n = 2\pi nT$ is the bosonic Matsubara frequency. $r_0 = \xi^{-2}$, where ξ is the magnetic correlation length. At a magnetic QCP, the correlation length diverges and $r_0 \to 0$. At finite temperatures, the quantum critical fluctuations gain a finite mass which is some function of temperature. Spin fluctuations are strongly momentum dependent, and peaked at the magnetic ordering wavevector. In the case of cuprates, the magnetic order is the Néel order with wavevector $\mathbf{Q} \equiv (\pi/a, \pi/a)$, where a is the lattice constant corresponding to the Cu-Cu distance on the square lattice (see Fig. 1.2 for the crystal structure).

The low-energy electronic properties are described by the Hamiltonian:

$$H = \sum_{\mathbf{k}\alpha} c_{\mathbf{k}\alpha}^{\dagger}(\varepsilon_{\mathbf{k}} - \mu)c_{\mathbf{k}\alpha} \tag{4.2}$$

where $c_{\mathbf{k}\alpha}$ annihilates one electron with momentum $\mathbf{k}$ and spin state α. $\varepsilon_{\mathbf{k}}$ describes the energy dispersion, and μ is the chemical potential. As an example, in Fig. 4.1, we show the band dispersion constructed based on ARPES measurements of overdoped cuprates, adapted from Ref. [96]. There are special points on the Fermi surface called the *hot spots*. A pair of hot spots is connected by the magnetic ordering wavevector. In later sections I will show how the properties of the hot spots uniquely determine the superconducting properties.

[2] I will use spin fluctuations and magnetic fluctuations interchangeably.

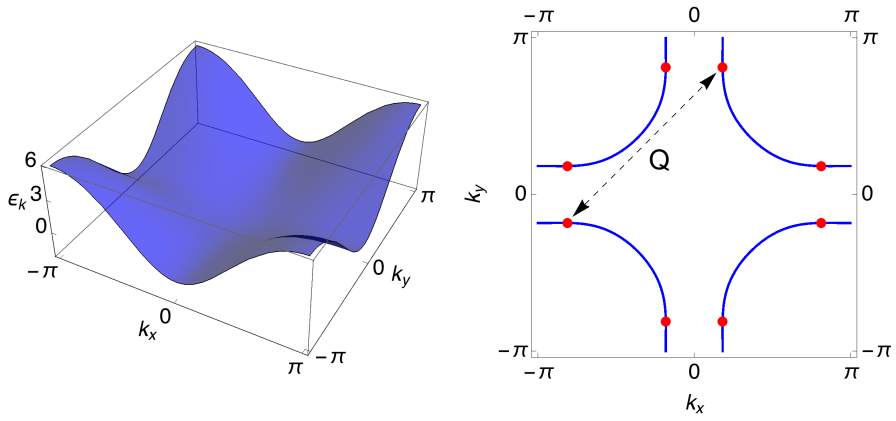

Figure 4.1: Band dispersion (left panel) and Fermi surface (right panel) based on ARPES measurements of optimally doped $Bi_2Sr_2CuO_{6+x}$[96]. Red points on the Fermi surface label hot spots. $\mathbf{Q} = (\pi/a, \pi/a)$ is the magnetic ordering wavevector.

The simplest form of spin-fermion coupling is local in space time coordinates:

$$H_\lambda = \lambda \sum_{\mathbf{kq};\alpha\beta} \vec{\phi}_{\mathbf{q}} \cdot c^\dagger_{\mathbf{k+q}\alpha} \vec{\sigma}_{\alpha\beta} c_{\mathbf{k}\beta} \tag{4.3}$$

where $\vec{\phi} = (\phi_x, \phi_y, \phi_z)$ is the bosonic field describing spin fluctuations (Eq. 4.1).

Eqs. 4.1, 4.2, and 4.3 define the spin-fermion model.

The low energy properties of the spin-fermion model have been studied following field theoretical renormalization group approach [14]. Ref. [97, 14] pointed out that in two space dimensions, the spin-fermion coupling cannot be treated perturbatively. Other forms of perturbative schemes based on artificially small parameters have been used, such as large-N approximation [13] where N is the number of electron flavors, dimensional regularization ($\epsilon \equiv 3 - d$)[98] and so on. However, analytical difficulties exist even within these approximation schemes [97, 14].

One of the well-established frameworks to study various electronic orders is the Eliashberg approach. It is a self-consistent treatment of the electronic self-energy due to the coupling to a boson. It is a powerful technique to obtain quantitative values of the transition temperatures of various electronic orders, as well as the corresponding susceptibilities in the disordered phase.

The validity of the Eliashberg approach relies on the Migdal's theorem, i.e., the set

of Feynman diagrams corresponding to corrections of the electron-boson coupling (so-called "vertex correction") can be neglected. The Eliashberg approach is justified for the strong-coupling electron-phonon problem, because the vertex corrections are small in the ratio between the Debye frequency and the Fermi energy, i.e., $\delta\mathcal{V} \sim \omega_D/E_F \ll 1$. In the spin-fermion model, because the spin fluctuations are electronic in nature, such an energy scale separation is by no means obvious. Nonetheless, it is important to see what the Eliashberg predictions are.

4.2.1 Eliashberg approach and superconductivity

To see how Eliashberg approach is applied to study the superconducting instability, we define a Nambu spinor for the low energy electrons, i.e.:

$$\psi^\dagger_{\mathbf{k}\sigma} \equiv \left(c^\dagger_{\mathbf{k}\sigma},\ c_{-\mathbf{k}\bar{\sigma}}\right) \tag{4.4}$$

Here $\sigma = \uparrow, \downarrow$ labels electron spin state, and $\bar{\sigma}$ is the opposite spin state of σ. The electronic Green's function is a matrix in the Nambu space, defined as:

$$\hat{G}(\mathbf{k}, i\omega_n) \equiv \langle \psi\psi^\dagger \rangle = \begin{pmatrix} \langle cc^\dagger \rangle & \langle cc \rangle \\ \langle c^\dagger c^\dagger \rangle & \langle c^\dagger c \rangle \end{pmatrix} \tag{4.5}$$

For simplicity of writing, the spin and momentum indices are omitted. The off-diagonal entry is called the anomalous Green's function. It is directly proportional to the superconducting order parameter, and becomes non-zero in the superconducting phase. The diagonal entries are regular Green's functions for electrons/holes respectively. The effect of the bosonic coupling is incorporated in the electronic self-energy $\hat{\Sigma}$ via Dyson's equation, and the self-energy is calculated by the product of the full bosonic propagator and the full Green's function:

$$\begin{aligned} \hat{G}^{-1}(\mathbf{k}, i\omega_n) &= \hat{G}_0^{-1}(\mathbf{k}, i\omega_n) - \hat{\Sigma}(\mathbf{k}, i\omega_n) \\ \hat{\Sigma}(\mathbf{k}, i\omega_n) &= \frac{n_b \lambda^2}{\beta V} \sum_{\mathbf{p}, i\omega_m} \chi(\mathbf{k}-\mathbf{p}, i\omega_n - i\omega_m) \hat{G}(\mathbf{p}, i\omega_m) \end{aligned} \tag{4.6}$$

where $n_b = 3$ is the number of spin components, β the inverse temperature, and V the volume. The above equations are represented diagrammatically in Fig. 4.2.

To proceed, we parametrize the self-energy in the following form:

$$\hat{\Sigma}_k = (1 - Z_k) i\omega_n \tau_0 + \zeta_{\mathbf{k}} \tau_3 + \phi_k \tau_1 \tag{4.7}$$

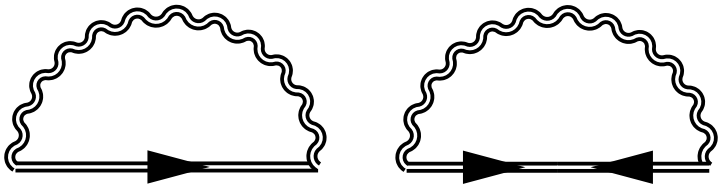

Figure 4.2: Feynman diagrams considered in the Eliashberg approach. Double curvy lines represent the full boson propagator dressed by electronic interactions, and double straight lines with one arrow/two arrows represent regular and anomalous part of the full electronic Green's function

where τ_i are Pauli matrices in the Nambu space, and $k \equiv (\mathbf{k}, i\omega_n)$ is the four-momentum representation. We introduced three parameters Z_k, $\zeta_{\mathbf{k}}$, and ϕ_k to represent the renormalizations to quasiparticle weight, energy dispersion, and superconducting gap respectively. From Dyson's equation Eq. 4.6, we obtain the full Green's function:

$$\hat{G}_k = -\frac{Z_k i\omega_n + \varepsilon_{\mathbf{k}}\tau_3 + \phi_k\tau_1}{Z_k^2\omega_n^2 + \varepsilon_{\mathbf{k}}^2 + \phi_k^2} \tag{4.8}$$

with renormalized band dispersion $\varepsilon_{\mathbf{k}} \to \varepsilon_{\mathbf{k}} + \zeta_{\mathbf{k}}$.

Substituting back into Eq. 4.6 and linearizing in ϕ_k, we find the self-consistent equations:

$$(1 - Z_k)i\omega_n = -\frac{n_b\lambda^2}{\beta V}\sum_p \chi(k-p)\frac{Z_p i\omega_m}{Z_p^2\omega_m^2 + \varepsilon_{\mathbf{p}}^2} \tag{4.9}$$

$$\phi_k = -\frac{n_b\lambda^2}{\beta V}\sum_p \chi(k-p)\frac{\phi_p}{Z_p^2\omega_m^2 + \varepsilon_{\mathbf{p}}^2} \tag{4.10}$$

Eq. 4.9 defines the coupled linearized Eliashberg equations for the spin-fermion model. By solving these equations, the quasiparticle renormalization, the superconducting gap structure, as well as the superconducting transition temperature can be obtained. While these equations are difficult to solve, in limiting cases, analytical solutions do exist based on physical assumptions. Below I look at two special cases where they can be solved analytically.

4.2.2 Weak coupling and away from magnetic QCP

We consider weak coupling ($\lambda \ll 1$) and away from quantum criticality ($r_0 \gg 0$). In this case, the dynamics of the spin fluctuations is negligible, and the renormalizations to the quasiparticle weight can be neglected. The "retardation effect", namely the frequency dependence of the gap function, can also be neglected. The problem reduces to superconductivity as a Fermi liquid instability in the presence of spin fluctuations.

Unlike the electron-phonon problem, the interaction mediated by spin fluctuations is repulsive. This is evidenced by the minus sign in Eq. 4.9. If the momentum dependence of the spin fluctuations was neglected, there is no solution to the Eliashberg equation, meaning that there is no superconductivity. This is in line with the BCS theory, where only attractive interaction (e.g., due to electron-phonon mechanism) can induce superconductivity.

However, the spin fluctuation is strongly momentum dependent, and peaked at the magnetic ordering wavevector $\mathbf{Q}$. As a result, only electronic states near a pair of hot spots are strongly coupled. By expanding near a pair of hot spots, we obtain:

$$\phi_{1,\mathbf{k}} \approx -\frac{n_b \lambda^2}{\beta V} \sum_{\mathbf{p}, i\omega_m} \frac{1}{r_0 + (\mathbf{k}-\mathbf{p})^2} \frac{\phi_{2,\mathbf{p}}}{\omega_m^2 + (\mathbf{v}_2 \cdot \mathbf{p})^2} \tag{4.11}$$

where we have defined $\phi_{\mathbf{k}} \equiv \phi_{1,\mathbf{k}}$, $\phi_{\mathbf{k}+\mathbf{Q}} \equiv \phi_{2,\mathbf{k}}$, and $\mathbf{k} \equiv \mathbf{k} - \mathbf{k}_{\text{h.s.}}$. $\mathbf{v}_i$ is the Fermi velocity at the ith hot spot. The equation can be solved by $\phi_{1,\mathbf{k}} = -\phi_{2,\mathbf{k}} \equiv \phi_0$, and:

$$1 \approx \frac{n_b \lambda^2}{\beta} \sum_{i\omega_m} \int \frac{\mathrm{d}p_\parallel \mathrm{d}p_\perp}{(2\pi)^2} \frac{1}{r_0 + p_\parallel^2 + p_\perp^2} \frac{1}{\omega_m^2 + v_F^2 p_\perp^2} \tag{4.12}$$

The dependence of $p_\perp$ in the boson propagator can be neglected compared to that in the fermion sector, provided that $r_0 \gg \omega_m / v_2$. As a result, the equation is satisfied below a critical temperature:

$$T_c \sim \Lambda_c \exp\left[-1/\left(\frac{\alpha n_b \lambda^2}{v_F \sqrt{r_0}}\right)\right] \tag{4.13}$$

where Λ_c is some upper energy cutoff associated with spin fluctuations, and α some numerical constant.

A naive extrapolation of the result to the magnetic QCP $r_0 \to 0$ gives $T_c \to \Lambda_c$, i.e., the critical temeperature is enhanced to Λ_c due to the presence of the magnetic

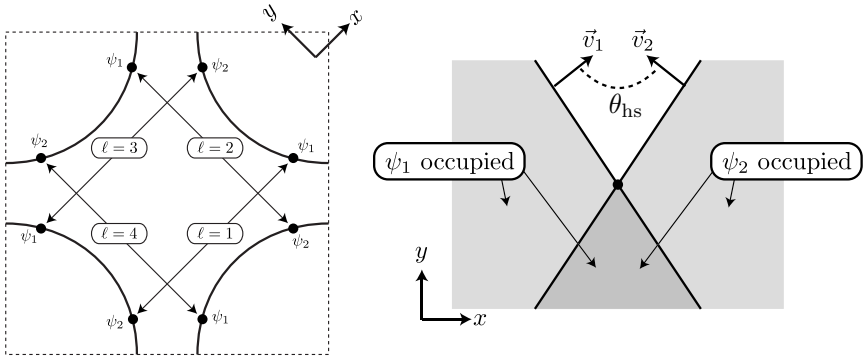

Figure 4.3: Left panel: Fermi surface and hot spot pairs. Right panel: properties of a pair of hot spots. Figures from Ref. [14].

QCP. As I will show in the next section, this is an overestimate of T_c, due to neglecting the renormalizations of the bosonic propagator and the quasiparticle weight, as well as omitting the frequency dependence of the superconducting gap function.

4.2.3 Near the magnetic QCP: the importance of hot spots

This section is written based on the appendix to my paper Ref. [94].

Based on the weak coupling analysis described above, the strong momentum dependence of the spin fluctuation propagator is necessary to obtain a finite T_c. This is also true for near the QCP, as the general structure of the Eliashberg equations remain unchanged. Therefore, we still work with the hot spot approximation. In this approximation, the electronic band dispersions are linearized in the vicinities of the hot spots, $\varepsilon_{i\mathbf{k}} \approx \mathbf{v}_i \cdot (\mathbf{k} - \mathbf{k}_{\rm hs})$. A pair of hot spots are characterized by their respective Fermi velocities $\mathbf{v}_i$ and the relative angle $\theta_{\rm hs}$. This is illustrated in Fig. 4.3. Note that the angle is always defined such that $\sin\theta_{\rm hs} > 0$.

The renormalized spin fluctuation propagator is computed within one-loop approximation:

$$\chi^{-1}(\mathbf{q}, i\Omega_n) = r_0 + \mathbf{q}^2 + \frac{\Omega_n^2}{v_s^2} + \frac{|\Omega_n|}{\gamma} \tag{4.14}$$

The Landau damping coefficient is given by:

$$\gamma = \frac{\pi v_F^2 \sin\theta_{\rm hs}}{\lambda^2 N} \tag{4.15}$$

Here, λ is the Yukawa coupling constant described in Eq. 4.3, and N is the number of hot spots pairs. At low energies, the spin fluctuation dynamics will be governed by Landau damping, rather than the original ballistic dynamics. For simplicity, we will neglect the ballistic dynamics in later calculations.

To proceed, we ignore the momentum dependence of the quasiparticle weight Z and of the gap ϕ. However, the frequency dependence needs to be included. Following the arguments given in the previous section, we only include the variation of the bosonic propagator with respect to the momentum parallel to the Fermi surface, $\chi(\mathbf{q}, i\Omega_n) \approx \chi(q_\parallel, i\Omega_n)$. Using these approximations, one can then perform the integration over momentum in the previous expressions by changing coordinates to $\left(p_\parallel, p_\perp\right)$, to obtain:

$$Z(\omega_n) = 1 + \frac{n_b \lambda^2 T}{4 v_F} \sum_{\omega_m} V_{\text{pair}}\left(\omega_n - \omega_m\right) \frac{\text{sign}(\omega_m)}{\omega_n} \tag{4.16}$$

$$\phi(\omega_n) = \frac{n_b \lambda^2 T}{4 v_F} \sum_{\omega_m} V_{\text{pair}}\left(\omega_n - \omega_m\right) \frac{\phi(\omega_m)}{Z(\omega_m)|\omega_m|} \tag{4.17}$$

To write these expressions, we note that $Z_1 = Z_2$, since the Fermi velocities are the same at both points of the hot-spot pair, and $\phi_1 = -\phi_2$ is the only possible solution to the gap equations. The pairing interaction is given by:

$$V_{\text{pair}}\left(\Omega_n\right) = \int_{-\frac{p_0}{2}}^{\frac{p_0}{2}} \frac{\mathrm{d}p_\parallel}{\pi} \frac{1}{r_0 + p_\parallel^2 + |\Omega_n|/\gamma} \tag{4.18}$$

where $p_0 \sim \mathcal{O}(1)$ is an upper momentum cutoff related to the size of the Fermi surface in the Brillouin zone. This momentum scale is to be compared to the typical "momentum width" of the hot spots, $\delta p_{\text{hs}} = \sqrt{2\pi T_c/\gamma}$, determined by comparing the frequency and momentum dependent terms in Eq. 4.14 for the energy scale $\Omega_1 = 2\pi T_c$.

In the hot-spots Eliashberg approximation, $p_0 \gg \delta p_{\text{hs}}$, and we can replace $p_0 \to \infty$ in the previous expression, yielding:

$$V_{\text{pair}}\left(\Omega_n\right) = \sqrt{\frac{1}{r_0 + |\Omega_n|/\gamma}} \tag{4.19}$$

Therefore, the Eliashberg equations become:

$$Z(\omega_n) = 1 + \frac{1}{2\pi}\sqrt{\frac{\Lambda_{\rm QCP}}{T}}\sum_{\omega_m}\frac{1}{\sqrt{|n-m|+\frac{r_0\gamma}{2\pi T}}}\frac{\mathrm{sign}(\omega_m)}{n+\frac{1}{2}} \tag{4.20}$$

$$\phi(\omega_n) = \frac{1}{2\pi}\sqrt{\frac{\Lambda_{\rm QCP}}{T}}\sum_{\omega_m}\frac{1}{\sqrt{|n-m|+\frac{r_0\gamma}{2\pi T}}}\frac{\phi(\omega_m)}{Z(\omega_m)|m+\frac{1}{2}|} \tag{4.21}$$

where we introduced the energy scale:

$$\Lambda_{\rm QCP} \equiv \left(\frac{n_b\lambda^2}{4v_F}\right)^2\frac{\gamma}{2\pi} = \frac{n_b^2\lambda^2\sin\theta_{\rm hs}}{32N} \tag{4.22}$$

The key point is that at the QCP, $r_0 = 0$, and the only energy scale in the problem is given by $\Lambda_{\rm QCP}$ (a similar behavior is found slightly away from the QCP, as long as $r_0 \ll 2\pi T_c/\gamma$). Therefore, the superconducting transition temperature at the QCP is set by the only energy scale in the problem, i.e.,

$$T_c = \alpha\Lambda_{\rm QCP} = \frac{\alpha n_b^2}{32N}\lambda^2\sin\theta_{\rm hs} \tag{4.23}$$

where α is a constant number. Notice that the upper energy cutoff Λ_c introduced in Eq. 4.13 does not appear in this equation, unlike the weak coupling scenario discussed previously. This is because the large frequency spin fluctuations are strongly damped, and therefore T_c is not linearly dependent on Λ_c.

According to our numerical solution of the Eliashberg equations, we find $\alpha \approx 0.56$. Note that, when $r_0 = 0$, the term $m = n$ in the sum that appears in the determination of $Z(\omega_n)$ is exactly canceled by the term $m = n$ in the sum that appears in the determination of $\phi(\omega_n)$. This is easily seen by defining the pairing gap $\Delta \equiv \phi/Z$, and separating out the $m = n$ term from Eq. 4.16:

$$\left[Z(\omega_n) - \frac{1}{2\pi}\sqrt{\frac{\Lambda_{\rm QCP}}{T}}\sqrt{\frac{2\pi T}{r_0\gamma}}\frac{1}{|n+\frac{1}{2}|}\right] = 1 + \frac{1}{2\pi}\sqrt{\frac{\Lambda_{\rm QCP}}{T}}\sum_{\omega_m\neq\omega_n}\frac{1}{\sqrt{|n-m|+\frac{r_0\gamma}{2\pi T}}}\frac{\mathrm{sign}(\omega_m)}{n+\frac{1}{2}} \tag{4.24}$$

$$\Delta(\omega_n)\left[Z(\omega_n) - \frac{1}{2\pi}\sqrt{\frac{\Lambda_{\rm QCP}}{T}}\sqrt{\frac{2\pi T}{r_0\gamma}}\frac{1}{|n+\frac{1}{2}|}\right] = \frac{1}{2\pi}\sqrt{\frac{\Lambda_{\rm QCP}}{T}}\sum_{\omega_m\neq\omega_n}\frac{1}{\sqrt{|n-m|+\frac{r_0\gamma}{2\pi T}}}\frac{\Delta(\omega_m)}{|m+\frac{1}{2}|} \tag{4.25}$$

Therefore the $m = n$ term does not enter into the linearized gap equation, and there is a finite superconducting transition temperature in the limit $r_0 \to 0$.

Eq. 4.23 gives the functional dependence of the superconducting transition temperature at a magnetic QCP based on the hot spot Eliashberg approximation. It is proportional to the square of the spin-fermion coupling vertex λ, and inversely proportional to the number of hot spot pairs. More interestingly, T_c does not depend on the Fermi velocity at the hot spots, but has a strong dependence on the relative angle $\theta_{\rm hs}$. A qualitative argument is presented as follows: for $\theta_{\rm hs} \to 0$, the Fermi surfaces at a pair of hot spots are nested. As a result, the spin fluctuations are maximally Landau damped, as shown in Eq. 4.15. The damped spin fluctuations are less efficient to drive a superconducting instability.

Failure of hot spots approximation

In the text before Eq. 4.19, we give a criterion for the failure of the hot spot approximation, namely, when the size of a hot spot extends to the size of the Fermi surface. It is nonetheless useful to still work with the hot spot approximation, to see how T_c evolves. This brief note will become useful later when I discuss the numerical results.

In this limit, the pairing interaction becomes:

$$V_{\rm pair}\left(\Omega_n\right) = \frac{p_0/\pi}{r_0 + |\Omega_n|/\gamma} \tag{4.26}$$

At the QCP, $r_0 = 0$, there is still only one energy scale in the Eliashberg equations, now set by:

$$\tilde{\Lambda}_{\rm QCP} \equiv \frac{p_0}{\pi}\left(\frac{n_b\lambda^2}{4v_F}\right)\frac{\gamma}{2\pi} = \frac{n_b p_0 v_F \sin\theta_{\rm hs}}{8\pi N} \tag{4.27}$$

The Eliashberg equations become:

$$Z(\omega_n) = 1 + \frac{1}{2\pi}\left(\frac{\tilde{\Lambda}_{\rm QCP}}{T}\right)\sum_{\omega_m}\frac{1}{|n-m| + \frac{r_0\gamma}{2\pi T}}\,\frac{\mathrm{sign}(\omega_m)}{n+\frac{1}{2}} \tag{4.28}$$

$$\phi(\omega_n) = \frac{1}{2\pi}\left(\frac{\tilde{\Lambda}_{\rm QCP}}{T}\right)\sum_{\omega_m}\frac{1}{|n-m| + \frac{r_0\gamma}{2\pi T}}\,\frac{\phi(\omega_m)}{Z(\omega_m)|m+\frac{1}{2}|} \tag{4.29}$$

The superconducting transition temperature T_c becomes:

$$T_c = \tilde{\alpha}\tilde{\Lambda}_{\rm QCP} = \frac{\tilde{\alpha} n_b p_0 v_F}{8\pi N}\sin\theta_{\rm hs} \tag{4.30}$$

T_c becomes independent of the Yukawa coupling, and may depend on additional properties of the Fermi surface, as indicated by the presence of the momentum scale p_0 in $\tilde{\Lambda}_{\rm QCP}$. Note that due to similar arguments described in Eq. 4.24, the $n = m$ term does not appear in the linearized gap equation.

I should re-emphasize that T_c obtained in Eq. 4.24 is still based on the hot spot Eliashberg approximation. This is *not* the correct form for the full Fermi surface considered in Fig. 4.3. For a detailed discussion on momentum-resolved Eliashberg approach, see Ref. [99].

Calculation of the pairing susceptibility

Here I show how the pairing susceptibility can be calculated in the hot spot Eliashberg approximation.

Focusing on a single pair of hot spots, depicted in Fig. 4.3. To compute the static pairing susceptibility in the sign-changing gap channel, we first introduce in the Hamiltonian the pairing field Δ:

$$\delta H = -2\Delta \sum_{\mathbf{k}} \left(\psi_{1\mathbf{k}\uparrow} \psi_{1-\mathbf{k}\downarrow} - \psi_{2\mathbf{k}\uparrow} \psi_{2-\mathbf{k}\downarrow} + h.c. \right) \tag{4.31}$$

where $\psi_{i=1,2}$ annihilates an electron at the hot spot i. Note that earlier in defining the spin-fermion model Eq. 4.2, I used c for electron annihilation. In Dyson's equation, this term can be incorporated in the self-energy, $\hat{\Sigma}_i \to \hat{\Sigma}_i - 2\Delta\tau_1$. Repeating the same steps as above, the only modification is in the gap equation:

$$\phi(\omega_n) = \frac{n_b \lambda^2 T}{4 v_F} \sum_{\omega_m} V_{\rm pair}\left(\omega_n - \omega_m\right) \frac{\phi(\omega_m)}{Z(\omega_m)|\omega_m|} + 2\Delta \tag{4.32}$$

We considered the linearized equation because we are interested only in the susceptibility of the disordered state, where $\phi = 0$. Defining $\eta(\omega_n) \equiv \partial\phi(\omega_n)/\partial\Delta$, we obtain a self-consistent equation for $\eta\left(\omega_n\right)$:

$$\eta(\omega_n) = \frac{n_b \lambda^2 T}{4 v_F} \sum_{\omega_m} V_{\rm pair}\left(\omega_n - \omega_m\right) \frac{\eta(\omega_m)}{Z(\omega_m)|\omega_m|} + 2 \tag{4.33}$$

$$\eta(\omega_n) = \frac{1}{2\pi} \sqrt{\frac{\Lambda_{\rm QCP}}{T}} \sum_{\omega_m} \frac{1}{\sqrt{|n-m|}} \frac{\eta(\omega_m)}{Z(\omega_m)|m+\frac{1}{2}|} + 2 \tag{4.34}$$

Now, the static pairing susceptibility is given by:

$$\chi_{\text{pair}} \equiv \chi(\mathbf{q} \to 0, i\Omega_n \to 0) = \partial_\Delta \sum_k 2\langle \psi_{1k\uparrow}\psi_{1-k\downarrow} - \psi_{2k\uparrow}\psi_{2-k\downarrow}\rangle \tag{4.35}$$

where $k = (\omega_n, \mathbf{k})$ and $\sum_k = T\sum_n \int \frac{d^2k}{(2\pi)^2}$. Because the mean value is precisely minus the anomalous part of the Green's function, $\phi_{i,k}$, given by Eq. 4.16, we obtain:

$$\chi_{\text{pair}} = 4T \sum_{\omega_n} \int \frac{d^2k}{(2\pi)^2} \frac{\eta(\omega_n)}{Z(\omega_n)^2\omega_n^2 + \varepsilon_{\mathbf{k}}^2} \tag{4.36}$$

Note that, for $\lambda = 0$ (non-interacting electrons), we have $Z(\omega_n) = 1,\ \eta(\omega_n) = 2$, and the equation above reduces to the well-known BCS expression

$$\chi_{\text{pair}} = 8T \sum_{\omega_n, \mathbf{k}} \frac{1}{\omega_n^2 + \varepsilon_{\mathbf{k}}^2} = 4 \sum_{i,k} G_i^{(0)}(k)\, G_i^{(0)}(-k) = 2N_f \ln \frac{\Lambda}{T} \tag{4.37}$$

where $N_f = 4\int \frac{\mathrm{d}^2\mathrm{k}}{(2\pi)^2}\delta(\varepsilon_{\mathbf{k}})$ is the total density of states at the Fermi level. The factor of 4 arises due to band and spin degeneracies.

For $\lambda \neq 0$, it is convenient once again to integrate along directions parallel and perpendicular to the Fermi surface, yielding:

$$\chi_{\text{pair}} = \frac{p_0}{2\pi^2 v_F} \sum_{\omega_n} \frac{\eta(\omega_n)}{Z(\omega_n)\left|n + \frac{1}{2}\right|} \tag{4.38}$$

where p_0 is the same quantity as defined in the previous section. Because the equations for $\eta(\omega_n)$ and $Z(\omega_n)$, Eqs. 4.33 and 4.20, depend only on $T/\Lambda_{\text{QCP}} \propto T/T_c$, it follows that the susceptibility is of the form $\chi_{\text{pair}}(T) = A_{\text{pair}} f_{\text{pair}}\left(\frac{T}{T_c}\right)$, where A_{pair} depends on the Fermi surface properties (as signaled by p_0 above), but $f_{\text{pair}}\left(\frac{T}{T_c}\right)$ is a universal function.

In computing χ_{pair} numerically, it is important to keep in mind that as higher temperatures are considered, the effect of the bandwidth becomes more important, as the bandwidth $8t$ provides a natural energy cutoff for the Matsubara sum. Note that this is not an issue for the computation of T_c, since $T_c \ll 8t$ always. Because $8t$ is a hard cutoff in real frequency space, to capture its effects in Matsubara frequency space, we follow Ref. [100] and introduce a soft cutoff:

$$\Upsilon(\omega_n) = \frac{1}{\exp\left[(\omega_n - 8t)/\omega_0\right] + 1} \tag{4.39}$$

This function appears not only in the Matsubara sum present in χ_{pair}, but also in the self-consistent equation for $\zeta(\omega_n)$ via:

$$\eta(\omega_n) = \frac{1}{2\pi}\sqrt{\frac{\Lambda_{\text{QCP}}}{T}}\sum_{\omega_m}\frac{\Upsilon(\omega_n)\Upsilon(\omega_m)}{\sqrt{|n-m|}}\frac{\eta(\omega_m)}{Z(\omega_m)|m+\frac{1}{2}|} + 2\Upsilon(\omega_n) \tag{4.40}$$

4.2.4 Charge density wave and SU(2) symmetry

Having understood how superconductivity can be studied using the hot spot Eliashberg approximation, here we show how charge density wave (CDW) can emerge in the spin-fermion model. Following Ref. [14, 101], under the hot spot approximation, the spin fermion model defined in Eqs. 4.1, 4.2, and 4.3 can be recasted onto an effective Lagrangian:

$$\mathcal{L} = \sum_{l=1...N}\left[\sum_{i=1,2}\frac{1}{2}\Psi_i^{\dagger l}(\partial_\tau - i\mathbf{v}_1^l\cdot\nabla)\sigma_0\tau_0\Psi_i^l + \frac{1}{2}\lambda\vec{\phi}\cdot(\Psi_1^{\dagger l}\vec{\sigma}\tau_0\Psi_2^l + h.c.)\right] \tag{4.41}$$

Here we introduce the four-component vector Ψ_i^l to represent the local Hilbert space at any hot spot, which is labeled by the index $l = 1...N$ for the pairs of hot spots and the index $i = 1, 2$ for either of the two hot spots within one pair. The notation is consistent with Fig. 4.3. The four component vector is defined in the spin$\times$Nambu space:

$$\Psi_i^l \equiv \begin{pmatrix}\psi_i^l \\ i\sigma_2\mathcal{C}\psi_i^l\end{pmatrix} \tag{4.42}$$

where the charge conjugation operator is: $\mathcal{C}\psi = \psi^\dagger$. The direct product matrices $\sigma_i\tau_j$ act on the vector Ψ field, where σ and τ are Pauli matrices acting on the spin and Nambu spaces respectively.

One immediately observes that the Lagrangian is invariant under the SU(2) transformations in the Nambu space, as the only matrix appearing in the Lagrangian is the identity matrix τ_0. Physically, this SU(2) symmetry is the particle-hole symmetry at each hot spot. As a result, the spin-singlet Cooper pairing operator maps onto a charge density wave operator via a particle-hole transformation $\psi_1 \to i\sigma_2\psi_1^\dagger$:

$$\psi_{1\uparrow}^1\psi_{1\downarrow}^3 - \psi_{1\downarrow}^1\psi_{1\uparrow}^3 \Rightarrow \psi_{1\downarrow}^{1\dagger}\psi_{1\downarrow}^3 + \psi_{1\uparrow}^{1\dagger}\psi_{1\uparrow}^3 \tag{4.43}$$

As consequence, the particle-hole symmetry means that the charge density wave with a wavevector $\mathbf{Q}_{13} \equiv (Q_0, Q_0)$ along the diagonal direction (right hand side of the above

equation, see also Fig. 4.3) is degenerate with superconductivity with a zero momentum (left hand side of the above equation). This gives a possible argument of why in some cuprate materials, charge density wave order is found near the superconducting phase.

Note that the SU(2) symmetry described above is an approximate symmetry based on the linearized band dispersion in the vicinity of a hot spot. In realistic materials, both band curvature and Fermi surface curvature will break this symmetry. The symmetry breaking always favors superconductivity over charge density wave, as the latter depends delicately on the details of the whole Fermi surface [101].

Additionally, various experiments [11, 102, 12, 103] have suggested that the charge density wave order is actually axial, described by a wavevector along the Cu-O-Cu bond direction, rather than checkerboard like (described by a wavevector along the diagonal direction). Therefore, the hot spot SU(2) symmetry is not directly applicable to the explanation in the experiments. Ref. [104] and [101] have given alternative arguments on how to achieve axial CDW orders.

4.2.5 Summary of results

To summarize, in this section, we discussed the spin-fermion model, and used the hot spot Eliashberg approximation to analyze the low energy superconducting properties. The main conclusions are the functional dependence of T_c on the hot spot parameters presented in Eq. 4.23 and Eq. 4.23.

Following Ref. [14], we showed that in the hot spot approximation, there is an emergent SU(2) symmetry, corresponding to the particle-hole transformation at each hot spot. Such a symmetry explains why charge density wave order and superconductivity can be nearly degenerate with each other. Both band curvature and Fermi surface curvature will break this symmetry, favoring superconductivity over charge density wave.

The above conclusions are reached based on the Eliashberg approach. As was discussed briefly at the beginning of this section, it is by no means obvious that the Eliashberg approach is valid. In the next chapter, I will discuss our work on numerical solutions of the spin-fermion model, and discuss the results compared to those predicted by the Eliashberg approximation.

4.3 Determinantal Quantum Monte Carlo and applications to the spin-fermion model

4.3.1 Introduction

Numerically, the spin-fermion model falls in the class of coupled boson-fermion systems, and can be studied using the Determinantal Quantum Monte Carlo (DQMC) technique introduced by Ref. [105]. The DQMC technique is an unbiased method to exactly solve the spin-fermion model, not constrained by the various approximation schemes used in theoretical calculations. DQMC achieves this goal by generating an ensemble of field configurations, whose probability distribution mimics that of the thermodynamic ensemble. The technique follows the Metropolis algorithm, which defines a transition probability for the successive generations of new field configurations in the ensemble. The transition probability is determined by the *detailed balance principle*, which says that in thermodynamic equilibrium, each elementary process is equilibrated with its reverse process. The details of the DQMC procedure are included in appendix A.

Although the DQMC technique is exact by nature, the accuracy of the numerical solutions will be limited by a number of factors, such as the truncation of the system size, discretization errors, and insufficient sampling (i.e., situations where the number of field configurations in the ensemble is sub-optimal). As described briefly in the appendix A, all of these can be alleviated to some extent. However, there is a more severe problem associated with DQMC simulations of the spin-fermion model, i.e., the fermion sign problem.

The sign problem describes the fact that in simulating fermionic systems using Monte Carlo method, due to the anti-commuting nature of fermionic wavefunctions, the transition probability is not necessarily positive. Therefore, in simulating the fermionic systems, one needs to keep track of the signs of the transition probability. While the sign problem is less severe at high temperatures, where electrons can be treated as semi-classical objects, it becomes important at low temperatures, where various electronic phases (such as superconductivity) appear. The computational error due to the sign problem scales exponentially as temperature goes down [106].

Although the sign problem is a generic problem in simulating fermionic systems, it is absent for certain class of models, in particular, Hamiltonians possessing Kramer's

symmetry[107]. The Kramers symmetry is an antiunitary symmetry A of the fermionic Hamiltonian H, such that $A^2 = -1,\ AHA^{-1} = H$. Some examples of such Hamiltonians include the negative-U Hubbard model and the positive-U Hubbard model on a bipartite lattice (i.e., half-filling).

The one-band spin-fermion model described in last section does *not* possess such a symmetry. However, a two-band variant where the spin fluctuation only couples electrons between different bands have such a symmetry, and therefore can be studied using the Monte Carlo procedure described above, free of the fermion sign problem. The proof is presented in appendix A. Below I will briefly describe the two-band spin-fermion model and the relevant system parameters for later numerical studies.

4.3.2 DQMC procedure for the two-band spin-fermion model

In DQMC, the two-band spin-fermion model is written in terms of an action:

$$S[\bar{\psi}, \psi; \vec{\phi}] = S_b + S_f + S_\lambda \tag{4.44}$$

$$S_b = \frac{1}{2}\int_{\tau,\mathbf{x}} \left[\frac{1}{v_s^2}\left(\partial_\tau \vec{\phi}\right)^2 + \left(\nabla\vec{\phi}\right)^2 + r\vec{\phi}^2 + \frac{u}{2}\left(\vec{\phi}^2\right)^2\right] \tag{4.45}$$

$$S_f = \int_{\tau,\mathbf{k}} \sum_{i=c,d}\sum_{\alpha=\uparrow\downarrow} \bar{\psi}_{i\mathbf{k}\alpha}\left(\partial_\tau + \varepsilon_{i\mathbf{k}} - \mu\right)\psi_{i\mathbf{k}\alpha} \tag{4.46}$$

$$S_\lambda = \lambda\int_{\tau,\mathbf{x}} \sum_{\alpha\beta} \vec{\phi}\cdot\left(\bar{\psi}_{c\alpha}\vec{\sigma}_{\alpha\beta}\psi_{d\beta} + h.c.\right) \tag{4.47}$$

Here the spin fluctuation $\vec{\phi}$ is described by the standard ϕ^4 action. r is the bare mass of spin fluctuations, and is a tunable parameter to probe magnetic quantum critical point. $\bar{\psi}_{i=c,d}$ and $\psi_{i=c,d}$ are Grassmann variables representing the two types of electron. $\vec{\sigma}$ are Pauli matrices in spin space.

In the DQMC procedure, the fermionic and bosonic degrees of freedom are placed on a 2+1 dimensional lattice, with $L \times L$ sites along the space directions, and N_τ sites along the imaginary time direction.

The fermionic degrees of freedom are integrated out (Gaussian) to achieve a purely bosonic partition function:

$$\mathcal{Z} \equiv \int \mathcal{D}[\bar{\psi}, \psi; \vec{\phi}]\exp(-S) = \int \mathcal{D}[\vec{\phi}]\det{}_{\vec{\phi}}\exp(-S_b) \tag{4.48}$$

The ensemble of $\{\vec{\phi}(\mathbf{x},\tau)\}$ is generated following the standard Monte Carlo procedure described in appendix A, with probability density proportional to $\det_{\vec{\phi}} \exp(-S_b)$. The low energy properties are determined from various correlation functions, the calculations of which are also presented in appendix A.

To reduce the computation time, we used XY spins (i.e., $\vec{\phi} \equiv (\phi_x, \phi_y)$) rather than Heisenberg spins (i.e., $\vec{\phi} \equiv (\phi_x, \phi_y, \phi_z)$). While this affects the quantitative results, the electronic properties remain qualitatively unchanged. Additionally, to minimize finite size effects, we follow Ref. [108, 92] to thread a magnetic flux quanta through the two dimensional plaquette. Such a flux quanta is small enough for the system sizes we have studied, and the physics remains unchanged. The details are presented in appendix A.

The system parameters include $\{v_s, r, u\}$ in the bosonic sector, and the spin-fermion interaction parameter λ. The fermionic sector is determined by the band dispersions. Additionally, there are also the inverse temperature β, and lattice parameters L, N_τ.

In later sections, unless specified otherwise, we use $v_s = 2$, $u = 1$, and vary r to locate the magnetic QCP. The time discretization is fixed at $\delta_\tau \equiv \beta/N_\tau = 0.1$.

4.3.3 Summary

The two band spin-fermion model was first proposed and studied by Ref. [91], and later by Ref. [109, 110, 92, 93]. In particular, Ref. [92, 93] give a thorough characterization of the phase diagram and the normal state electronic and magnetic properties.

In generalizing from one band to two band spin-fermion model, it is assumed that hot spots, rather than the whole Fermi surface, determines the low energy physics. Therefore, a pair of hot spots is split onto different electron bands. The hot spot properties are preserved while the rest of the Fermi surface is distorted freely. This generalization is motivated by the fact that spin fluctuations are strongly momentum-dependent, and couples much more strongly with hot spots than the rest of the Fermi surface. However, despite intense research activity in this front, the extent to which hot spot properties govern the low energy physics remains a hotly debated issue [97, 14, 98, 111].

In later sections, I will present two of our numerical investigations of the two-band spin-fermion model, in regards to superconductivity and charge density wave physics in proximity to a magnetic quantum critical point.

By comparing our numerical results with insights from the hot spot Eliashberg approach, I will address several questions relevant to the low energy physics in proximity to the magnetic QCP. In particular, what is the low-energy electronic phase diagram from the numerical solutions of the two-band spin-fermion model? Is the hot spot approximation justified? Is Eliashberg approach valid? How does the approximate SU(2) symmetry affect the interplay between superconductivity and charge density wave physics? What does T_c depend upon?

4.4 Superconductivity mediated by quantum critical antiferromagnetic fluctuations: the rise and fall of hot spots

This section is written based on my paper Ref. [94].

4.4.1 Introduction

In the hot spot Eliashberg approach, the superconducting transition temperature derived in Eq. 4.23 is:

$$T_c = \frac{\alpha n_b^2}{32N}\lambda^2 \sin\theta_{\rm hs};\ \alpha = 0.56 \tag{4.49}$$

The static pairing susceptibility in the disordered phase is also shown to possess a functional form:

$$\chi_{\rm pair} = A_{\rm pair} f_{\rm pair}(\frac{T}{T_c}) \tag{4.50}$$

The functional dependence on the relative angle between Fermi velocities at a pair of hot spots is unique and quite interesting. If this functional dependence is also shown in the numerical solutions to the two-band spin-fermion model, it will be a convincing evidence for the validity of the hot spot Eliashberg approach.

4.4.2 Electronic band dispersion

To achieve this goal, we study a family of band dispersions that interpolate between closed nearly-nested Fermi pockets to open Fermi surfaces, passing through a van Hove singularity, where the density of states is strongly peaked. This non-trivial dependence

of the density of states on the band dispersion allows us to separate phenomena associated with the Fermi surface as a whole and with the hot spots only.

The fermionic Hamiltonian is:

$$\mathcal{H}_0 = \sum_{\mathbf{k}\alpha} \varepsilon_{c,\mathbf{k}} c^\dagger_{\mathbf{k}\alpha} c_{\mathbf{k}\alpha} + \sum_{\mathbf{k},\alpha} \varepsilon_{d,\mathbf{k}} d^\dagger_{\mathbf{k}\alpha} d_{\mathbf{k}\alpha} \,. \tag{4.51}$$

Here, the operator $c^\dagger_{\mathbf{k}\alpha}$ creates an electron with momentum $\mathbf{k}$ and spin α at band c. The centers of the two bands are displaced from each other by the AFM ordering vector $\mathbf{Q} = (\pi, \pi)$, and the dispersions are given by

$$\begin{aligned} \varepsilon_{c,\mathbf{k}} &= \mu - 2(t+\delta)\cos k_x - 2(t-\delta)\cos k_y \\ \varepsilon_{d,\mathbf{k}+\mathbf{Q}} &= -\mu + 2(t-\delta)\cos k_x + 2(t+\delta)\cos k_y \,, \end{aligned} \tag{4.52}$$

where t is the hopping parameter, μ is the chemical potential, and momentum is measured in units of inverse lattice constant $1/a$. Hereafter, we set $\mu = t$. By changing the parameter δ, the band dispersions interpolate between two closed nearly-nested Fermi pockets ($\delta < t/4$) and two open Fermi surfaces ($\delta > t/4$), see Fig. 4.4. For $\delta = t/4$, the band dispersion has a saddle point at the Fermi level, implying the existence of a van Hove singularity, which is characterized by a diverging density of states, N_f.

For the specific band dispersions of our model, because the hot spots are always along the diagonal $|k_x| = |k_y|$, we have $|\mathbf{v}_{F,i}| = v_F$ for all hot spots, with:

$$v_F = 2t\sqrt{2\left[1 - \left(\frac{\mu}{4t}\right)^2\right]\left[\left(\frac{\delta}{t}\right)^2 + 1\right]} \tag{4.53}$$

The relative angle θ_{hs} between the Fermi velocities of a pair of hot spots is calculated to be:

$$\sin\theta_{\mathrm{hs}} = \frac{2\,(\delta/t)}{1 + (\delta/t)^2} \tag{4.54}$$

Below I describe our DQMC procedure in determining the magnetic QCP, as well as measurement of superconducting properties. The results are presented for $L = 12$, $\lambda^2 = 8t$, and $\delta = 0.6t$. However, the statements do not depend on the specific system parameters. Later I will present our numerical results and comparisons with hot spot Eliashberg calculations.

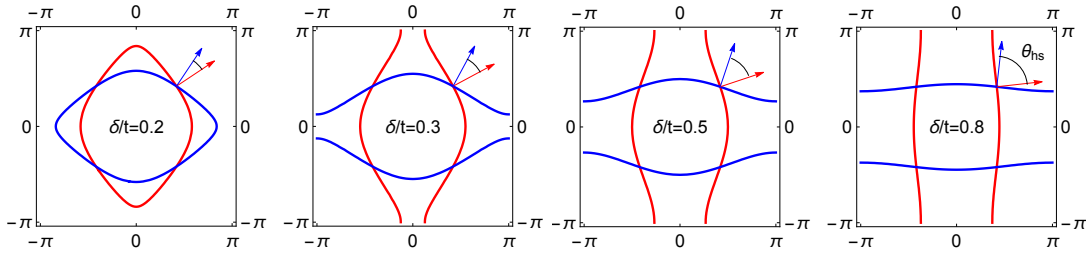

Figure 4.4: Fermi surfaces corresponding to the two bands (red and blue curves) in the first Brillouin zone, for different values of δ/t. One of the bands (blue) is displaced by the AFM wave-vector $\mathbf{Q} = (\pi, \pi)$, which makes both Fermi surfaces appear concentric. In this representation, a pair of hot spots, defined by $\varepsilon_{c,\mathbf{k}_{\rm hs}} = \varepsilon_{d,\mathbf{k}_{\rm hs}+\mathbf{Q}} = 0$, correspond to the points at which the two Fermi surfaces overlap. For the system parameters used here, the hot spots are always along the diagonals of the Brillouin zone. By changing the parameter δ/t, the system interpolates between closed nearly-nested Fermi surfaces ($\delta/t < 1/4$) and open Fermi surfaces ($\delta/t > 1/4$), crossing a van Hove singularity at $\delta/t = 1/4$. The angle $\theta_{\rm hs}$ between the Fermi velocities of a pair of hot spots (red and blue arrows) increases as function of δ/t (note that one of the Fermi velocities has been multiplied by -1 for clarity purposes). From Ref. [94].

4.4.3 DQMC procedure

Locating the magnetic QCP

For a finite temperature $1/\beta$, we tune the bare boson mass r to locate the magnetic phase transition $r_c(\beta)$. We then extrapolate to zero temperature $\beta \to \infty$ to locate the magnetic QCP.

We first define the uniform magnetization for a given field configuration $\{\vec{\phi}(\mathbf{x}, \tau)\}$:

$$\bar{\mathbf{M}} \equiv \frac{1}{\beta L^2} \int_0^\beta \mathrm{d}\tau \sum_{\mathbf{x}} \vec{\phi}(\mathbf{x}, \tau) \tag{4.55}$$

To obtain a good estimate of r_c, we extract from the QMC simulations both the Binder cumulant,

$$\mathcal{B} = 1 - \frac{\langle (\bar{\mathbf{M}}^2)^2 \rangle}{2\langle \bar{\mathbf{M}}^2 \rangle^2} \tag{4.56}$$

and the static spin susceptibility,

$$\chi_M \equiv \frac{1}{\beta L^2} \langle \sum_{\mathbf{x},\tau} \sum_{\mathbf{x}',\tau'} \vec{\phi}(\mathbf{x}, \tau) \cdot \vec{\phi}(\mathbf{x}', \tau') \rangle = \beta L^2 \langle \bar{\mathbf{M}}^2 \rangle \tag{4.57}$$

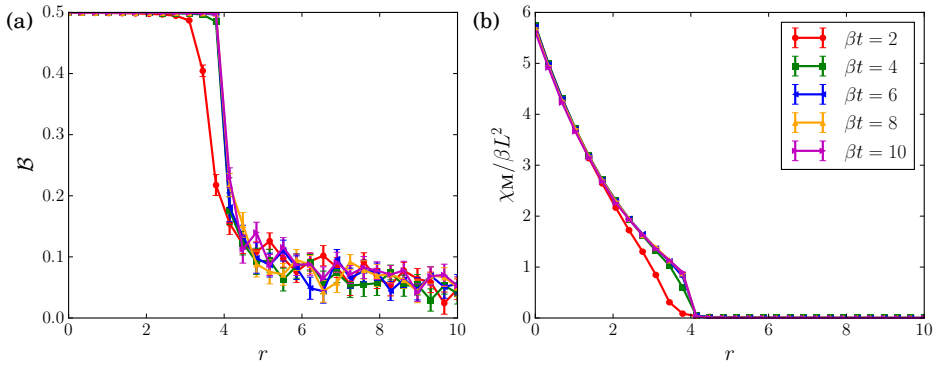

Figure 4.5: Binder cumulant $\mathcal{B}$ (left) and static spin susceptibility χ_M (right) as a function of r for various temperatures. The inverse temperature β is in units of $1/t$. From Ref. [94].

Here, $\langle \cdots \rangle$ denotes thermal averaging. For XY spins on a two dimensional lattice, the magnetic phase transition is of Berezinskii-Kosterlitz-Thoughless (BKT) type. Deep in the ordered phase, $\mathcal{B} = \frac{1}{2}$, and $\mathcal{B} = 0$ in the disordered phase. Similarly, in the ordered phase, χ_M scales with $\beta L^{2-\eta}$, where η changes continuously as function of r and T, approaching $\eta = 0$ in the ordered phase at zero temperature. Therefore, at any finite temperature, a rough estimate for the AFM transition is given by the value of r in which $\chi_M/\left(\beta L^2\right)$ shows a kink and $\mathcal{B}$ changes sharply from 0 to 1/2. In Fig. 4.5, we show the behavior of these two quantities. On the scale shown in this figure, both $\mathcal{B}$ and $\chi_M/\left(\beta L^2\right)$ are nearly temperature independent at low temperatures (but still above T_c), therefore providing an estimate for r_c.

Next, to improve our estimate of r_c, we compute the r dependence of the mass of the bosonic propagator at low temperatures, $\tilde{r} \equiv \chi_M^{-1}\left(\mathbf{q} = 0, i\Omega_n = 0\right)$, as shown in Fig. 4.6(a). The estimated r_c corresponds to the r value that has the smallest $\tilde{r}$, before however it reaches zero, since we want to study the system in the non-magnetically ordered state.

In the same figure we also present the frequency and momentum dependencies of $\chi_M^{-1}\left(\mathbf{q}, i\Omega_n\right)$. $\chi_M^{-1}(\mathbf{q} = 0, i\Omega_n)$ shows a rather linear dependence on the Matsubara frequency, indicating the presence of Landau damping, which in turn plays a key role in the hot-spots Eliashberg approximation, see Eq. 4.14. Similarly, $\chi_M^{-1}(\mathbf{q}, i\Omega_n = 0)$ is

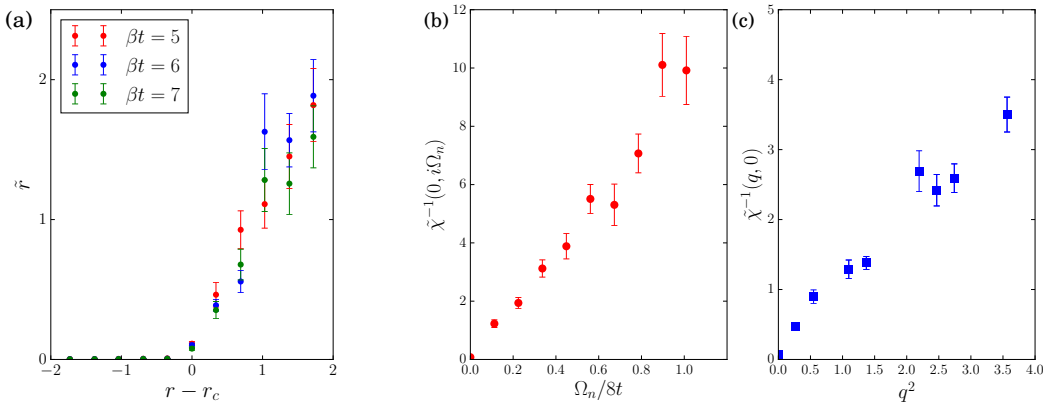

Figure 4.6: Panel (a) shows the renormalized mass term of the magnetic propagator, $\tilde{r}$, as function of r_c. The set of parameters used here is $\left(\delta/t,\ L,\ \lambda^2/t\right) = (0.6,\ 12,\ 8)$. The inverse renormalized magnetic propagator $\tilde{\chi}^{-1}(\mathbf{q}, i\Omega_n)$ at $r = r_c$ is plotted as function of Ω_n for $\mathbf{q} = 0$ (b) and as function of q for $\Omega_n = 0$ (c). In (b) and (c), the inverse temperature is $\beta = 7/t$. From Ref. [94].

consistent with a q^2 behavior for small momentum.

Pairing susceptibility and superfluid density

The static pairing susceptibility is defined as:

$$\chi^{(a)}_{\text{pair}} \equiv \frac{1}{\beta L^2} \sum_{\mathbf{r},\mathbf{r}'} \int_{\tau,\tau'} \langle \Gamma_a(\mathbf{r},\tau) \Gamma^\dagger_a(\mathbf{r}',\tau') \rangle \tag{4.58}$$

where

$$\Gamma_a(\mathbf{r},\tau) \equiv i\sigma^y_{\alpha\beta} \left[c_\alpha(\mathbf{r},\tau) c_\beta(\mathbf{r},\tau) + (-1)^a d_\alpha(\mathbf{r},\tau) d_\beta(\mathbf{r},\tau) \right] \tag{4.59}$$

is the pairing field associated with the sign-changing gap function ($a = 1$) or to the sign-preserving gap function ($a = 2$). σ_y is the Pauli matrix in spin space. In Fig. 4.7, we plot both pairing susceptibilities, in units of the non-interacting susceptibility $\chi_{\text{pair},0}$, as function of r and as function of temperature. Compared with Fig. 4.5, it is clear that while $\chi^{(1)}_{\text{pair}}/\chi_{\text{pair},0}$ is strongly peaked at $r = r_c$, $\chi^{(2)}_{\text{pair}}/\chi_{\text{pair},0}$ is always smaller than 1, implying that there is no enhancement in the sign-preserving channel.

Because the system is two-dimensional, the superconducting phase transition is also of the BKT type. Therefore, to determine T_c, we search for the temperature where the

BKT condition is satisfied:

$$\rho_s(T_c) = \frac{2}{\pi} T_c$$

where ρ_s is the superfluid density.

As explained in Ref. [92], the latter can be extracted from our QMC simulations via the current-current correlation function Λ_{ij} according to $\rho_s \equiv \lim_{L\to\infty} \rho_s(L)$, with:

$$\rho_s(L) = \frac{1}{8}\langle \Lambda_{xx}(q_x = \frac{2\pi}{L}, q_y = 0, i\Omega_n = 0) + \Lambda_{yy}(q_x = 0, q_y = \frac{2\pi}{L}, i\Omega_n = 0)\rangle \quad (4.60)$$

$$- \frac{1}{8}\langle \Lambda_{xx}(q_x = 0, q_y = \frac{2\pi}{L}, i\Omega_n = 0) + \Lambda_{yy}(q_x = \frac{2\pi}{L}, q_y = 0, i\Omega_n = 0)\rangle \quad (4.61)$$

where

$$\Lambda_{ij}(\mathbf{r}, \tau) \equiv \frac{1}{\beta L^2}\langle \int d\tau_1 \sum_{\mathbf{r}_1} j_i(\mathbf{r} + \mathbf{r_1}, \tau + \tau_1) j_j(\mathbf{r}_1, \tau_1)\rangle \quad (4.62)$$

and j_i is the standard current operator. Note that the model studied here is symmetric under the combination of a $\pi/2$ rotation, a particle-hole transformation, and the exchange of the two bands, implying $\Lambda_{xx}(\mathbf{r}, \tau) = \Lambda_{yy}(\tilde{\mathbf{r}}, \tau)$, where $\mathbf{r}$ and $\tilde{\mathbf{r}}$ are related by a $\pi/2$ rotation. Fig. 4.8 shows ρ_s for various system sizes for the band dispersion $\delta/t = 0.6$ and the interaction parameter $\lambda^2 = 8t$. The estimated transition temperature $T_c(L)$ for each system of size L is determined as the intersection between the interpolated curve of $\rho_s(L, T)$ and $\frac{2}{\pi}T$. The error bars in ρ_s arising from the QMC sampling are used to estimate the error bars of T_c in the following way: besides the interpolation curve passing through the average values of ρ_s, we also determine two additional interpolation curves passing through the top and the bottom of each error bar related to ρ_s. The error bars in T_c are estimated by determining when these two additional curves cross $\frac{2}{\pi}T$.

Thermodynamic limit of the BKT transition temperature

To estimate the thermodynamic value of the BKT transition, we first plot the extracted $T_c(L)$ as function of $1/L$ in Fig. 4.9a. For most of the values of δ/t that we studied specifically, $\delta/t = 0.2$, 0.3, 0.4, 0.5, 0.7 we found a near saturation of $T_c(L)$ for the two largest system sizes studied, i.e. $L = 12$ and $L = 14$ for $0.4 \leq \delta/t \leq 0.8$, and $L = 10$ and $L = 12$ for $0.2 \leq \delta/t \leq 0.3$. We verified that the reason for this behavior is that the superfluid density curves for the two largest system sizes agree within statistical

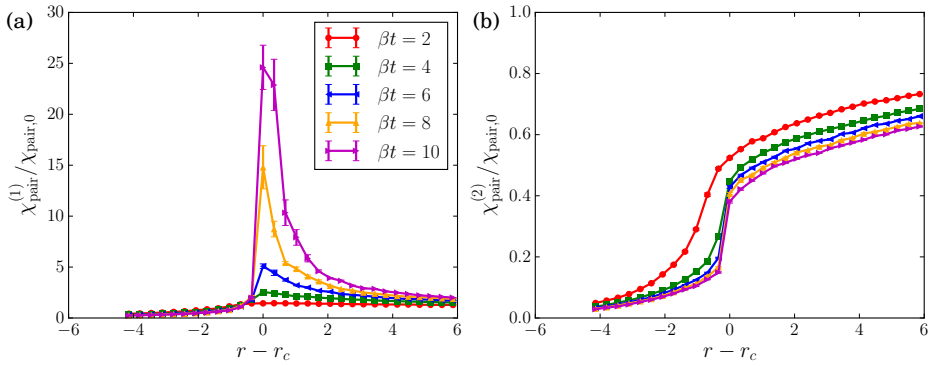

Figure 4.7: Static pairing susceptibility $\chi^{(a)}_{\rm pair}$ in the sign-changing gap channel ($a = 1$, panel a) and in the in the sign-preserving gap channel ($a = 2$, panel b) as function of the distance to the QCP at $r = r_c$. The inverse temperature β is in units of $1/t$ and the susceptibilities are normalized by the non-interacting susceptibility $\chi_{\rm pair,0}$ obtained by setting $\lambda = 0$. From Ref. [94].

error bars near the BKT transition. We illustrate this behavior for the case $\delta/t = 0.4$ in Fig. 4.9b. Therefore, for these band dispersions, we estimate the thermodynamic value for the transition temperature to be given by $T_c\,(L_{\rm max})$.

For the band dispersion with $\delta/t = 0.6$, even though T_c nearly saturates for the two largest system sizes, the corresponding superfluid density curves are not on top of each other within the QMC statistical error bars. This is also the case for the band dispersion with $\delta/t = 0.8$, as shown in Fig. 4.9c. Moreover, for this band dispersion, T_c does not really seem to saturate for the two largest system sizes, as shown in Fig. 4.9a. For these two systems, $T_c\,(L_{\rm max})$ should therefore be understood as an upper bound value for the thermodynamic value of T_c. In these cases, we can also estimate the lower bound value by the condition that the $\rho_s(T, L_{\rm max})$ curve becomes larger than $\rho_s(T, L)$ for one of the smaller system sizes studied (in our case, $L = 12$). Such a criterion is based on the fact that, in the disordered phase, finite-size effects generally make $\rho_s(T, L)$ larger for smaller system sizes.

4.4.4 T_c dependence on hot spot properties

In Fig. 4.10, we show the behavior of $T_c\,(L)$ at the AFM-QCP as function of the parameter δ/t introduced in Eq. 4.52 for a moderately strong interaction parameter $\lambda^2 = 8t$.

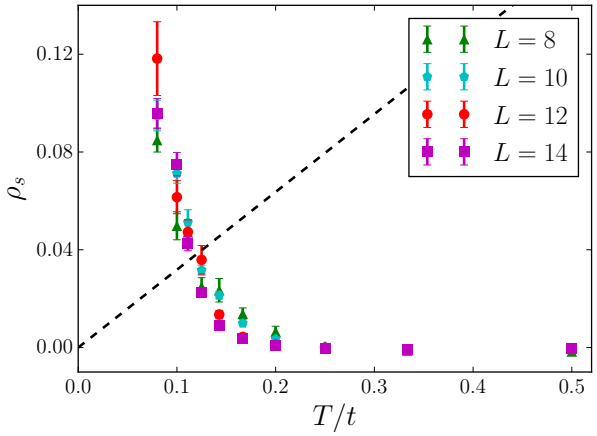

Figure 4.8: Superfluid density $\rho_s(L,T)$ as function of temperature T for the band dispersion $\delta/t = 0.6$ and coupling constant $\lambda^2 = 8t$ for various system sizes L. The BKT transition temperature for each system size is determined by the condition $\rho_s(L,T_c) = \frac{2}{\pi}T_c$. From Ref. [94].

Fig. 4.10 reveals that T_c is not sensitive to the non-interacting density of states N_f, which diverges at the van Hove singularity at $\delta/t = 0.25$, as shown in the same figure.Instead, we find that T_c increases linearly with $\sin\theta_{\rm hs}$, where $\theta_{\rm hs}$ is the angle between the non-interacting Fermi velocities of a hot-spot pair (see Fig. 4.4). This is consistent with the qualitative predictions from the hot spot Eliashberg approach. If we plug in the bare value of the interaction parameter into Eq. 4.49, we obtain $T_c^{(\rm hs)}/t = 0.14\sin\theta_{\rm hs}$, which is very close to the linear fitting in Fig. 4.10, $T_c^{(\rm hs)}/t = 0.13\sin\theta_{\rm hs}$. However, in comparing $T_c^{(\rm hs)}$ with our QMC results, it is important to recognize that the BKT physics is absent in the hot-spots Eliashberg approximation. Of course, if the phase fluctuations responsible for the suppression of $T_c^{(\rm hs)}$ are only weakly sensitive on the band structure parameters [112], then the Eliashberg transition temperature $T_c^{(\rm hs)}$ and the BKT transition temperature T_c should be simply related by a constant α, $T_c = \alpha T_c^{(\rm hs)}$. The fact that T_c scales linearly with $\sin\theta_{\rm hs}$ in our QMC simulations suggests that this is indeed the case.

To further investigate the SC properties of the system, in Fig. 4.11 we plot the temperature-dependent inverse pairing susceptibility $\chi^{-1}_{\rm pair}(T)$ for all band dispersions at their respective QCPs. We find that, for a rather wide temperature range, the

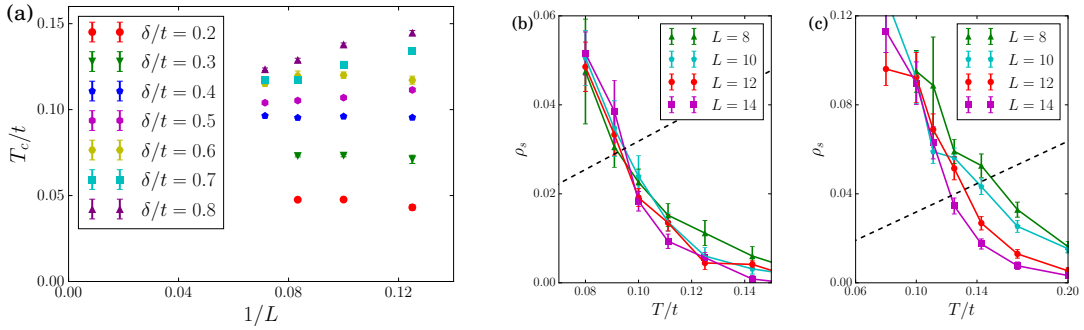

Figure 4.9: (a) The QMC extracted $T_c(L)$ as function of the inverse system size $1/L$ for all band dispersion parameters δ/t. Interpolated $\rho_S(T)$ curve for $\delta/t = 0.4$ (b) and for $\delta/t = 0.8$ (c). From Ref. [94].

normalized susceptibilities $\chi_{\text{pair}}^{-1}(T)/\chi_{\text{pair}}^{-1}(3T_c)$ plotted as function of T/T_c collapse onto a single curve, for all values of δ/t and of L. As a result, it follows that the pairing susceptibility must be of the form presented earlier in Eq. 4.50.

While the constant A_{pair}, which determines the overall amplitude of the SC fluctuations, depends weakly on δ/t (see Fig. 4.11), the function $f_{\text{pair}}(T/T_c)$, which determines the temperature dependence of the SC fluctuations, is universal and independent on the band dispersion. Therefore, these results imply that for a wide range of temperatures, the SC fluctuation spectrum is determined by the same energy scale that determines T_c which, according to the analysis in Fig. 4.10, is related to the hot-spots properties.

We can also compute the pairing susceptibility $\chi_{\text{pair}}^{(\text{hs})}(T)$ within the hot-spots Eliashberg approximation. The detailed calculation was presented in the previous sections. At the QCP, we obtain an expression of the form of Eq. 4.50, with the universal function $f_{\text{pair}}^{(\text{hs})}(T/T_c)$ plotted together with the collapsed QMC points in Fig. 4.11. The overall agreement between the two curves is evident and, surprisingly, holds over a rather wide temperature range. This confirms our previous conclusion that $f_{\text{pair}}(x)$ arises from hot-spots properties. The fact that the analytical function $f_{\text{pair}}^{(\text{hs})}(T/T_c)$, which is insensitive to BKT physics, captures well the behavior of the QMC-derived function $f_{\text{pair}}(T/T_c)$, suggests that vortex-antivortex fluctuations characteristic of the BKT transition do not play a major role in our QMC simulations. Indeed, for all system sizes studied, $\chi_{\text{pair}}(T)$ does not show any indication of an exponential temperature dependence near T_c.

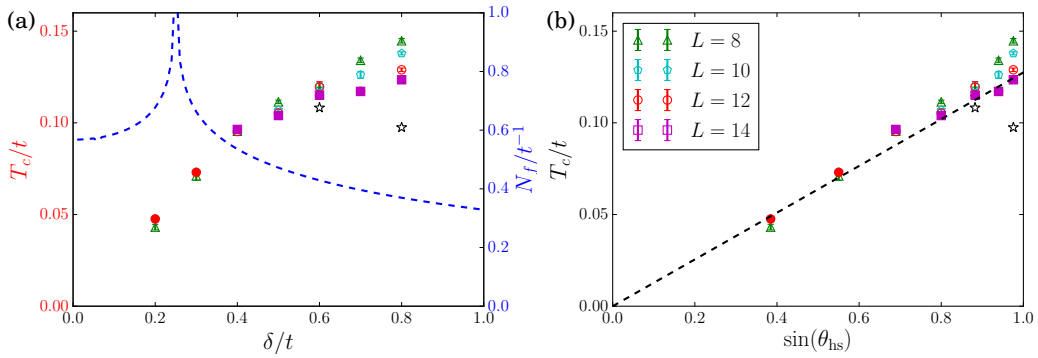

Figure 4.10: The superconducting transition temperature T_c at the QCP for different band dispersion parameters. (a) The QMC results for T_c and the calculated density of states N_f (calculated directly from the band dispersions) as function of the band dispersion parameter δ/t (see Fig. 4.4). We associate a transition temperature $T_c\,(L)$ to the temperature at which the BKT condition is met for a system of size L, and denote $T_c\,(L_{\rm max})$ by filled symbols. Analysis of finite-size effects reveals that for most values of δ/t, $T_c\,(L_{\rm max})$ is a very good estimate for the thermodynamic-limit value T_c. For the systems in which $T_c\,(L)$ does not fully converge, namely $\delta/t = 0.6$ and $\delta/t = 0.8$, $T_c(L_{\rm max})$ are upper bound values for T_c, whereas the stars are lower bound values on T_c. Note the enhanced N_f at the van Hove singularity point $\delta/t = 1/4$. (b) The linear relationship between $T_{\rm c}$ and $\sin\theta_{\rm hs}$, where $\theta_{\rm hs}$ is the angle between the two Fermi velocities of a pair of hot spots, calculated directly from the band dispersions. From Ref. [94].

4.4.5 Beyond hot spot: T_c at larger spin-fermion coupling

An important prediction of the hot-spots Eliashberg approximation is that T_c increases not only with $\sin\theta_{\rm hs}$, but also with λ^2. As a result, if the hot-spots Eliashberg approximation is correct, T_c would not be bounded and could increase indefinitely as function of the interaction parameter λ. To verify this property, we chose three band dispersion parameters and obtained T_c for several values of λ. As shown in Fig. 4.12, we find a reasonable scaling of $T_c/\sin\theta_{\rm hs}$ with λ^2 for moderately large values of the interaction parameter, i.e. λ^2 of the order of the bandwidth $8t$. The slope of this line is the same as that in Fig. 4.10b. Note that for $\lambda = 0$, we have a system of non-interacting electrons with $\chi_{\rm pair} = 2N_f \ln\left(\frac{\Lambda}{T}\right)$, implying that $T_c = 0$. More interestingly, for $\frac{\lambda^2}{8t} \gtrsim 2$, we start observing strong deviations from the λ^2 behavior, signaling the failure of the hot-spots Eliashberg approximation. Furthermore, in this regime, $T_{\rm c}$ increases very mildly and

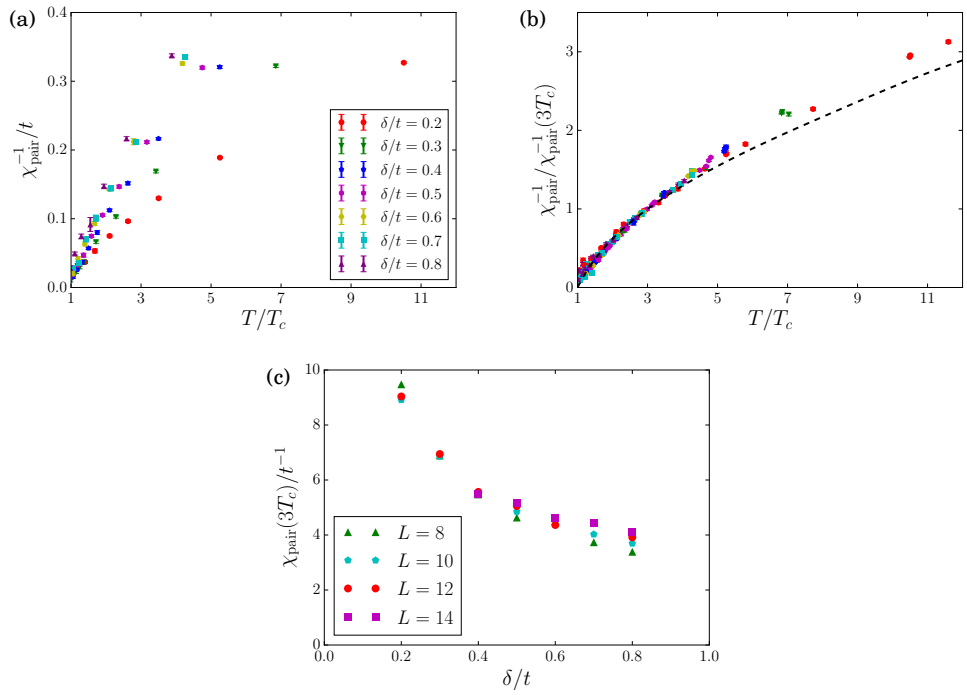

Figure 4.11: Universal temperature dependence of the pairing susceptibility $\chi_{\rm pair}$ at the QCP. (a) Temperature dependence of $\chi^{-1}_{\rm pair}$ extracted from QMC simulations for all band dispersion parameters δ/t. The system size is $L = 12$. (b) Collapse of the scaled $\chi^{-1}_{\rm pair}(T)/\chi^{-1}_{\rm pair}(3T_c)$ as function of T/T_c for all values of δ/t and all system sizes L. For each value of L, we used the corresponding $T_c(L)$. The black dashed curve is the analytical function $f^{\rm (hs)}_{\rm pair}(T/T_c)/f^{\rm (hs)}_{\rm pair}(3)$ obtained from the hot-spots Eliashberg approximation of the spin-fermion model. (c) The behavior of the QMC-extracted prefactor $A_{\rm pair} \propto \chi_{\rm pair}(3T_c)$ of Eq. 4.50 as function of δ/t. From Ref. [94].

seems to saturate.

To shed light on this saturation behavior, recall that in the two-band spin-fermion model, a pair of hot spots are split onto two electron bands. For large spin-fermion coupling, the hot spot width $\delta p_{\rm hs}$, defined in the text above Eq. 4.19, also increases. As a result, one expect that the whole Fermi surface becomes a big hot spot, and the physics crosses over from a hot-spot dominated to Fermi-surface dominated behavior. The expected T_c from the hot spot Eliashberg calculation is derived in Eq. 4.30, namely:

$$T_c = \tilde{\alpha}\tilde{\Lambda}_{\rm QCP} = \frac{\tilde{\alpha} n_b p_0 v_F}{8\pi N} \sin\theta_{\rm hs} \tag{4.63}$$

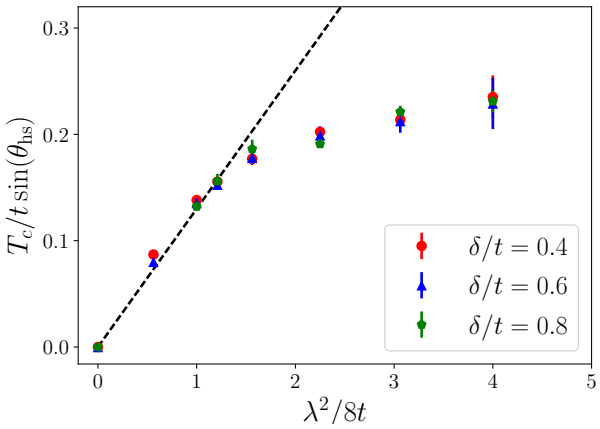

Figure 4.12: Dependence of the superconducting transition temperature on the interaction strength. For three values of the band dispersion parameter δ/t, we show the QMC results for T_c, in units of the hopping parameter t and normalized by the corresponding value of $\sin\theta_{\rm hs}$, as function of the squared coupling constant λ^2 (in units of $8t$) describing how strong the electrons interact with AFM fluctuations. The system size is $L = 12$. The dashed line, which denotes a λ^2 dependence, has the same slope as in Fig. 4.10b, and is expected from the analytical hot-spots Eliashberg solution of the spin-fermion model. The absence of the data point corresponding to $\delta/t = 0.8$ and $\lambda^2 = 4.5t$ is because T_c did not converge as function of the system size for these parameters. From Ref. [94].

It is clear that T_c becomes independent on the spin-fermion interaction strength as it becomes larger, consistent with the our QMC results.

4.4.6 Analysis and conclusion

In summary, we showed that within the spin-fermion model the SC properties near an AFM quantum critical point, including both the transition temperature T_c and the temperature-dependent pairing susceptibility $\chi_{\rm pair}$, are dominated by the properties of the hot spots, while being rather insensitive to the global properties of the Fermi surface. More specifically, the functional dependences of T_c and $\chi_{\rm pair}$ inferred from our QMC results, given by Eqs. 4.49 and 4.50, are very well captured by an approximate analytical solution of the spin-fermion model that focuses on the impact of the Landau damping on the pairing interaction. In other words, the hot-spots Eliashberg approach provides an

excellent approximate solution to the spin-fermion model, which presumably should hold also for systems with different types of band dispersions beyond the rather artifical two-band case. It is surprising that such an approximation works well even for moderately large values of the interaction λ^2 between the AFM fluctuations and the low-energy electronic states. However, our combined QMC-analytical analysis also reveals that when λ^2 becomes larger than the electronic bandwidth, the hot-spots approximation fails. Interestingly, at this crossover from hot-spots dominated pairing to Fermi-surface dominated pairing, T_c seems to start saturating, signaling that the maximum possible T_c value for this model has been achieved.

Our results have important implications to the understanding of quantum critical pairing in general. On the one hand, by establishing that the properties of the hot spots govern the SC properties of the low-energy spin-fermion model, it offers important insights into which of the many system parameters should be changed to optimize T_c in an ideal system. For instance, it becomes clear that systems with nearly-nested Fermi surfaces, where $\sin\theta_{\rm hs}$ is small, despite having an abundance of low-energy magnetic fluctuations, have a much smaller transition temperature than systems with non-nested Fermi surfaces, where $\sin\theta_{\rm hs}$ is larger. Conversely, our results establish robust and well-defined benchmarks that allow one to assess whether the SC state obtained in other microscopic models or even the superconducting state observed in actual materials falls within the "universality class" of the low-energy spin-fermion model. Two such benchmarks, for instance, are the linear dependence of T_c on $\sin\theta_{\rm hs}$ and the saturation of T_c for large interactions. Large-cluster DMFT simulations of the Hubbard model [113, 114, 115] may be able to test these benchmarks and elucidate whether the superconducting properties of the Hubbard model are determined by hot-spots properties or whether they depend on physics beyond the spin-fermion model. On the experimental front, the most promising material candidates that show signatures of AFM quantum criticality near optimal doping are electron-doped cuprates and isovalent-doped pnictides. As for hole-doped cuprates, although they do have a putative AFM quantum critical point, they also display phenomena that have yet to be observed in QMC simulations of the spin-fermion model, such as additional intertwined ordered phases [116] and a transition from small to large Fermi surface without an obvious accompanying order [117]. One interesting possibility is to investigate how pressure affects T_c in these

compounds, and correlate these changes with the pressure-induced modifications of the hot-spots properties.

4.5 Interplay between superconductivity and charge density wave physics near an antiferromagnetic quantum phase transition

4.5.1 Introduction

Charge density wave (CDW) is an electronic order where the electron density exhibits periodic modulation in real space, namely $\rho(\mathbf{r}) = \rho_0 + \Delta_{\mathrm{CDW}} \exp(i\mathbf{Q}_{\mathrm{CDW}} \cdot \mathbf{r}) + h.c.$. Here ρ_0 is the uniform electron density, and Δ_{CDW} is the CDW order parameter, with wavevector $\mathbf{Q}_{\mathrm{CDW}}$. CDW has long been observed and studied. For example, one-dimensional metals with one electron per unit cell are unstable towards the formation of a CDW ground state. This is known as the Peierl's transition[118].

In recent years, short-range CDW order has been detected inside the pseudogap region in various cuprate materials, such as $Ba_2Sr_2CaCu_2O_{8+x}$[11, 102], $YBa_2Cu_3O_{6+x}$[12], and $HgBa_2CuO_{4+x}$ [103]. The occurrence of CDW is close to the superconducting phase, and both occur when long-range antiferromagnetic order is suppressed.

The CDW wavevector is along either of the Cu-Cu directions in the CuO_2 plane, i.e., it is axial. This is shown by scanning tunneling microscopy studies on $Ba_2Sr_2CaCu_2O_{8+x}$, as well as resonant X-ray scattering studies on $YBa_2Cu_3O_{6+x}$ and $HgBa_2CuO_{4+x}$. In $HgBa_2CuO_{4+x}$, quantum oscillations suggest that the CDW phase is a double-$\mathbf{Q}$ state, where axial CDW with wavevector along both of the Cu-Cu directions coexist microscopically.

The CDW order seems to be a low-energy electronic instability. This is hinted from the fact that the wavevector is incommensurate with the underlying lattice, and seemingly follows the wavevector connecting the nesting portions of the Fermi surface[103].

If the CDW order is indeed a low energy phenomenon, similar to superconductivity, then the onset of one order is expected to suppress the other, since both compete for the same low-energy electrons. This view seems to be consistent with results from X-ray experiments in hole-doped $YBa_2Cu_3O_{6+x}$, that the charge fluctuations are suppressed at

the onset of superconductivity, and that by suppressing superconductivity with magnetic field, charge fluctuations are enhanced. On the other hand, the results on electron-doped $Nd_{1-x}Ce_xCuO_4$ [119] are a bit confusing, with enhanced charge susceptibility at very high temperatures, and seemingly uncorrelated with superconductivity.

It remains an open question as to the origin of the charge density wave order. One view, as presented in earlier sections of this chapter, is that both CDW and superconductivity are emergent due to spin fluctuations [101, 14]. In particular, in the hot-spot approximation to the spin-fermion model, there is an emergent particle-hole symmetry at each hot spot, which maps a Cooper pairing operator onto a charge density wave operator. However, such a CDW operator has a wavevector along the diagonal direction (called checkerboard CDW) rather than the bond directions of Cu-O-Cu, inconsistent with the experimental observations of singe-$\mathbf{Q}$/double-$\mathbf{Q}$ axial states described above. Ref. [101] took one step further to show that non-hot-spot properties, in particular, the nesting properties near the anti-nodal regions on the Fermi surface[3] will favor the axial orders, which can emerge if the spin fluctuations become strong enough (i.e., near magnetic quantum critical point).

CDW physics in proximity to an antiferromagnetic QCP has been studied in two separate papers [92, 110] using the Monte Carlo technique described previously. While the presence of a magnetic QCP does enhance both axial and checkerboard charge fluctuations, the enhancement is found to less than 5% at all temperatures, despite a significant boost of superconductivity. These results are in contradiction to the theoretical work presented in Ref. [14], which predicted a near-degeneracy between checkerboard CDW and superconductivity based on the hot spot approximation.

One possible reason for such a discrepancy is that CDW is a delicate phase that depends on the fine tuning of the electronic band structure beyond the hot spots. In particular, the nesting features of the Fermi surface may be crucial to observing any sort of enhanced CDW correlations. In this section, I present a detailed numerical study of the two-band spin-fermion model, focusing on purely one-dimensional band dispersions. Unlike two-dimensional band dispersions, the non-interacting charge susceptibility is logarithmically divergent at low temperatures, and any small attractions in the charge sector can induce long-range CDW order.

[3] See Fig. 4.1. Antinodal regions correspond to $(\pi, 0)$ and $(0, \pi)$ in the Brillouin zone.

This section is organized as follows: I will first describe the choice of purely one-dimensional dispersions, and point out an exact particle-hole symmetry of the spin-fermion model at half-filling. I will show that in this case, both CDW and superconductivity are equally enhanced by spin fluctuations, and present the numerical results to support it. By going away from half-filling, the exact particle-hole symmetry is broken. However, there is still the approximate particle-hole symmetry coming from the linearized hot spot approximation. I will show that this approximate symmetry in the electronic properties is insufficient in supporting a nearly-degenerate superconducting and CDW order.

4.5.2 One-dimensional band dispersion

We study a series of one-dimensional electronic band dispersions described by the following:

$$\begin{aligned} \varepsilon_{c\mathbf{k}} &= -\mu - 2t\cos k_x \\ \varepsilon_{d\mathbf{k}} &= -\mu - 2t\cos k_y \end{aligned} \tag{4.64}$$

The two electron bands are related by a 90-degree rotation. By tuning the ratio of μ/t, the wavevector Q_0 connecting parallel lines of the Fermi surface change as:

$$Q_0 = 2\arccos\frac{-\mu}{2t} \tag{4.65}$$

In particular, at half-filling $\mu = 0$, the charge density wave wavevector is $Q_0 = \pi$. Fig. 4.13 shows the two electronic Fermi surfaces for $\mu/t = -\sqrt{2}$. Hot spots on each Fermi surface are marked by purple dots. The momentum dependence and the logarithmic behavior of the non-interacting static charge susceptibility are presented in Fig. 4.14.

4.5.3 Half filling and exact $SU(2)$ symmetry

At half-filling $\mu = 0$, the two-band spin-fermion model has an exact $SU(2)$ symmetry associated with a bipartite particle-hole transformation $\mathcal{P}$, defined as:

$$\mathcal{P}\psi_a(\mathbf{r}) \equiv i\sigma_2(-1)^{i_x+i_y}\psi_a^*(\mathbf{r});\ \ \psi_a \equiv (a_\uparrow, a_\downarrow)^T \tag{4.66}$$

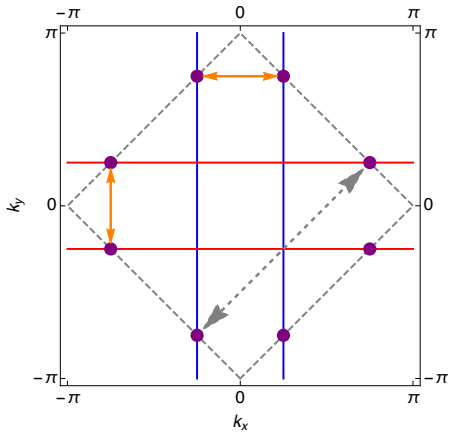

Figure 4.13: Purely one dimensional Fermi surface used in our studies. Here $\mu/t = -\sqrt{2}$. Purple points mark the location of the hot spots. Gray dashed line marks the antiferromagnetic Brillouin zone boundary, and the gray dashed arrow is the antiferromagnetic ordering wavevector $\mathbf{Q} = (\pi, \pi)$. The orange arrow $Q_0 = \pi/2$ connects parallel lines of the Fermi surface. This is the CDW wavevector favored by the Fermi surface.

where $a = c, d$ labels the two electron bands. $\mathbf{r} \equiv (i_x, i_y)$ is the lattice coordinate of the fermion field. $\psi_a^* \equiv (a_\uparrow^\dagger, a_\downarrow^\dagger)^T$, i.e., without transposing the column vector.

To see this, let's first write down the full fermion Hamiltonian on a 2D square lattice:

$$\begin{aligned} H &= -t \sum_{\mathbf{r}} \left(c_{\mathbf{r}\alpha}^\dagger c_{\mathbf{r}+\hat{x}\alpha} + d_{\mathbf{r}\alpha}^\dagger d_{\mathbf{r}+\hat{y}\alpha} \right) + \lambda \sum_{\mathbf{r}} \vec{\phi}_{\mathbf{r}} \cdot (c_{\mathbf{r}\alpha}^\dagger \vec{\sigma}_{\alpha\beta} d_{\mathbf{r}\beta} + h.c.) \\ &= -t \sum_{\mathbf{r}} \left(\psi_{c\mathbf{r}}^\dagger \sigma_0 \psi_{c\mathbf{r}+\hat{x}} + \psi_{d\mathbf{r}}^\dagger \sigma_0 \psi_{d\mathbf{r}+\hat{y}} \right) + \lambda \sum_{\mathbf{r}} \vec{\phi}_{\mathbf{r}} \cdot (\psi_{c\mathbf{r}}^\dagger \vec{\sigma} \psi_{d\mathbf{r}} + h.c.) \\ &\equiv T + V \end{aligned} \tag{4.67}$$

In the absence of the spin-fermion coupling, the nearest-neighbor hopping gives the energy dispersion described in Eq. 4.64. The second line is the matrix form in spin space, with $(\sigma_0, \vec{\sigma})$ the Pauli matrices. T and V are short-hand notations for the kinetic term and the interaction term respectively.

Under the bipartite particle-hole transformation $\mathcal{P}$, the kinetic term (T) becomes:

$$\begin{aligned} T &\xrightarrow{\mathcal{P}} -t(-1) \sum_{\mathbf{r}} \sum_{i=c,d} (i\sigma_2 \psi_i^*)^\dagger \sigma_0 (i\sigma_2 \psi_i^*) \\ &= -t(-1) \sum_{\mathbf{r}} \sum_{i=c,d} \psi_i^T (-i\sigma_2) \sigma_0 (i\sigma_2) \psi_i^* = T \end{aligned} \tag{4.68}$$

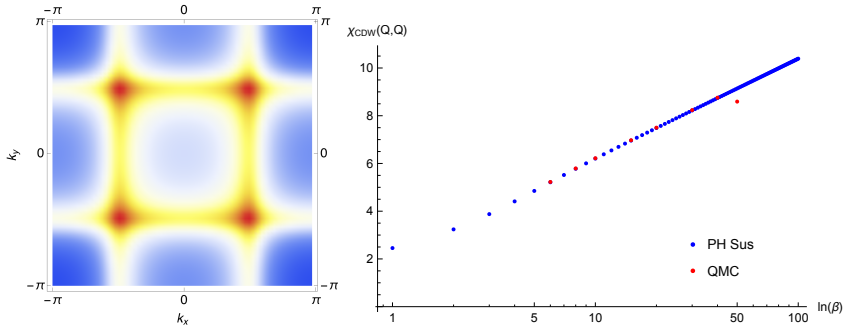

Figure 4.14: Non-interacting charge susceptibility in the Brillouin zone. Left panel: momentum space picture at inverse temperature $\beta = 12$. Right panel: $\chi(Q_0, Q_0)$ as a function of inverse temperature β. The logarithmic temperature dependence is observed from QMC as well. Here $\mu/t = -1.414$.

where the factor of (-1) comes from the bipartite transformation. The lattice indices of the fermionic fields are omitted for convenience. The last equality can be shown by re-arranging the order of the fermionic fields. As a result, the kinetic term is invariant under $\mathcal{P}$.

Similarly, the interaction term (V) describing the spin-fermion coupling is also invariant under $\mathcal{P}$-transformation. To see this, note that:

$$\begin{aligned} V &\xrightarrow{\mathcal{P}} \lambda \sum_{\mathbf{r}} \vec{\phi} \cdot \left[(i\sigma_2 \psi_c^*)^\dagger \vec{\sigma} (i\sigma_2 \psi_d^*) + h.c. \right] \\ &= \lambda \sum_{\mathbf{r}} \vec{\phi} \cdot \left[\psi_c^T (-i\sigma_2) \vec{\sigma} (i\sigma_2) \psi_d^* + h.c. \right] \\ &= \lambda \sum_{\mathbf{r}} \vec{\phi} \cdot \left(\psi_d^\dagger \vec{\sigma} \psi_c + h.c. \right) \end{aligned} \tag{4.69}$$

The last equality makes use of the fact that $\sigma_2 \vec{\sigma} \sigma_2 = (-\sigma_1, \sigma_2, -\sigma_3)$, $\sigma_2^T = -\sigma_2$ and $\sigma_i^T = \sigma_i$ for $i = 1, 3$.

We define two 4-dimensional vectors at each site, $\Psi_a \equiv (\psi_a, \mathcal{P}\psi_a)^T$, and the Hamiltonian is rewritten as:

$$H = -\frac{t}{2} \sum_{\mathbf{r}, \mu = 1 \cdots 4} \left(\Psi^\dagger_{c\mathbf{r}\mu} \sigma_0 \tau_0 \Psi_{c\mathbf{r}+\hat{x}\mu} + \Psi^\dagger_{d\mathbf{r}\mu} \sigma_0 \tau_0 \Psi_{d\mathbf{r}+\hat{y}\mu} \right) + \frac{\lambda}{2} \sum_{\mathbf{r}} \vec{\phi}_{\mathbf{r}} \cdot (\Psi^\dagger_{c\mathbf{r}} \vec{\sigma} \tau_0 \Psi_{d\mathbf{r}} + h.c.) \tag{4.70}$$

Here τ are Pauli matrices in the Nambu space. This Hamiltonian is to be compared with the Lagrangian described by Eq. 4.41 based on linearized hot spot approximation.

The Hamiltonian is invariant under the SU(2) transformations in the Nambu space (τ), as the only matrix appearing in the Hamiltonian is the identity matrix τ_0. Below I show the implications of such a symmetry to superconductivity and CDW. Unlike the hot spot SU(2) discussed previously in Sec. 4.2, where the Cooper pairing and CDW operators are mapped onto each other, here the bipartite SU(2) does not lead to such a mapping. As I show below, the susceptibilities do map onto each other in the high-T disordered phase.

Note that the sign-changing superconducting and CDW vertices are:

$$\Gamma_{\mathrm{SC}}(\mathbf{r},\tau) = \Delta i\sigma_{2\alpha\beta}\left(c_\alpha c_\beta - d_\alpha d_\beta\right) \tag{4.71}$$

$$\Gamma_{\mathrm{CDW}}(\mathbf{r},\tau) = \rho\sigma_{0\alpha\beta}\left(c^\dagger_\alpha c_\beta - d^\dagger_\alpha d_\beta\right) \tag{4.72}$$

where Δ and ρ are the superconducting and CDW order parameters respectively. The corresponding susceptibilities:

$$\chi_i(\mathbf{r},\tau) = \langle \Gamma_i(\mathbf{r},\tau)\Gamma_i^\dagger(0,0)\rangle \tag{4.73}$$

Here we show how the $s_\pm$ superconducting and (π,π) CDW are degenerate due to this symmetry. Starting from the pairing susceptibility, we have:

$$\chi_{\mathrm{SC}} = (i\sigma_{2,\alpha\beta})(-i\sigma^*_{2,\gamma\delta})\langle(c_{\mathbf{r}\alpha}c_{\mathbf{r}\beta} - d_{\mathbf{r}\alpha}d_{\mathbf{r}\beta})\left(c^\dagger_{\mathbf{0}\delta}c^\dagger_{\mathbf{0}\gamma} - d^\dagger_{\mathbf{0}\delta}d^\dagger_{\mathbf{0}\gamma}\right)\rangle \tag{4.74}$$

where for simplicity we neglected the imaginary time indices. There are four terms after expanding out the parenthesis, all in the form of:

$$\begin{aligned}\chi^{ij}_{\mathrm{SC}} &= (i\sigma_{2,\alpha\beta})(i\sigma_{2,\gamma\delta})\langle\psi_{i,\mathbf{r}\alpha}\psi_{i,\mathbf{r}\beta}\psi^\dagger_{j,\mathbf{0}\delta}\psi^\dagger_{j,\mathbf{0}\gamma}\rangle \\ &= (i\sigma_{2,\alpha\beta})(i\sigma_{2,\gamma\delta})\left(-\langle 13\rangle\langle 24\rangle + \langle 14\rangle\langle 23\rangle\right) \\ &= -2(i\sigma_{2,\alpha\beta})(i\sigma_{2,\gamma\delta})\langle 13\rangle\langle 24\rangle\end{aligned} \tag{4.75}$$

where $i,j = c,d$, and $1\cdots 4$ label the fermionic creation/annihilation operators by their respective positions in the expression. The last equality can be shown straightforwardly. Now I show that this can be transformed into the CDW susceptibility. To see this, note that under $\mathcal{P}$ transformation:

$$\begin{aligned}\chi^{ij}_{\mathrm{SC}} &= -2(i\sigma_{2,\alpha\beta})(i\sigma_{2,\gamma\delta})\langle\psi_{i,\mathbf{r}\alpha}\psi^\dagger_{j,\mathbf{0}\delta}\rangle\langle\psi_{i,\mathbf{r}\beta}\psi^\dagger_{j,\mathbf{0}\gamma}\rangle \\ &= -2(-1)^{i_x+i_y}(i\sigma_{2,\alpha\beta})(i\sigma_{2,\gamma\delta})(i\sigma_{2\alpha m})(i\sigma_{2\delta n})\langle\psi^\dagger_{i,\mathbf{r}m}\psi_{j,\mathbf{0}n}\rangle\langle\psi_{i,\mathbf{r}\beta}\psi^\dagger_{j,\mathbf{0}\gamma}\rangle \\ &= 2(-1)^{i_x+i_y}\left(\sigma_{2m\alpha}\sigma_{2,\alpha\beta}\sigma_{2,\gamma\delta}\sigma_{2\delta n}\right)\langle\psi^\dagger_{i,\mathbf{r}m}\psi_{j,\mathbf{0}n}\rangle\langle\psi_{i,\mathbf{r}\beta}\psi^\dagger_{j,\mathbf{0}\gamma}\rangle \\ &= 2(-1)^{i_x+i_y}\sigma_{0,m\beta}\sigma_{0,n\gamma}\langle\psi^\dagger_{i,\mathbf{r}m}\psi_{j,\mathbf{0}n}\rangle\langle\psi_{i,\mathbf{r}\beta}\psi^\dagger_{j,\mathbf{0}\gamma}\rangle\end{aligned} \tag{4.76}$$

This is equal to twice the corresponding term in the CDW susceptibility:

$$\begin{aligned}\chi^{ij}_{\text{CDW}} &\equiv \sigma_{0,\alpha\beta}\sigma_{0,\delta\gamma}\langle\psi^\dagger_{i,\mathbf{r}\alpha}\psi_{i,\mathbf{r}\beta}\psi^\dagger_{j,\mathbf{0}\gamma}\psi_{j,\mathbf{0}\delta}\rangle \\ &= \sigma_{0,\alpha\beta}\sigma_{0,\delta\gamma}\langle\psi^\dagger_{i,\mathbf{r}\alpha}\psi_{j,\mathbf{0}\delta}\rangle\langle\psi_{i,\mathbf{r}\beta}\psi^\dagger_{j,\mathbf{0}\gamma}\rangle\end{aligned} \tag{4.77}$$

The sign factor of $(-1)^{i_x+i_y}$ means superconducting susceptibility at $\mathbf{q}=0$ is equal to CDW susceptibility at $\mathbf{q}=(\pi,\pi)$. Unlike the approximate SU(2) symmetry from hot spot approximation, here the symmetry is exact due to half filling. Away from half filling, $\mu \neq 0$, the bipartite particle-hole symmetry is broken.

4.5.4 Main results from DQMC

We studied a series of purely one-dimensional band dispersions using DQMC, using μ/t as a tuning parameter. We studied system sizes $L=8,10,12$. Unless finite size effects are significant, I will focus on the results obtained for only $L=12$. Additionally, we choose $t=1$, and measure all other energies in units of t.

Below we will only look at charge and superconducting instabilities where there is a sign-change between the two electron bands.

Half-filling

Fig. 4.15 shows the static charge and superconducting susceptibilities at a fixed temperature $\beta=12$ at the magnetic QCP. The maximum of the charge susceptibility is at (π,π), as expected. There is no apparent enhancement for the stripe CDW with wavevectors $(\pi,0)$ or $(0,\pi)$. The maximum of SC susceptibility is at $(0,0)$, suggesting the absence of pair density wave order.

Fig. 4.16 shows the charge and pair susceptibilities divided over the non-interacting value for various temperatures and distance to magnetic QCP. Both susceptibilities are enhanced in proximity to the magnetic QCP. More interestingly, the two susceptibilities lie within errorbars of each other at the same temperatures, suggesting that the particle-hole symmetry described above is observed from numerics.

Next we look at the superconducting transition temperature. Theoretically, since there is an exact $SU(2)$ symmetry, in two dimensions there is no long range order with a finite transition temperature. Nonetheless, the correlation length grows as temperature goes down, suggesting a zero-T symmetry breaking. Numerically, only finite system sizes

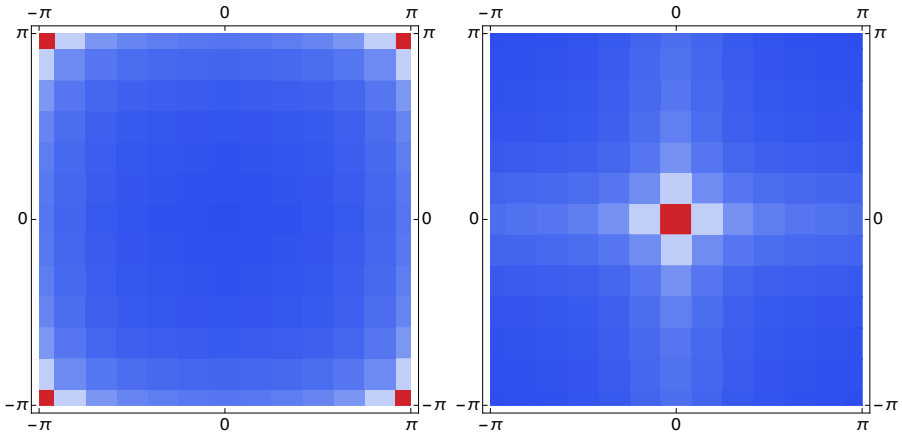

Figure 4.15: Charge (left) and superconducting (right) susceptibilities in the momentum space at the magnetic QCP. Half-filling at $\mu = 0$, $\beta = 12$. The maximum of the CDW susceptibility is at (π, π), consistent with expectations. The maximum of SC susceptibility is at $(0, 0)$, suggesting the absence of pair density wave order.

can be simulated. When the correlation length grows bigger than the linear dimension, it will resemble a transition into an ordered phase, as averaging over the space-time gives a finite order parameter. However, the transition temperature should exhibit strong finite size effects, and extrapolate to zero in the thermodynamic limit. In Fig. 4.17 I show the behavior of superfluid density ρ_s as well as the superconducting T_c defined by the Berezinskii-Kosterlitz-Thouless criterion. Both the superfluid density and the transition temperature $T_c(L)$ exhibit strong finite size effects for the three system sizes $L = 8, 10, 12$ we have studied. Although inconclusive, the strong size dependence suggests the absence of true long range order at finite temperatures.[4]

Away from half-filling

Away from half-filling, the particle-hole symmetry is absent. Nonetheless, CDW can still emerge due to spin fluctuations[101]. We studied four different band dispersions, with $Q_0 = \pi i/6$, where $i = 2, 3, 4, 5$, corresponding to period-6, period-4, period-3 and period-$\frac{12}{5}$ charge density wave orders. These are achieved by $\mu/t = -\sqrt{3}, -\sqrt{2}, -1, -\frac{1}{2}\arccos\frac{5}{12}$

[4] The computation time scales exponentially with the lattice dimension L, due to calculation of the fermion determinant, see appendix A. Therefore, $L = 12$ is the maximum system size we have investigated.

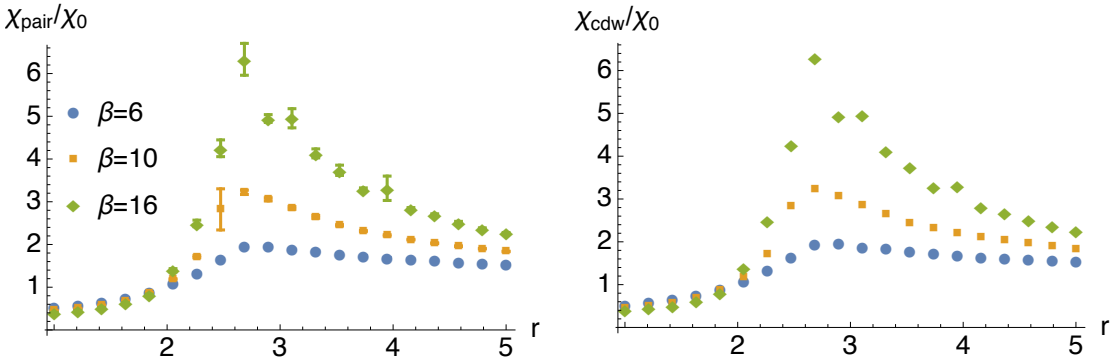

Figure 4.16: d-wave charge (left) and superconducting (right) susceptibilities plotted versus distance to magnetic QCP for temperatures $\beta = 6, 10, 16$.

respectively. The choice of the periods are because these are the exact wavevectors that can be probed in DQMC for $L = 12$.

Fig. 4.18 shows the static charge susceptibility in momentum space at the magnetic QCP. All results are presented for $\beta = 12$. The location of the maximum charge susceptibility is consistent with the wavevectors favored by the respective Fermi surfaces.

In Fig. 4.19, we show the dependence of the superconducting and CDW susceptibilities on the distance to magnetic QCP for the four band dispersions. Although both SC and CDW are enhanced by the presence of quantum critical spin fluctuations, SC is enhanced much stronger compared to CDW. The lifting of the CDW-SC degeneracy is already quite apparent at $Q_0 = 5\pi/6$, i.e. a small deviation from half-filling, suggesting the extreme sensitivity of charge order to the exact particle-hole symmetry.

To illustrate the competition between CDW and superconductivity, in Fig. 4.20 we plot the temperature evolution of superconducting and charge susceptibilities at the magnetic QCP for the electronic band dispersion corresponding to period-4 CDW. At high temperatures, both susceptibilities increase as temperature goes down, suggesting the tendency towards long range order. However, near the onset of the superconducting phase via a BKT transition, the charge susceptibility decreases with decreasing temperature, suggesting that the presence of long-range superconducting order suppresses

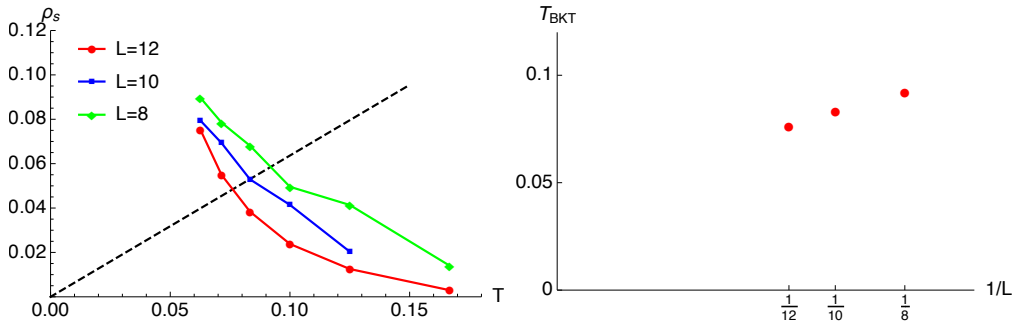

Figure 4.17: Left: superfluid density versus temperature for $L = 8, 10, 12$. Right: extracted BKT transition temperature $T_c(L)$. Finite size effects are significant in these properties.

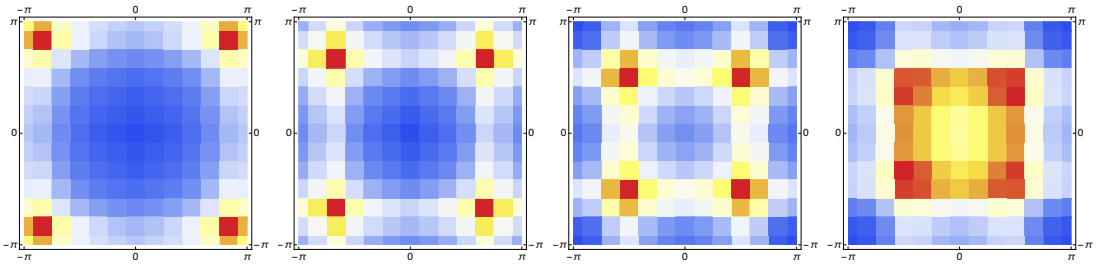

Figure 4.18: Charge susceptibilities in the momentum space for period-$\frac{12}{5}$, period-3, period-4 and period-6 charge density wave orders. All results are obtained at the magnetic QCP. $\beta = 12$.

CDW. This is consistent with X-ray measurements on $YBa_2Cu_3O_{6+x}$ [12], as well as other theoretical calculations [120].

Can stripe CDW fluctuations be favored over the checkerboard CDW fluctuations?

As has been discussed above, at the magnetic QCP, the maximum charge susceptibility is always located along the diagonal direction. While this is expected based on the hot spot approximation to the spin-fermion model, it is not consistent with experimental results.

In Fig. 4.21 we show the comparison of the charge susceptibility in the magnetically ordered phase and at the magnetic QCP. The results are obtained for the electronic band dispersion favoring a period-4 CDW. It is obvious that in the magnetically ordered

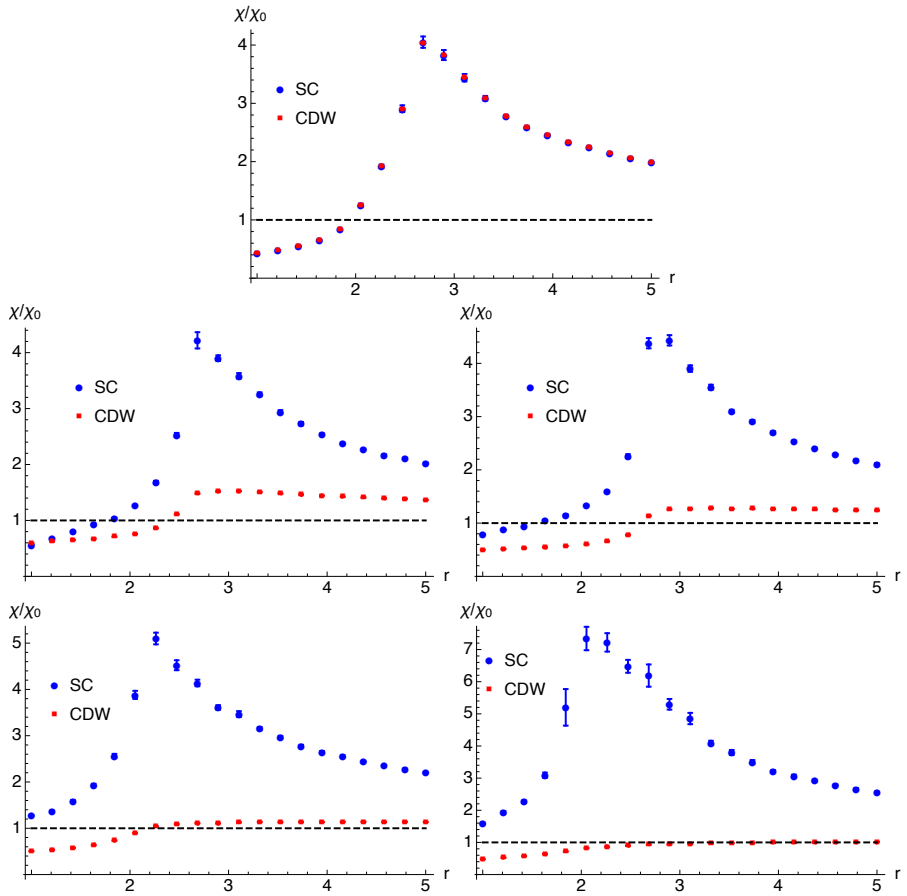

Figure 4.19: Charge and superconducting susceptibilities for a inverse fixed temperature $\beta = 12$. The band dispersions correspond to half-filling (top), period-$\frac{12}{5}$ (middle left), period-3 (middle right), period-4 (bottom left) and period-6 (bottom right) CDW.

phase, the maximum of the charge susceptibility is along the Cu-O-Cu bond directions. In the right panel of Fig. 4.21, we quantify the checkerboard to axial CDW evolution by defining the ratio of the maximum charge susceptibility along diagonal and bond directions: $\chi(Q_0, Q_0)/\chi(\tilde{Q}, 0)$.[5] This ratio has a sharp change at the magnetic QCP, suggesting that axial CDW correlations are favored when the Fermi surface undergoes a reconstruction due to the onset of long range magnetic order. A qualitative argument has been given based on nodal/antinodal asymmetry of the Fermi surface due to the

[5] Due to Fermi surface reconstruction in SDW phase, the maximum charge susceptibility may not sit exactly at Q_0.

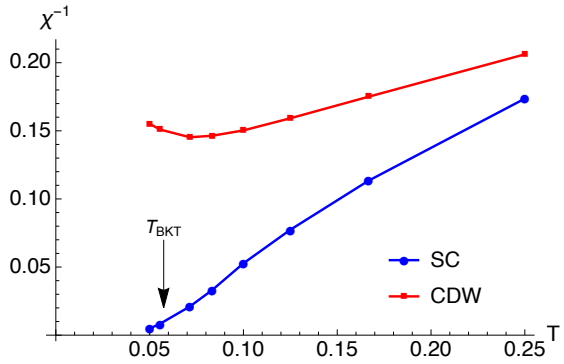

Figure 4.20: Inverse charge and superconducting susceptibilities versus temperature at the magnetic QCP.

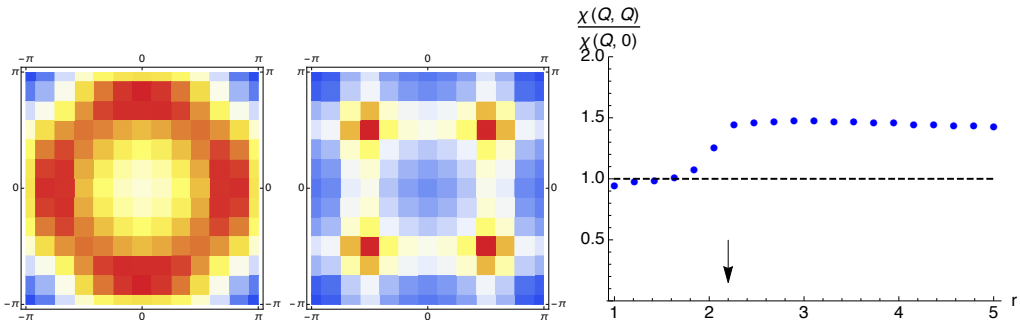

Figure 4.21: Charge susceptibilities in the magnetically ordered phase (left) versus at the magnetic quantum critical point (middle). Results obtained based on the band dispersion favoring period-4 CDW. The ratio between the maximum charge susceptibilities along the Cu-O-Cu bond direction and the diagonal direction is shown in the right figure. The arrow marks the location of the magnetic QCP.

opening of an enegy gap at the hot spots [101].

4.5.5 Analysis and conclusion

By considering purely one dimensional band dispersions, we find signatures of charge density wave order numerically within the two-band spin-fermion model. Through Fig. 4.16 and 4.19, we see that charge susceptibility is enhanced in proximity to an antiferromagnetic QCP, suggesting the possibility of CDW induced by quantum spin fluctuations.

By contrasting the results for band dispersions at and away from half-filling, we

see that the CDW is very delicate, requiring Fermi surface fine tuning, and loses to superconductivity very quickly when the exact particle-hole symmetry is broken. The competition between SC and CDW is evident from the numerical results, in particular, from Fig. 4.20. The degeneracy lifting is already apparent at temperatures above the superconducting phase. One method to understand it is through the negative feedback of superconducting fluctuations on charge density wave fluctuations.

We also analyzed the checkerboard versus axial CDW correlations. As is shown in Fig. 4.21, the axial CDW correlations can only be favored in the magnetically ordered phase, when the Fermi surface develops an energy gap at the hot spots.

4.6 Conclusions

In this chapter, we discussed several aspects of the low-energy electronic phase diagram of cuprate high temperature superconductors, focusing on the proximity to an antiferromagnetic quantum critical point. We investigated the so-called spin-fermion model, which is a low-energy effective model describing quantum critical spin fluctuations coupled to electrons near the Fermi surface. By combined analytical and numerical work, we revealed the low energy physics of the model, and how microscopic system parameters govern the superconducting and charge density wave properties.

In Sec. 4.2, following past works [13, 14, 101], we presented an analytical solution of the spin-fermion model. In particular, based on the Eliashberg approach, we discussed the importance of special points on the Fermi surface called hot spots, and how their properties uniquely determine the superconducting properties. We also pointed out a special particle-hole symmetry due to the linearized hot spot approximation, which gives rise to an emergent symmetry between superconductivity and charge density wave. This gives a qualitative argument why in many cuprate materials, superconductivity and charge density wave order are found near each other in the phase diagram.

In Sec. 4.4, we presented a numerical solution of the spin-fermion model using a Determinantal Quantum Monte Carlo technique, focusing on the superconducting properties in proximity to an antiferromagnetic quantum critical point. By carefully tuning the low-energy electronic properties, in particular those relevant to the hot spots, we

discovered a functional dependence of superconducting transition temperature and susceptibility on the hot spot properties (Eq. 4.49 and 4.50). We find a remarkable agreement between the numerical solutions and those predicted by the hot spot Eliashberg approach. We also studied the failure of the hot spot approximation by going to large spin-fermion interactions, and concluded that the saturation of T_c is due to the whole Fermi surface acting like one big hot spot.

In Sec. 4.5, we studied the possibility of a charge density wave order in the spin-fermion model, and discussed its interplay with superconductivity. We studied a series of purely one-dimensional electronic band dispersions at and away from half-filling. We find that the while both superconductivity and charge density wave order are enhanced due to the presence of quantum critical spin fluctuations, charge density wave is a rather delicate order extremely sensitive to the fine-tuning of the electronic band dispersion beyond the hot spot properties. In particular, charge density wave is quickly suppressed away from half-filling, where an exact particle-hole symmetry guarantees the degeneracy between charge density wave and superconductivity.

Chapter 5

Conclusion

In this thesis, I discussed several aspects of the phase diagram of high-T_c cuprate and iron pnictide/chalcogenide superconductors, and addressed several important questions pertaining to the research community.

In Ch. 2, I investigated the nature and origin of the magnetic phases in the iron pnictide materials. Comparing the magnetic phase diagrams arising from a localized J_1-J_2 spin-Heisenberg model, and from an itinerant model describing weakly interacting electrons near the Fermi surface, I showed that the magnetic orders which preserve square lattice symmetry naturally occurs only in the itinerant model. I showed how these magnetic orders can become the ground state due to imperfect Fermi surface nesting (induced by doping, pressure etc.), the residual electronic interactions (i.e., interactions which do not contribute directly to the magnetic instabilities), and the effect of Néel antiferromagnetic fluctuations (induced by doping local magnetic moments). Since the existence of tetragonal magnetic orders is crucial in identifying the microscopic origin of magnetism, I proposed unique experimental manifestations of these orders in the electronic properties and collective spin excitations.

In Ch. 3, I investigated the origin of electronic nematic order in the iron pnictide materials. In particular, I discussed in detail the magnetic scenario, where nematic order is driven by strong magnetic fluctuations. I showed that while at a mean-field level, the nematic order and the magnetic order occur simultaneously, once fluctuations are accounted for, the two transitions can be split. I proceeded to discuss the

experimental manifestations of electronic nematicity, focusing on its effect on the local density of states near an impurity, which can be visualized by atomically-resolved spectroscopy. Through the successful modeling of the results obtained by scanning tunneling spectroscopy, I demonstrated the intimate relationship between nematicity and large amplitude magnetic fluctuations in iron pnictide materials.

In Ch. 4, I investigated the physics of superconductivity (SC) and charge density wave (CDW) near a metallic antiferromagnetic quantum critical point (QCP). By numerically solving the spin-fermion model via a sign-problem-free Quantum Monte Carlo technique, I showed the significance of hot spot properties in uniquely determining the superconducting transition temperature and the superconducting fluctuations in proximity to the antiferromagnetic QCP. The numerical results on SC have remarkable quantitative agreement with those calculated by an approximate field-theoretic method, reminiscent of the Eliashberg approach used in the electron-phonon problem. This result is somewhat surprising, and requires further investigations. I also discussed the CDW physics in the spin-fermion model, and studied its interplay with SC. The numerical results reveal the competition between SC and CDW, consistent with other theoretical calculations and experimental results. By studying a series of electronic band dispersions, I showed that the CDW is a delicate phase, sensitive to the fine tuning of the band properties beyond the hot spots.

Appendix A

Determinantal Quantum Monte Carlo and Application to two band spin-fermion model

A.1 Monte Carlo basics

Statistical systems are composed of macroscopic number of particles. At thermal equilibrium they are characterized by their phase space Ω and probability distribution ρ, with the condition $\int_\Omega \rho = 1$. $\ln \rho$ is an additive quantity of the system, and therefore can be represented by integrals of motion, i.e., $\ln \rho = -\beta E + (...)$, where E is the total energy of the system, β the inverse temperature. (...) are other integrals of motion (linear and angular momentum, particle number etc.). Thermodynamic observables are averaged quantities $\langle \mathcal{O} \rangle \equiv \int_\Omega \mathcal{O}\rho$. For example, the phase space of a classical N-particle system is the set of position and momentum of each individual particle: $\mathrm{d}\Omega = \Pi_{i=1}^{N} \mathrm{d}q_i \mathrm{d}p_i$, and $\rho \propto \exp(-\beta E)$ the probability density. For quantum systems, the phase space consists of many-body quantum states $\{\Sigma_i\}$, and $\rho \propto \langle \Sigma_i | \exp(-\beta \hat{H}) | \Sigma_i \rangle$. For quantum field theories, the phase space consists of paths in field configurations $\{\phi(\mathbf{r}, \tau)\}$, and the probability $\rho \propto \exp(-S\{\phi(\mathbf{r}, \tau)\})$, where $S = \int_{\mathbf{r},\tau} \mathcal{L}$ is the action.

With the knowledge of $\{\Omega, \rho\}$, we can compute all thermodynamic properties of the system. In reality, due to the interactions between constituents, seldomly do we have

analytical solutions. On the other hand, it is precisely the interactions that drive various phases of matter, such as superconductivity and magnetism.

Monte Carlo (MC) is a powerful numerical method for understanding the properties of interacting systems. The basic idea is to generate a finite ensemble M of configurations $\tilde{\Omega}$, where the probability of finding a certain configuration $\tilde{\Sigma}_i \in \tilde{\Omega}$ is

$$\tilde{P}(\tilde{\Sigma}_i) = \frac{\rho(\tilde{\Sigma}_j)}{\sum_{j=1}^{M} \rho(\tilde{\Sigma}_j)} \tag{A.1}$$

While the physical observable is:

$$\langle \mathcal{O} \rangle_{\tilde{\Omega}} \equiv \frac{1}{M} \sum_{i=1}^{M} \mathcal{O}(\tilde{\Sigma}_i) \tag{A.2}$$

In the limit of $M \to \infty$, the expectation value of physical observables converge to the thermodynamic properties.

The Monte Carlo method is based on the detailed balance principle, which states that for statistical system at thermal equilibrium, each elementary process is equilibrated with its reverse process. Take two states of the system i and j. Detailed balance principle requires that

$$\rho_i W_{i \to j} = \rho_j W_{j \to i} \tag{A.3}$$

where ρ_i is the thermal equilibrium probability density, and $W_{i \to j}$ the transition probability from i to j.

Based on the detailed balance principle, the MC ensemble can be constructed following a Markov process described as follows:

(1) Start from a initial configuration Σ_0, compute the thermal probability density $\rho_0 \equiv \langle \exp(-\beta \hat{H}) \rangle_0$. Generate new configurations successively based on the Markov transition probability $W_{i \to i+1}$.

(2) For the $(i+1)$th iteration, construct a trial configuration Σ_{i+1}, and compute ρ_{i+1}. Accept the trial configuration with probability $W_{i \to i+1}$. If $\rho_{i+1} > \rho_i$, $W_{i \to i+1} = 1$; If $\rho_{i+1}/\rho_i < 1$, $W_{i \to i+1} = \rho_{i+1}/\rho_i$.

The definition of the transition probability is consistent with the detailed balance principle. Therefore, as the number of iterations goes to infinity, the thermodynamic limit is reached.

A.2 Applications to coupled boson-fermion system

This section reproduces the results previously published in Ref. [105].

In the path-integral formulation, the coupled boson-fermion system we are interested in is described by a space-time local action:

$$S = S_\phi + \int \mathrm{d}\tau \mathrm{d}^d\mathbf{x}\ \bar{\psi}(\mathbf{x},\tau)\left(\partial_\tau + \mathcal{H}\right)\psi(\mathbf{x},\tau) \tag{A.4}$$

where $\tau \in (0,\beta)$ is the imaginary time going from 0 to inverse temperature β. S_ϕ denotes the bosonic action. ϕ describes a generic boson field, and $\bar{\psi}$ ψ are anticommuting Grassmann variables describing fermionic fields. Note that both ϕ and ψ can have multiple components. $\mathcal{H} \equiv \mathcal{T} + \mathcal{V}$ is the fermion Hamiltonian density, with $\mathcal{T}$ the kinetic energy and $\mathcal{V}$ the boson-fermion interaction. The partition function: $\mathcal{Z} = \int_\Omega \exp(-S)$, and the phase space Ω consists of bosonic and fermionic paths in space-time.

In doing Monte Carlo study, both imaginary time and space are discretized to form a $d+1$ dimensional lattice. Since the imaginary time axis is finite, it is discretized to N steps, with $\Delta_\tau \equiv \beta/N$. The discretization error is $\mathcal{O}(\Delta_\tau)$. The space is discretized into L^d lattice points, with linear dimension L. Note that the space is truncated to a volume of L^d with a certain boundary condition. This inevitably introduces finite size effects, which I will describe later.

Since Grassmann variables are not c-numbers, and cannot be directly sampled, the logic is to integrate out the fermionic degrees of freedom, which are described by Gaussian fluctuations, to obtain an effective probability density for the boson fields:

$$\rho \propto \exp(-S_{\text{eff}}) \equiv \exp(-S_\phi)\ \det\nolimits_{\tau,\mathbf{x}}\{\partial_\tau + H\} \tag{A.5}$$

where the *fermion determinant* is formally defined as $\det_{\mathbf{x},\tau}\{\partial_\tau + H\}$. While the bosonic action is local in space and time, the fermion determinant is inherently non local. The size of the matrix is $nNL^d \times nNL^d$, where n is the local Hilbert space of fermions. As a result, the computation complexity of the fermion determinant is then $\mathcal{O}((nNL^d)^3)$ (e.g., using LU factorization). This is a daunting task, and strongly limits the lattice size that can be studied using Monte Carlo method.

However, it is easy to see that the fermion determinant is sparse along the τ axis, in that it connects between adjacent time only. The fermionic action can be written

explicitly as (neglecting spatial index):

$$\int \mathrm{d}\tau \bar{\psi} \left(\partial_\tau + H\right) \psi \equiv \sum_{i=1}^{N} \bar{\psi}_i \psi_i + \bar{\psi}_i \left(-1 + \Delta_\tau H_{i-1}\right) \psi_{i-1} \tag{A.6}$$

where $\psi \equiv (\psi_1 \cdots \psi_{nL^d})$ is a vector in space, and H is a $nL^d \times nL^d$ matrix. Casted in a matrix form ($\psi_N = -\psi_0$):

$$\begin{pmatrix} \bar{\psi}_0 & \bar{\psi}_1 & \cdots & \bar{\psi}_{N-1} \end{pmatrix} \begin{pmatrix} 1 & 0 & \cdots & 0 & (1-\Delta_\tau H_{N-1}) \\ -(1-\Delta_\tau H_0) & 1 & \cdots & 0 & 0 \\ \vdots & \vdots & \ddots & \vdots & \vdots \\ 0 & 0 & \cdots & 1 & 0 \\ 0 & 0 & \cdots & -(1-\Delta_\tau H_{N-2}) & 1 \end{pmatrix} \begin{pmatrix} \psi_0 \\ \psi_1 \\ \vdots \\ \psi_{N-1} \end{pmatrix} \tag{A.7}$$

As a result, the fermion determinant shown in Eq. A.5 becomes:

$$\det{}_{\tau,\mathbf{x}} = \ \det{}_{\mathbf{x}} \left\{\mathcal{I} + B_{N-1} \cdots B_1 B_0\right\} \tag{A.8}$$

where $B_i \equiv 1 - \Delta_\tau H_i \approx \exp(-\Delta_\tau H_i)$. The exponential form is used to reduce discretization error. The complexity of evaluating the fermion determinant is $\mathcal{O}(N(nL^d)^3)$, much reduced compared to taking the full determinant.

A.3 Computing fermionic Green's function

The calculation of one-particle fermionic Green's function is shown as follows:

$$\begin{aligned} G(\mathbf{x}, \tau; \mathbf{x}', \tau') &\equiv \langle \mathcal{T} \left[\psi(\mathbf{x}, \tau) \psi^\dagger(\mathbf{x}', \tau')\right] \rangle \\ &= \frac{1}{\mathcal{Z}} \int \exp(-S_B) \ \det{}_{\mathbf{x},\tau} \{\partial_\tau + H\} \mathcal{G}(\mathbf{x}, \tau; \mathbf{x}', \tau') \end{aligned} \tag{A.9}$$

where

$$\mathcal{G}(\mathbf{x}, \tau; \mathbf{x}', \tau') \equiv \frac{1}{\det_{\mathbf{x},\tau}\{\partial_\tau + H\}} \int \exp(-S_F) \mathcal{T} \left[\psi(\mathbf{x}, \tau) \psi^\dagger(\mathbf{x}', \tau')\right] \tag{A.10}$$

is the Green's function for a fixed bosonic configuration. Again, the calculation of $\mathcal{G}$ can be simplified by utilizing the specific time dependence of the fermionic Hamiltonian. By defining $\mathcal{G}(\mathbf{x}, \tau; \mathbf{x}', \tau') \equiv \langle \mathbf{x} | \mathcal{G}(\tau, \tau') | \mathbf{x}' \rangle$, we have:

$$\begin{aligned} \mathcal{G}(\tau, \tau') &= U(\tau, \tau') J^{-1}(\tau') \text{ if } \beta > \tau > \tau' \\ &= -U(\tau, 0) U(\beta, \tau') J^{-1}(\tau') \text{ if } \beta > \tau' > \tau \end{aligned} \tag{A.11}$$

where $U(\tau,\tau') \equiv \mathcal{T}\exp(-\int_{\tau}^{\tau'} H)$, and $J(\tau) \equiv \mathcal{I} + U(\tau,0)U(\beta,\tau)$. We can show that the above definition satisfies

$$(\partial_\tau + H)\,\mathcal{G}(\tau,\tau') = \delta(\tau-\tau')\mathcal{I} \tag{A.12}$$

for $\tau \neq \tau'$. The $\tau = \tau'$ criterion is satisfied with:

$$\lim_{\epsilon\to 0_+} \mathcal{G}(\tau'+\epsilon,\tau') - \mathcal{G}(\tau'-\epsilon,\tau') = \mathcal{I} \tag{A.13}$$

In the discretized time scheme, we have for $(i+1)\Delta_\tau > \tau > i\Delta_\tau$, $(j+1)\Delta_{\tau'} > \tau' > j\Delta_{\tau'}$, and $i \geq j$:

$$\mathcal{G}(\tau,\tau') = B_{i-1}B_{i-2}\cdots B_{j+1}B_j\left(\mathcal{I} + B_{j-1}\cdots B_0 B_{N-1}\cdots B_j\right)^{-1} \tag{A.14}$$

The equal time Green's function $\mathcal{G}(\tau,\tau-0_+)$, which is particularly useful in devising the Monte Carlo algorithm, is:

$$\mathcal{G}(\tau,\tau-0+) \equiv \mathcal{G}_i = \left(\mathcal{I} + B_{i-1}\cdots B_0 B_{N-1}\cdots B_i\right)^{-1} \tag{A.15}$$

To move forward along the imaginary time axis (i.e., going from the time slot $(i+1)\Delta_\tau > \tau > i\Delta_\tau$ to $(i+2)\Delta_\tau > \tau > (i+1)\Delta_\tau$):

$$\mathcal{G}_{i+1} = B_i \mathcal{G}_i B_i^{-1} \tag{A.16}$$

The occupation number at a given time slice is given by:

$$n_i \equiv \langle \psi^\dagger(\tau)\psi(\tau-0_+)\rangle = \mathcal{I} - \mathcal{G}_i \tag{A.17}$$

A.4 Monte Carlo procedure

This section reproduces the results previously published in Ref. [91, 92].

From the above analysis, the coupled boson-fermion system is reduced to an effective bosonic problem, with probability density given by Eq. A.5. The Monte Carlo procedure for solving the coupled boson-fermion system, which goes under the name of *Determinantal Quantum Monte Carlo* (DQMC), is described as follows:

The procedure starts by specifying an initial bosonic configuration on the discretized space-time lattice, and constructing the initial fermionic equal-time Green's function at

$\tau = 0$. The Markov chain proceeds by proposing a space-time local change to the bosonic configuration, and computing the change in the fermion determinant as well as the bosonic action. The criterion for accepting/rejecting the change is based on the detailed balance principle, and discussed in Sec. A.1. When all the space in a time slice has been scanned, proceed to the next time slice. One iteration is completed after the field configuration on the entire lattice has been updated.

The most time consuming procedure per DQMC iteration is computing the change in the fermion determinant as well as updating the Green's function once the proposed change is accepted. Below I show how they are computed.

At a given time slice $(m+1)\Delta_\tau > \tau > m\Delta_\tau$, let us propose a change in the field at $\mathbf{x}_0$. The ratio of the fermion determinant before and after the change is

$$R = \frac{\det_{\mathbf{x}}\{\mathcal{I} + B_{m-1}\cdots B_0 B_{N-1}\cdots B'_m\}}{\det_{\mathbf{x}}\{\mathcal{I} + B_{m-1}\cdots B_0 B_{N-1}\cdots B_m\}} \tag{A.18}$$

where $B_i \equiv \exp(-\Delta_\tau H_m) \approx \exp(-\Delta_\tau T)\exp(-\Delta_\tau V_m)$. The change in the field gives rise to

$$B'_m \approx \exp(-\Delta_\tau T)\exp(-\Delta_\tau V'_m) = B_m \exp(-\Delta_\tau(V'_m - V_m)) \equiv B_m(\mathcal{I} + N) \tag{A.19}$$

where $N \equiv \exp(-\Delta_\tau(V'_m - V_m)) - \mathcal{I}$ is a matrix which is non-zero only at $(\mathbf{x}_0, \mathbf{x}_0)$. As a result,

$$\begin{aligned} R &= \frac{\det_{\mathbf{x}}\{\mathcal{I} + B_{m-1}\cdots B_0 B_{N-1}\cdots B_m(\mathcal{I}+N)\}}{\det_{\mathbf{x}}\{\mathcal{I} + B_{m-1}\cdots B_0 B_{N-1}\cdots B_m\}} \\ &= \frac{\det_{\mathbf{x}}\{\mathcal{G}_m^{-1} + (\mathcal{G}_m^{-1} - \mathcal{I})N\}}{\det_{\mathbf{x}} \mathcal{G}_m^{-1}} \\ &= \det_{\mathbf{x}}\{\mathcal{I} + (\mathcal{I} - \mathcal{G}_m)N\} \\ &= \det_{\mathbf{x}_0}\{\mathcal{I} + (\mathcal{I} - \mathcal{G}_m)N\} \end{aligned} \tag{A.20}$$

where $\det_{\mathbf{x}_0}$ denotes the local fermionic Hilbert space (spin, orbital etc.) at site $\mathbf{x}_0$. As a result, with the knowledge of the equal-time Green's function $\mathcal{G}_m$, the time cost of computing the determinant ratio is $\mathcal{O}(n^3)$, and it does not scale with lattice size.

Once the proposed change in the bosonic field is accepted, the new equal-time

Green's function needs to be calculated. The updated Green's function is:

$$\begin{aligned}\mathcal{G}'_m &= \left(\mathcal{I} + B_{m-1}\cdots B_0 B_{N-1}\cdots B'_m\right)^{-1} \\ &= \left[\mathcal{G}_m^{-1} + (\mathcal{G}_m^{-1} - \mathcal{I})N\right]^{-1} \\ &= \left[\mathcal{I} + (\mathcal{I} - \mathcal{G}_m)N\right]^{-1}\mathcal{G}_m\end{aligned} \tag{A.21}$$

The computation of the matrix inverse go as follows. N is a sparse matrix whose only nonzero entry resides in a $n \times N$ block at $(\mathbf{x}_0, \mathbf{x}_0)$. Therefore, only n columns of $\mathcal{I} - \mathcal{G}_m$ multiplies N. We can define u v as $N \times n$ matrices, with u the n columns of $\mathcal{I} - \mathcal{G}_m$, and v the n rows of N. As a result,

$$\mathcal{G}'_m = \left(\mathcal{I} + uv^\dagger\right)^{-1}\mathcal{G}_m = \mathcal{G}_m - u\left(1 + v^\dagger u\right)^{-1}v^\dagger\mathcal{G}_m \tag{A.22}$$

The last step utilizes the Shermann-Morrison formula : $(1+uv^\dagger)^{-1} = 1-u(1+v^\dagger u)^{-1}v^\dagger$. Therefore, the matrix inverse is on a $n \times n$ matrix rather than $nL^d \times nL^d$ matrix. The total computation complexity is $\mathcal{O}(L^{2d})$, rather than $\mathcal{O}(L^{3d})$ if computed directly.

A.5 Fermion sign problem

A basic assumption for applying the DQMC method is to have a positive transition probability $W_{i\to i+1}$. From Eq. A.5, the sampling probability density is proportional to the fermion determinant. The determinant $\det_{\mathbf{x}}\{\mathcal{I} + B_{N-1}\cdots B_0\}$ is not necessarily positive definite, and can even become complex, due to the time-ordering of the B matrices. As a result, the transition probability used in the Markov process is ill-defined. The sign problem is less of an issue at high temperatures, where the variation of fields is slow in time, and $B_{N-1}\cdots B_0 \approx \exp(-\beta H)$ is Hermitian. It becomes rather severe at low temperatures, where the most interesting physics of phases of matter and phase transitions occur.

Despite no general way around the sign problem, there are certain classes of Hamiltonians where such a sign problem is absent. Ref. [107] presents a sufficient criterion for sign-problem-free DQMC calculations: if the fermionic Hamiltonian is invariant under an anti-unitary transformation, then the fermion determinant is positive definite. Such an anti-unitary transformation A satisfies the following conditions:

$$A^2 = -1;\ AHA^{-1} = H \tag{A.23}$$

In the presence of such a symmetry, the Hamiltonian possesses a Kramers doublet. As a result, all eigenvalues have a corresponding complex conjugate pair. Models which fall in this category include the negative-U Hubbard model, positive-U Hubbard model at half-filling, etc.. Generic spin-fermion models do not possess such a symmetry. However, as I will show below, a two-band generalization can be constructed for DQMC studies.

A.6 Sign-problem free DQMC for two-band spin-fermion model

The spin fermion model describes the coupling between a vector boson $\vec{\phi}$ with the spin of itinerant electrons. The coupling is assumed to be Yukawa-type, i.e.,

$$V = \lambda \sum_i \vec{\phi}_i \cdot \psi^\dagger_{i\alpha} \vec{\sigma}_{\alpha\beta} \psi_{i\beta} \tag{A.24}$$

where λ is the Yukawa coupling strength, i is the lattice label, and $\vec{\sigma}$ are Pauli matrices in spin space. The kinetic energy of the electrons can also be written on a lattice, with

$$T = \sum_{ij;\alpha} (-t_{ij} - \mu\delta_{ij}) \psi^\dagger_{i\alpha} \psi_{i\alpha} \tag{A.25}$$

where t_{ij} is the hopping amplitude between site i and j, and μ the chemical potential (working with canonical ensemble).

The one-band spin-fermion model does not possess such an anti-unitary symmetry described previously, therefore suffers from sign problem when performing DQMC. However, the sign problem is absent for a two-band spin-fermion model, where the vector boson scatters electrons between different flavors:

$$V' = \lambda \sum_i \vec{\phi}_i \cdot \left(c^\dagger_{i\alpha} \vec{\sigma}_{\alpha\beta} d_{i\beta} + h.c. \right) \tag{A.26}$$

where c and d are annihilation operators for two electron flavors. Written in a matrix form:

$$V' = \lambda \sum_i \vec{\phi}_i \cdot \begin{pmatrix} c^\dagger_\uparrow & c^\dagger_\downarrow & d^\dagger_\uparrow & d^\dagger_\downarrow \end{pmatrix} \begin{pmatrix} 0 & \vec{\sigma} \\ \vec{\sigma} & 0 \end{pmatrix} \begin{pmatrix} c_\uparrow \\ c_\downarrow \\ d_\uparrow \\ d_\downarrow \end{pmatrix} \equiv \lambda \sum_i \vec{\phi}_i \cdot \Psi^\dagger \vec{\sigma} \otimes \tau_1 \Psi \tag{A.27}$$

where $\vec{\tau}$ are Pauli matrices in the flavor basis, and $\otimes$ means the direct product of two matrices. It is easy to verify that $A \equiv i\sigma_2 \otimes \tau_3 \mathcal{C}$ is the anti-unitary symmetry of the Hamiltonian, where $\mathcal{C}$ is the complex conjugation operator. To see this, note that:

$$A^{-1}(\vec{\sigma} \otimes \tau_1)A = -i\sigma_2 \otimes \tau_3(\vec{\sigma}^* \otimes \tau_1)i\sigma_2 \otimes \tau_3 = -(-i\sigma_2\vec{\sigma}^* i\sigma_2) \otimes (\tau_3\tau_1\tau_3) \tag{A.28}$$

The last equation is equal to $\vec{\sigma} \otimes \tau_1$ following the anticommuting algebra of the Pauli matrices.

A.7 XY spin and simplification of the fermionic Hamiltonian

In the DQMC technique, the most time consuming procedure is the computation of the fermion determinant, defined in Eq. A.8. This strongly limits the system sizes we can study. In this section, I will show that if the vector boson has two components (i.e., XY spin) rather than three (i.e., Heisenberg spin), there is a spectral symmetry that reduces the local fermionic Hilbert space from 4 (i.e., spin$\times$band) to 2. Note that going from Heisenberg to XY spins do not alter the low-energy electronic phase diagram at a qualitative level.

To see this, let us consider $\vec{\phi} = (\phi_x, \phi_y)$. As a result, the vector boson flips of the spin of the electron when it is scattered from one band to to other. We can define two spinors as:

$$\psi_1 \equiv (c_\uparrow, d_\downarrow)^T \; ; \; \psi_2 \equiv (c_\downarrow, d_\uparrow)^T \tag{A.29}$$

The spin-fermion interaction Hamiltonian Eq. A.27 can be rewritten to be:

$$V' = \lambda \sum_i \left(\psi_{1i}^\dagger \vec{\phi} \cdot \vec{\sigma} \psi_{1i} + \psi_{2i}^\dagger \vec{\phi} \cdot \vec{\sigma}^* \psi_{2i} \right) \tag{A.30}$$

It is easy to see that the fermion Hamiltonian can be written as a direct sum of two 2×2 blocks:

$$H = H_1 \oplus H_2 \tag{A.31}$$

where the $H_1 = H_2^*$. As a result, the fermion determinant defined in Eq. A.8 can be recast as:

$$\sum_{a=1,2} \det{}_{\mathbf{x}} \left\{ \mathcal{I}^{(a)} + B_{N-1}^{(a)} \cdots B_0^{(a)} \right\} \Rightarrow \left| \det{}_{\mathbf{x}} \left\{ \mathcal{I}^{(1)} + B_{N-1}^{(1)} \cdots B_0^{(1)} \right\} \right|^2 \tag{A.32}$$

Such a reduction of dimensionality comes from the fact that spin rotation symmetry for XY spins has a one-dimension faithful representation, in the form of $(\phi_x, \phi_y) \Leftrightarrow |\phi| \exp(i\theta)$. For Heisenberg spins, such a reduction does not exist.

A.8 Reducing finite size effects using a magnetic flux

One common issue associated with Monte Carlo simulations is finite size effects. In our DQMC procedure, the system is placed on a $L \times L$ square lattice. To extrapolate to the thermodynamic limit, large system sizes needs to be studied. However, due to limitations in the computing resources, the maximum linear dimension we can study is on the order of 10. Finite size effects are severe when extracting various critical temperatures for the onset of long range order, such as superconductivity and charge density wave.

There is an even bigger problem associated with simulations on a finite lattice, due to insufficient sampling of the electronic states. To illustrate this problem, we consider the example of applying periodic boundary conditions to the fermionic degrees of freedom, namely:

$$c_{\mathbf{r}} = c_{\mathbf{r}+L\hat{x}} = c_{\mathbf{r}+L\hat{y}} = c_{\mathbf{r}+L\hat{x}+L\hat{y}} \tag{A.33}$$

where $\hat{x}/\hat{y}$ are unit vectors along the x y directions. As a result, in the Brillouin zone, only states with wavevectors $\mathbf{k} = \frac{2\pi}{L}(l_x, l_y);\ l_{x/y} = 1...L$ are included in the calculations.

On the other hand, at low temperatures, the physics is determined by electronic states near the Fermi surface, which is a one-dimensional submanifold of the two-dimensional Brillouin zone. As a result, out of the L^2 momentum states, only $\mathcal{O}(L)$ states are responsible for the physics of various electronic orders. Finite size effects become extremely severe in computing low-energy electronic properties. In Fig. A.1, I show how the finite system size affects the compressibility of the non-interacting system.

To reduce the finite size effects, we follow Ref. [108, 92] to thread a magnetic flux quanta $\Phi_z = h/e$ through the two-dimensional square lattice. Qualitatively, the reduction of finite size effects due to a magnetic flux can be understood as follows: The presence of a boundary has a stronger effect on delocalized electrons (e.g., in a metal) than localized electrons (e.g., in an insulator). The presence of a magnetic flux can localize electronic states, therefore reducing the effects caused by having a boundary.

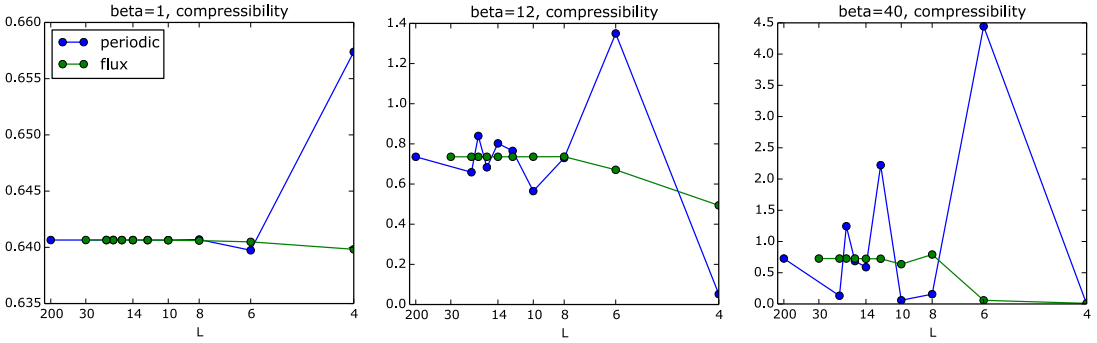

Figure A.1: Compressibility of the non-interacting electronic system, calculated from density-density correlation function. β is the inverse temperature. Blue points are calculated with periodic boundary conditions, and green points are calculated by threading a magnetic flux quanta described in the main text. Here the electronic band parameters are taken from Ref. [92]. Figure is a courtesy from Yoni Schattner.

Since only one flux quanta is applied through the entire square lattice, the magnetic field is $B_z = \Phi_z/L^2$, and is a small perturbation $\mathcal{O}(L^{-2})$. Such a flux does not alter the electronic properties in the thermodynamic limit. To preserve the anti-unitary symmetry of the Hamiltonian, the applied flux quanta is band and spin dependent. In practice, we used the following ansatz:

$$\Phi_{c\uparrow} = -\Phi_{c\downarrow};\ \Phi_{c\alpha} = -\Phi_{d\alpha} \tag{A.34}$$

where $\alpha = \uparrow\downarrow$ labels electronic spin. Fig. A.1 shows the reduction of the finite size effects by threading a flux quanta. In particular, at low temperatures $T \approx 0.5\%$ of the electronic bandwidth (figure to the right), the thermodynamic compressibility is achieved for a system size of $L \approx 10$.

One tradeoff with threading a magnetic flux is that the periodic boundary conditions are destroyed, and we can no longer probe the momentum space properties for the one-particle Green's functions. However, some four-point correlation functions, such as Cooper pairing correlation and density-density correlation, still preserve the periodic boundary conditions, and the momentum states are still good quantum numbers. To see this, we look at the example of a pairing correlator, defined as:

$$\chi(\mathbf{r}_1, \tau_1; \mathbf{r}_2, \tau_2) \equiv \langle c_{\mathbf{r}_1\uparrow}(\tau_1) c_{\mathbf{r}_1\downarrow}(\tau_1) c^\dagger_{\mathbf{r}_2\downarrow}(\tau_2) c^\dagger_{\mathbf{r}_2\uparrow}(\tau_2) \rangle \tag{A.35}$$

Following the ansatz defined in Eq. A.34, for c electrons, opposite spins feel a magnetic field in the opposite directions. As a result, translation of $L\hat{x}$ or $L\hat{y}$ leaves the correlator unchanged.

References

[1] Pia Jensen Ray. Structural investigation of $La_{2-x}Sr_xCuO_{4+y}$ - Following staging as a function of temperature. Master's thesis, Niels Bohr Institute, Faculty of Science, University of Copenhagen. Copenhagen, Denmark, November 2015.

[2] R. Doll and M. Näbauer. Experimental Proof of Magnetic Flux Quantization in a Superconducting Ring. *Phys. Rev. Lett.*, 7:51–52, Jul 1961.

[3] Bascom S. Deaver and William M. Fairbank. Experimental Evidence for Quantized Flux in Superconducting Cylinders. *Phys. Rev. Lett.*, 7:43–46, Jul 1961.

[4] W. A. Little and R. D. Parks. Observation of Quantum Periodicity in the Transition Temperature of a Superconducting Cylinder. *Phys. Rev. Lett.*, 9:9–12, Jul 1962.

[5] J. Bardeen, L. N. Cooper, and J. R. Schrieffer. Theory of Superconductivity. *Phys. Rev.*, 108:1175–1204, Dec 1957.

[6] Emanuel Maxwell. Isotope Effect in the Superconductivity of Mercury. *Phys. Rev.*, 78:477–477, May 1950.

[7] C. A. Reynolds, B. Serin, W. H. Wright, and L. B. Nesbitt. Superconductivity of Isotopes of Mercury. *Phys. Rev.*, 78:487–487, May 1950.

[8] Neven Barišić, Mun K. Chan, Yuan Li, Guichuan Yu, Xudong Zhao, Martin Dressel, Ana Smontara, and Martin Greven. Universal sheet resistance and revised phase diagram of the cuprate high-temperature superconductors. *Proceedings of the National Academy of Sciences*, 110(30):12235–12240, 07 2013.

[9] Johnpierre Paglione and Richard L. Greene. High-temperature superconductivity in iron-based materials. *Nat Phys*, 6(9):645–658, 09 2010.

[10] D. J. Scalapino. A common thread: The pairing interaction for unconventional superconductors. *Rev. Mod. Phys.*, 84:1383–1417, Oct 2012.

[11] Andrej Mesaros, Kazuhiro Fujita, Stephen D. Edkins, Mohammad H. Hamidian, Hiroshi Eisaki, Shin-ichi Uchida, J. C. Séamus Davis, Michael J. Lawler, and Eun-Ah Kim. Commensurate $4a_0$-period charge density modulations throughout the $Bi_2Sr_2CaCu_2O_{8+x}$ pseudogap regime. *Proceedings of the National Academy of Sciences*, 113(45):12661–12666, 2016.

[12] J. Chang, E. Blackburn, A. T. Holmes, N. B. Christensen, J. Larsen, J. Mesot, Ruixing Liang, D. A. Bonn, W. N. Hardy, A. Watenphul, M. v. Zimmermann, E. M. Forgan, and S. M. Hayden. Direct observation of competition between superconductivity and charge density wave order in $YBa_2Cu_3O_{6.67}$. *Nat Phys*, 8(12):871–876, 12 2012.

[13] Ar. Abanov, Andrey V. Chubukov, and J. Schmalian. Quantum-critical theory of the spin-fermion model and its application to cuprates: Normal state analysis. *Advances in Physics*, 52(3):119–218, 2003.

[14] Max A. Metlitski and Subir Sachdev. Quantum phase transitions of metals in two spatial dimensions. II. Spin density wave order. *Phys. Rev. B*, 82:075128, Aug 2010.

[15] K. B. Efetov, H. Meier, and C. Pepin. Pseudogap state near a quantum critical point. *Nat Phys*, 9(7):442–446, 07 2013.

[16] N. Barišić, M. K. Chan, M. J. Veit, C. J. Dorow, Y. Ge, Y. Tang, W. Tabis, G. Yu, X. Zhao, and M. Greven. Hidden Fermi-liquid behavior throughout the phase diagram of the cuprates. *arXiv:1507.07885*, 2015.

[17] Rafael M. Fernandes, Daniel K. Pratt, Wei Tian, Jerel Zarestky, Andreas Kreyssig, Shibabrata Nandi, Min Gyu Kim, Alex Thaler, Ni Ni, Paul C. Canfield, Robert J. McQueeney, Jörg Schmalian, and Alan I. Goldman. Unconventional pairing in the iron arsenide superconductors. *Phys. Rev. B*, 81:140501, Apr 2010.

[18] M. D. Watson, T. K. Kim, A. A. Haghighirad, S. F. Blake, N. R. Davies, M. Hoesch, T. Wolf, and A. I. Coldea. Suppression of orbital ordering by chemical pressure in $FeSe_{1-x}S_x$. *Phys. Rev. B*, 92:121108, Sep 2015.

[19] T. Shibauchi, A. Carrington, and Y. Matsuda. A Quantum Critical Point Lying Beneath the Superconducting Dome in Iron Pnictides. *Annual Review of Condensed Matter Physics*, 5(1):113–135, 2014.

[20] Qisi Wang, Yao Shen, Bingying Pan, Xiaowen Zhang, K. Ikeuchi, K. Iida, A. D. Christianson, H. C. Walker, D. T. Adroja, M. Abdel-Hafiez, Xiaojia Chen, D. A. Chareev, A. N. Vasiliev, and Jun Zhao. Magnetic ground state of FeSe. *Nature Communications*, 7:12182 EP –, 07 2016.

[21] Rafael M Fernandes and Andrey V Chubukov. Low-energy microscopic models for iron-based superconductors: a review. *Reports on Progress in Physics*, 80(1):014503, 2017.

[22] John A. Hertz. Quantum critical phenomena. *Physical Review B*, 14(3):1165–1184, 1976.

[23] A. J. Millis. Effect of a nonzero temperature on quantum critical points in itinerant fermion systems. *Physical Review B*, 48(10):7183–7196, 1993.

[24] Subir Sachdev. *Quantum Phase Transitions*. Cambridge University Press, second edition edition, 2011.

[25] Matthias Vojta. Quantum phase transitions. *Reports on Progress in Physics*, 66(12):2069, 2003.

[26] K. M. Taddei, J. M. Allred, D. E. Bugaris, S. H. Lapidus, M. J. Krogstad, H. Claus, D. Y. Chung, M. G. Kanatzidis, R. Osborn, S. Rosenkranz, and O. Chmaissem. Observation of the magnetic C4 phase in $Ca_{1-x}Na_xFe_2As_2$ and its universality in the hole-doped 122 superconductors. *Physical Review B - Condensed Matter and Materials Physics*, 95(6), 2 2017.

[27] D. D. Khalyavin, S. W. Lovesey, P. Manuel, F. Krüger, S. Rosenkranz, J. M. Allred, O. Chmaissem, and R. Osborn. Symmetry of reentrant tetragonal phase

in $Ba_{1-x}Na_xFe_2As_2$: Magnetic versus orbital ordering mechanism. *Phys. Rev. B*, 90:174511, Nov 2014.

[28] S. Avci, O. Chmaissem, J. M. Allred, S. Rosenkranz, I. Eremin, A. V. Chubukov, D. E. Bugaris, D. Y. Chung, M. G. Kanatzidis, J. P Castellan, J. A. Schlueter, H. Claus, D. D. Khalyavin, P. Manuel, A. Daoud-Aladine, and R. Osborn. Magnetically driven suppression of nematic order in an iron-based superconductor. *Nature Communications*, 5:3845 EP –, 05 2014.

[29] A. E. Böhmer, F. Hardy, L. Wang, T. Wolf, P. Schweiss, and C. Meingast. Superconductivity-induced re-entrance of the orthorhombic distortion in $Ba_{1x}K_xFe_2As_2$. *Nature Communications*, 6:7911 EP –, 07 2015.

[30] M. G. Kim, A. Kreyssig, A. Thaler, D. K. Pratt, W. Tian, J. L. Zarestky, M. A. Green, S. L. Bud'ko, P. C. Canfield, R. J. McQueeney, and A. I. Goldman. Antiferromagnetic ordering in the absence of structural distortion in $Ba(Fe_{1-x}Mn_x)_2As_2$. *Phys. Rev. B*, 82:220503, Dec 2010.

[31] G. S. Tucker, D. K. Pratt, M. G. Kim, S. Ran, A. Thaler, G. E. Granroth, K. Marty, W. Tian, J. L. Zarestky, M. D. Lumsden, S. L. Bud'ko, P. C. Canfield, A. Kreyssig, A. I. Goldman, and R. J. McQueeney. Competition between stripe and checkerboard magnetic instabilities in Mn-doped $BaFe_2As_2$. *Phys. Rev. B*, 86:020503, Jul 2012.

[32] J. Lorenzana, G. Seibold, C. Ortix, and M. Grilli. Competing Orders in FeAs Layers. *Phys. Rev. Lett.*, 101:186402, Oct 2008.

[33] I. Eremin and A. V. Chubukov. Magnetic degeneracy and hidden metallicity of the spin-density-wave state in ferropnictides. *Phys. Rev. B*, 81:024511, Jan 2010.

[34] P. M. R. Brydon, Jacob Schmiedt, and Carsten Timm. Microscopically derived Ginzburg-Landau theory for magnetic order in the iron pnictides. *Phys. Rev. B*, 84:214510, Dec 2011.

[35] Xiaoyu Wang and Rafael M. Fernandes. Impact of local-moment fluctuations on the magnetic degeneracy of iron arsenide superconductors. *Phys. Rev. B*, 89:144502, Apr 2014.

[36] Xiaoyu Wang, Jian Kang, and Rafael M. Fernandes. Magnetic order without tetragonal-symmetry-breaking in iron arsenides: Microscopic mechanism and spin-wave spectrum. *Phys. Rev. B*, 91:024401, Jan 2015.

[37] Jian Kang, Xiaoyu Wang, Andrey V. Chubukov, and Rafael M. Fernandes. Interplay between tetragonal magnetic order, stripe magnetism, and superconductivity in iron-based materials. *Phys. Rev. B*, 91:121104, Mar 2015.

[38] R. M. Fernandes, S. A. Kivelson, and E. Berg. Vestigial chiral and charge orders from bidirectional spin-density waves: Application to the iron-based superconductors. *Phys. Rev. B*, 93:014511, Jan 2016.

[39] Alexander Altland and Benjamin Simons. *Condensed Matter Field Theory*. Cambridge University Press, 2nd edition, 2010.

[40] Suchitra E Sebastian, J Gillett, N Harrison, P H C Lau, D J Singh, C H Mielke, and G G Lonzarich. Quantum oscillations in the parent magnetic phase of an iron arsenide high temperature superconductor. *Journal of Physics: Condensed Matter*, 20(42):422203, 2008.

[41] M. M. Qazilbash, J. J. Hamlin, R. E. Baumbach, Lijun Zhang, D. J. Singh, M. B. Maple, and D. N. Basov. Electronic correlations in the iron pnictides. *Nat Phys*, 5(9):647–650, 09 2009.

[42] Z. P. Yin, K. Haule, and G. Kotliar. Kinetic frustration and the nature of the magnetic and paramagnetic states in iron pnictides and iron chalcogenides. *Nat Mater*, 10(12):932–935, 12 2011.

[43] Jian Kang and Zlatko Tešanović. Theory of the valley-density wave and hidden order in iron pnictides. *Phys. Rev. B*, 83:020505, Jan 2011.

[44] R. M. Fernandes, A. V. Chubukov, J. Knolle, I. Eremin, and J. Schmalian. Preemptive nematic order, pseudogap, and orbital order in the iron pnictides. *Phys. Rev. B*, 85:024534, Jan 2012.

[45] A. V. Balatsky, D. N. Basov, and Jian-Xin Zhu. Induction of charge density waves by spin density waves in iron-based superconductors. *Phys. Rev. B*, 82:144522, Oct 2010.

[46] Qimiao Si and Elihu Abrahams. Strong Correlations and Magnetic Frustration in the High T_c Iron Pnictides. *Phys. Rev. Lett.*, 101:076401, Aug 2008.

[47] Frank Krüger, Sanjeev Kumar, Jan Zaanen, and Jeroen van den Brink. Spin-orbital frustrations and anomalous metallic state in iron-pnictide superconductors. *Phys. Rev. B*, 79:054504, Feb 2009.

[48] P. Chandra, P. Coleman, and A. I. Larkin. Ising transition in frustrated Heisenberg models. *Phys. Rev. Lett.*, 64:88–91, Jan 1990.

[49] S Graser, T A Maier, P J Hirschfeld, and D J Scalapino. Near-degeneracy of several pairing channels in multiorbital models for the Fe pnictides. *New Journal of Physics*, 11(2):025016, 2009.

[50] D. J. Singh and M.-H. Du. Density Functional Study of $LaFeAsO_{1-x}F_x$: A Low Carrier Density Superconductor Near Itinerant Magnetism. *Phys. Rev. Lett.*, 100:237003, Jun 2008.

[51] A. V. Chubukov, D. V. Efremov, and I. Eremin. Magnetism, superconductivity, and pairing symmetry in iron-based superconductors. *Phys. Rev. B*, 78:134512, Oct 2008.

[52] Saurabh Maiti and Andrey V. Chubukov. Renormalization group flow, competing phases, and the structure of superconducting gap in multiband models of iron-based superconductors. *Phys. Rev. B*, 82:214515, Dec 2010.

[53] Ronny Thomale, Christian Platt, Jiangping Hu, Carsten Honerkamp, and B. Andrei Bernevig. Functional renormalization-group study of the doping dependence of pairing symmetry in the iron pnictide superconductors. *Phys. Rev. B*, 80:180505, Nov 2009.

[54] M. J. Calderón, G. León, B. Valenzuela, and E. Bascones. Magnetic interactions in iron superconductors studied with a five-orbital model within the Hartree-Fock and Heisenberg approximations. *Phys. Rev. B*, 86:104514, Sep 2012.

[55] Qinlong Luo and Elbio Dagotto. Magnetic phase diagram of a five-orbital Hubbard model in the real-space Hartree-Fock approximation varying the electronic density. *Phys. Rev. B*, 89:045115, Jan 2014.

[56] D. C. Johnston, R. J. McQueeney, B. Lake, A. Honecker, M. E. Zhitomirsky, R. Nath, Y. Furukawa, V. P. Antropov, and Yogesh Singh. Magnetic exchange interactions in $BaMn_2As_2$: A case study of the J_1-J_2-J_c Heisenberg model. *Phys. Rev. B*, 84:094445, Sep 2011.

[57] Jiming An, A. S. Sefat, D. J. Singh, and Mao-Hua Du. Electronic structure and magnetism in $BaMn_2As_2$ and $BaMn_2Sb_2$. *Phys. Rev. B*, 79:075120, Feb 2009.

[58] Rafael M. Fernandes and Andrew J. Millis. Suppression of Superconductivity by Néel-Type Magnetic Fluctuations in the Iron Pnictides. *Phys. Rev. Lett.*, 110:117004, Mar 2013.

[59] N. Plonka, A. F. Kemper, S. Graser, A. P. Kampf, and T. P. Devereaux. Tunneling spectroscopy for probing orbital anisotropy in iron pnictides. *Phys. Rev. B*, 88:174518, Nov 2013.

[60] Ying Ran, Fa Wang, Hui Zhai, Ashvin Vishwanath, and Dung-Hai Lee. Nodal spin density wave and band topology of the FeAs-based materials. *Phys. Rev. B*, 79:014505, Jan 2009.

[61] J. Knolle, I. Eremin, and R. Moessner. Multiorbital spin susceptibility in a magnetically ordered state: Orbital versus excitonic spin density wave scenario. *Phys. Rev. B*, 83:224503, Jun 2011.

[62] Vladimir Cvetkovic and Oskar Vafek. Space group symmetry, spin-orbit coupling, and the low-energy effective Hamiltonian for iron-based superconductors. *Phys. Rev. B*, 88:134510, Oct 2013.

[63] Haruki Watanabe and Hitoshi Murayama. Unified Description of Nambu-Goldstone Bosons without Lorentz Invariance. *Phys. Rev. Lett.*, 108:251602, Jun 2012.

[64] M W Long and W Yueung. Multiple spin density waves of an itinerant antiferromagnet. *Journal of Physics F: Metal Physics*, 16(6):769, 1986.

[65] Jun Zhao, D. T. Adroja, Dao-Xin Yao, R. Bewley, Shiliang Li, X. F. Wang, G. Wu, X. H. Chen, Jiangping Hu, and Pengcheng Dai. Spin waves and magnetic exchange interactions in $CaFe_2As_2$. *Nat Phys*, 5(8):555–560, 08 2009.

[66] L. W. Harriger, H. Q. Luo, M. S. Liu, C. Frost, J. P. Hu, M. R. Norman, and Pengcheng Dai. Nematic spin fluid in the tetragonal phase of $BaFe_2As_2$. *Phys. Rev. B*, 84:054544, Aug 2011.

[67] Daniel D. Scherer, Ilya Eremin, and Brian M. Andersen. Collective magnetic excitations of C_4-symmetric magnetic states in iron-based superconductors. *Phys. Rev. B*, 94:180405, Nov 2016.

[68] Y. Kamiya, N. Kawashima, and C. D. Batista. Dimensional crossover in the quasi-two-dimensional Ising-O(3) model. *Phys. Rev. B*, 84:214429, Dec 2011.

[69] Andrey Chubukov, Eduardo Gagliano, and Carlos Balseiro. Phase diagram of the frustrated spin-1/2 Heisenberg antiferromagnet with cyclic-exchange interaction. *Phys. Rev. B*, 45:7889–7898, Apr 1992.

[70] E. W. Carlson, D. X. Yao, and D. K. Campbell. Spin waves in striped phases. *Phys. Rev. B*, 70:064505, Aug 2004.

[71] J T Haraldsen and R S Fishman. Spin rotation technique for non-collinear magnetic systems: application to the generalized Villain model. *Journal of Physics: Condensed Matter*, 21(21):216001, 2009.

[72] Marianne Rotter, Marcus Tegel, Dirk Johrendt, Inga Schellenberg, Wilfried Hermes, and Rainer Pöttgen. Spin-density-wave anomaly at 140 K in the ternary iron arsenide $BaFe_2As_2$. *Phys. Rev. B*, 78:020503, Jul 2008.

[73] R. Applegate, J. Oitmaa, and R. R. P. Singh. Spin waves in $J_{1a}-J_{1b}-J_2$ orthorhombic square-lattice Heisenberg models: Application to iron pnictide materials. *Phys. Rev. B*, 81:024505, Jan 2010.

[74] Chen Fang, Hong Yao, Wei-Feng Tsai, JiangPing Hu, and Steven A. Kivelson. Theory of electron nematic order in LaFeAsO. *Phys. Rev. B*, 77:224509, Jun 2008.

[75] Jiun-Haw Chu, James G. Analytis, Kristiaan De Greve, Peter L. McMahon, Zahirul Islam, Yoshihisa Yamamoto, and Ian R. Fisher. In-Plane Resistivity Anisotropy in an Underdoped Iron Arsenide Superconductor. *Science*, 329(5993):824–826, 2010.

[76] Jiun-Haw Chu, Hsueh-Hui Kuo, James G. Analytis, and Ian R. Fisher. Divergent Nematic Susceptibility in an Iron Arsenide Superconductor. *Science*, 337(6095):710–712, 2012.

[77] Weicheng Lv, Jiansheng Wu, and Philip Phillips. Orbital ordering induces structural phase transition and the resistivity anomaly in iron pnictides. *Phys. Rev. B*, 80:224506, Dec 2009.

[78] R. M. Fernandes, A. V. Chubukov, and J. Schmalian. What drives nematic order in iron-based superconductors? *Nat Phys*, 10(2):97–104, 02 2014.

[79] Michael Schütt, Jörg Schmalian, and Rafael M. Fernandes. Origin of DC and AC conductivity anisotropy in iron-based superconductors: Scattering rate versus spectral weight effects. *Phys. Rev. B*, 94:075111, Aug 2016.

[80] E. P. Rosenthal, E. F. Andrade, C. J. Arguello, R. M. Fernandes, L. Y. Xing, X. C. Wang, C. Q. Jin, A. J. Millis, and A. N. Pasupathy. Visualization of electron nematicity and unidirectional antiferroic fluctuations at high temperatures in NaFeAs. *Nat Phys*, 10(3):225–232, 03 2014.

[81] Erick F. Andrade, Ayelet D. Notis, Ethan P. Rosenthal, Xiaoyu Wang, Lingyi Xing, Xiancheng Wang, Changqing Jin, Rafael M. Fernandes, Andrew J. Millis, and Abhay N. Pasupathy. Elasto-Scanning Tunneling Microscopy – an Atomic-Resolution Probe of Electronic Anisotropy. *Submitted*, 2017.

[82] A. F. Wang, X. G. Luo, Y. J. Yan, J. J. Ying, Z. J. Xiang, G. J. Ye, P. Cheng, Z. Y. Li, W. J. Hu, and X. H. Chen. Phase diagram and calorimetric properties of $NaFe_{1-x}Co_xAs$. *Phys. Rev. B*, 85:224521, Jun 2012.

[83] M Yi, D H Lu, R G Moore, K Kihou, C-H Lee, A Iyo, H Eisaki, T Yoshida, A Fujimori, and Z-X Shen. Electronic reconstruction through the structural and magnetic transitions in detwinned NaFeAs. *New Journal of Physics*, 14(7):073019, 2012.

[84] P. A. Lee, T. M. Rice, and P. W. Anderson. Fluctuation Effects at a Peierls Transition. *Phys. Rev. Lett.*, 31:462–465, Aug 1973.

[85] Y. Dagan, M. M. Qazilbash, C. P. Hill, V. N. Kulkarni, and R. L. Greene. Evidence for a Quantum Phase Transition in $Pr_{2-x}Ce_xCuO_{4-\delta}$ from Transport Measurements. *Phys. Rev. Lett.*, 92:167001, Apr 2004.

[86] Louis Taillefer. Scattering and Pairing in Cuprate Superconductors. *Annual Review of Condensed Matter Physics*, 1(1):51–70, 2010.

[87] E. M. Motoyama, G. Yu, I. M. Vishik, O. P. Vajk, P. K. Mang, and M. Greven. Spin correlations in the electron-doped high-transition-temperature superconductor $Nd_{2-x}Ce_xCuO_4$. *Nature*, 445(7124):186–189, 01 2007.

[88] T. Shibauchi, A. Carrington, and Y. Matsuda. A Quantum Critical Point Lying Beneath the Superconducting Dome in Iron Pnictides. *Annual Review of Condensed Matter Physics*, 5(1):113–135, 2014.

[89] Bumsoo Kyung, Jean-Sébastien Landry, and A.-M. S. Tremblay. Antiferromagnetic fluctuations and d-wave superconductivity in electron-doped high-temperature superconductors. *Phys. Rev. B*, 68:174502, Nov 2003.

[90] Yuxuan Wang, Artem Abanov, Boris L. Altshuler, Emil A. Yuzbashyan, and Andrey V. Chubukov. Superconductivity near a Quantum-Critical Point: The Special Role of the First Matsubara Frequency. *Phys. Rev. Lett.*, 117:157001, Oct 2016.

[91] Erez Berg, Max A. Metlitski, and Subir Sachdev. Sign-Problem–Free Quantum Monte Carlo of the Onset of Antiferromagnetism in Metals. *Science*, 338(6114):1606–1609, 2012.

[92] Yoni Schattner, Max H. Gerlach, Simon Trebst, and Erez Berg. Competing Orders in a Nearly Antiferromagnetic Metal. *Phys. Rev. Lett.*, 117:097002, Aug 2016.

[93] Max H. Gerlach, Yoni Schattner, Erez Berg, and Simon Trebst. Quantum critical properties of a metallic spin-density-wave transition. *Phys. Rev. B*, 95:035124, Jan 2017.

[94] Xiaoyu Wang, Yoni Schattner, Erez Berg, and Rafael M. Fernandes. Superconductivity mediated by quantum critical antiferromagnetic fluctuations: the rise and fall of hot spots. *arXiv:1609.09568*, 09 2016.

[95] Ar. Abanov and Andrey V. Chubukov. Spin-Fermion Model near the Quantum Critical Point: One-Loop Renormalization Group Results. *Physical Review Letters*, 84(24):5608–5611, 2000.

[96] Rui-Hua He, M. Hashimoto, H. Karapetyan, J.D. Koralek, J.P. Hinton, J.P. Testaud, V. Nathan, Y. Yoshida, Hong Yao, K. Tanaka, W. Meevasana, R.G. Moore, D.H. Lu, S.-K. Mo, M. Ishikado, H. Eisaki, Z. Hussain, T.P. Devereaux, S.A. Kivelson, J. Orenstein, A. Kapitulnik, and Z.-X. Shen. From a Single-Band Metal to a High-Temperature Superconductor via Two Thermal Phase Transitions. *Science*, 331(6024):1579–1583, 2011.

[97] Sung-Sik Lee. Low-energy effective theory of Fermi surface coupled with U(1) gauge field in $2+1$ dimensions. *Phys. Rev. B*, 80:165102, Oct 2009.

[98] David F. Mross, John McGreevy, Hong Liu, and T. Senthil. Controlled expansion for certain non-Fermi-liquid metals. *Phys. Rev. B*, 82:045121, Jul 2010.

[99] Ar. Abanov, A. V. Chubukov, and M. R. Norman. Gap anisotropy and universal pairing scale in a spin-fluctuation model of cuprate superconductors. *Phys. Rev. B*, 78:220507, Dec 2008.

[100] Jian Kang and Rafael M. Fernandes. Robustness of quantum critical pairing against disorder. *Phys. Rev. B*, 93:224514, Jun 2016.

[101] Yuxuan Wang and Andrey Chubukov. Charge-density-wave order with momentum $(2Q, 0)$ and $(0, 2Q)$ within the spin-fermion model: Continuous and discrete symmetry breaking, preemptive composite order, and relation to pseudogap in hole-doped cuprates. *Phys. Rev. B*, 90:035149, Jul 2014.

[102] Eduardo H. da Silva Neto, Pegor Aynajian, Alex Frano, Riccardo Comin, Enrico Schierle, Eugen Weschke, András Gyenis, Jinsheng Wen, John Schneeloch, Zhijun Xu, Shimpei Ono, Genda Gu, Mathieu Le Tacon, and Ali Yazdani. Ubiquitous Interplay Between Charge Ordering and High-Temperature Superconductivity in Cuprates. *Science*, 343(6169):393–396, 2014.

[103] W. Tabis, Y. Li, M. Le Tacon, L. Braicovich, A. Kreyssig, M. Minola, G. Dellea, E. Weschke, M. J. Veit, M. Ramazanoglu, A. I. Goldman, T. Schmitt, G. Ghiringhelli, N. Barišić, M. K. Chan, C. J. Dorow, G. Yu, X. Zhao, B. Keimer, and M. Greven. Charge order and its connection with Fermi-liquid charge transport in a pristine high-Tc cuprate. *Nature Communications*, 5:5875 EP –, 12 2014.

[104] Debanjan Chowdhury and Subir Sachdev. The enigma of the pseudogap phase of the cuprate superconductors. *arXiv:1501.00002*, 01 2015.

[105] R. Blankenbecler, D. J. Scalapino, and R. L. Sugar. Monte Carlo calculations of coupled boson-fermion systems. I. *Physical Review D*, 24(8):2278–2286, 1981.

[106] D. J. Scalapino. Numerical Studies of the 2D Hubbard Model. *arXiv:cond-mat/0610710*, 2006.

[107] Congjun Wu and Shoucheng Zhang. Sufficient condition for absence of the sign problem in the fermionic quantum Monte Carlo algorithm. *Physical Review B*, 71(15), 2005.

[108] F. F. Assaad. Depleted Kondo lattices: Quantum Monte Carlo and mean-field calculations. *Phys. Rev. B*, 65:115104, Feb 2002.

[109] Zi-Xiang Li, Fa Wang, Hong Yao, and Dung-Hai Lee. What makes the Tc of monolayer FeSe on SrTiO3 so high: a sign-problem-free quantum Monte Carlo study. *Science Bulletin*, 61(12):925 – 930, 2016.

[110] Zi-Xiang Li, Fa Wang, Hong Yao, and Dung-Hai Lee. The nature of effective interaction in cuprate superconductors: a sign-problem-free quantum Monte-Carlo study. *arXiv:1512.04541*, 12 2015.

[111] S. Raghu, Gonzalo Torroba, and Huajia Wang. Metallic quantum critical points with finite BCS couplings. *Phys. Rev. B*, 92:205104, Nov 2015.

[112] Andrey V. Chubukov and Jörg Schmalian. Superconductivity due to massless boson exchange in the strong-coupling limit. *Phys. Rev. B*, 72:174520, Nov 2005.

[113] T. A. Maier, M. Jarrell, T. C. Schulthess, P. R. C. Kent, and J. B. White. Systematic Study of *d*-Wave Superconductivity in the 2D Repulsive Hubbard Model. *Phys. Rev. Lett.*, 95:237001, Nov 2005.

[114] Kristjan Haule and Gabriel Kotliar. Strongly correlated superconductivity: A plaquette dynamical mean-field theory study. *Phys. Rev. B*, 76:104509, Sep 2007.

[115] Emanuel Gull, Olivier Parcollet, and Andrew J. Millis. Superconductivity and the Pseudogap in the Two-Dimensional Hubbard Model. *Phys. Rev. Lett.*, 110:216405, May 2013.

[116] Eduardo Fradkin, Steven A. Kivelson, and John M. Tranquada. Colloquium: Theory of intertwined orders in high temperature superconductors. *Rev. Mod. Phys.*, 87:457–482, May 2015.

[117] S. Badoux, W. Tabis, F. Laliberté, G. Grissonnanche, B. Vignolle, D. Vignolles, J. Béard, D. A. Bonn, W. N. Hardy, R. Liang, N. Doiron-Leyraud, Louis Taillefer, and Cyril Proust. Change of carrier density at the pseudogap critical point of a cuprate superconductor. *Nature*, 531(7593):210–214, 03 2016.

[118] Rudolf Peierls. *More Surprises in Theoretical Physics*. Princeton Series in Physics, 1991.

[119] Eduardo H. da Silva Neto, Riccardo Comin, Feizhou He, Ronny Sutarto, Yeping Jiang, Richard L. Greene, George A. Sawatzky, and Andrea Damascelli. Charge ordering in the electron-doped superconductor $Nd_{2-x}Ce_xCuO_4$. *Science*, 347(6219):282, 01 2015.

[120] Lauren E. Hayward, David G. Hawthorn, Roger G. Melko, and Subir Sachdev. Angular Fluctuations of a Multicomponent Order Describe the Pseudogap of $YBa_2Cu_3O_{6+x}$. *Science*, 343(6177):1336, 03 2014.